

https://dspace.org/

The aerodynamic effect of wheel fairings applied to a generic formula one car

Davkin, Liam Michael

2022
https://hdl.handle.net/10539/34401

Downloaded from a DSpace repository. https://dspace.org/

THE AERODYNAMIC EFFECT OF WHEEL FAIRINGS APPLIED TO A GENERIC FORMULA ONE CAR

Liam Michael Davkin

A dissertation submitted to the Faculty of Engineering and the Built Environment, University of the Witwatersrand, Johannesburg, in fulfilment of the requirements for the degree of Master of Science in Mechanical Engineering.

Johannesburg, May 2022

Declaration

I declare that this dissertation is my own, unaided work, except where otherwise acknowledged. It is being submitted for the degree of Master of Science in Mechanical Engineering to the University of the Witwatersrand, Johannesburg. It has not been submitted before for any degree or examination at any other university.

Signed this 25th day of May 2022



Liam Michael Davkin

Acknowledgements

I would firstly like to thank my supervisor, Prof Craig Law, for his constant support and invaluable guidance throughout the duration of this research. I am forever grateful for his reassurance and encouragement during the frequent stressful times (compounded by doing research during a global pandemic).

This work was made possible by an allocation of resources (programme number MECH0847) at the Centre for High-Performance Computing (CHPC), a part of the South African National Integrated Cyberinfrastructure System (NICIS). Thank you to Dr Randall Paton for his assistance with this aspect of the project.

Thank you to Mr Michael Boer for his assistance and advice with the flow visualisation aspect of the wind tunnel testing.

Further thanks must be extended to Dr Michael Atkins, Mr Ayodimeji Biobaku, Prof Frank Kienhofer, Mr Reshendren Naidoo, and Prof Walter Schmitz, for their assistance in the sourcing, lending, and using of the experimental equipment.

Thank you to Mr Andrew Heydenrych, Mr Norman Kgasago, Mr Zwavho Netshisaulu, Mr Rowen Parumal, Mr Klaas Phaka, Mr Peter Radebe, and Mr Shaun Riekert for their assistance in manufacturing and lending of equipment, and maintaining and repairing the wind tunnel facility.

To my friends, Abraham Hartley and Richard Wilkie, thank you for lending an extra set of hands in the lab when I really needed it.

Lastly, to my parents Ivor and Judy, and my brother Kyle. Thank you for all that you did to help me throughout this time - from proofreading drafts to providing emotional support.

Abstract

A reason for the lack of overtaking in Formula One racing is often attributed to the loss of downforce for a trailing car. This is due to the car operating in a highly turbulent wake aft of a car ahead of it. A loss of downforce results in a trailing car losing control margins in corners, thus failing to overtake. Early concept images for the 2022 technical regulations suggested the use of wheel coverings or fairings over the rear wheels of the cars, in an attempt to reduce the impact downstream of a car's highly turbulent wake.

In order to ascertain the aerodynamic impact of such fairings, numerical models were employed to examine the wake structure of the car. This involved numerical wake surveys of the three-dimensional velocity components in various planes downstream of a car. A car model with no wheel fairings was tested in order to develop a baseline to which comparisons could be made. Two fairing configurations were then tested, namely a partial and full fairing. Both fairings covered part of the rear wheel tread. The partial fairing differed from the full fairing by the absence of a covering over the sidewalls of the wheels. Simulations that measured the change in drag and lift coefficient of a trailing car operating in the wake further highlighted the aerodynamic impact of the fairings. 1/6 scale wind tunnel wake surveys were conducted using a traverse system and five-hole probe to measure the three-dimensional velocity components at various planar probing locations. The data from the wind tunnel wake surveys was then compared to scale numerical models in order to provide validation to the numerical model setup. The numerical model setup was further verified by means of evaluating domain size sensitivity and mesh independence.

By analysing two-dimensional velocity contours and streamtraces, it was seen that the addition of both partial and full wheel fairings altered the wake structure. The addition of wheel fairings increase the size of low axial speed vortex cores with increased circulation to the sides of the wheels. The upwash flux towards the midplane of the car also increased due to the addition of fairings. Both these changes in wake structure would have adverse affects on downforce production for a trailing car by reducing the magnitude of the oncoming flow and decreasing the effective angle of attack of the front and rear wings. The trailing car

simulations highlighted an increase in drag coefficient and decrease in lift coefficient due to the addition of both fairing configurations.

Thus, both rear wheel fairing configurations were concluded to be ineffective in increasing the overtaking opportunities in Formula One racing. This was due to the effect of inhibiting a trailing car to follow a leading car closely because of the increase in drag and understeering in to corners due to the decrease in downforce. The traditional open-wheel configuration is thus the recommended rear wheel configuration for future car regulations.

Published Work

Aspects of this dissertation have been presented in the following references:

- 12th South African Conference on Computational and Applied Mechanics - 2021

  Article published as part of conference proceedings:

  Davkin, L. and Law, C., 2021. 'Aerodynamic Effect of Wheel Fairings on the Wake of a Formula One Car'. In MATEC Web of Conferences (Vol. 347, p. 00008). EDP Sciences.

- Aeronautical Society of South Africa (AeSSA) Annual Conference - 2021

  Presentation title: Wind Tunnel Investigation on the Wake Behind a Generic Formula One Racing Car with Rear Wheel Fairings

Contents

Declaration i

Acknowledgements ii

Abstract iii

Published Work v

Contents vi

List of Figures x

List of Tables xvi

List of Symbols xvii

List of Acronyms xix

1 Introduction 1

1.1 Background 1

1.2 Wake Behind a Car 4

1.2.1 Wake Structure 4

1.2.2 Slipstream Effects 5

1.3 Problem Identification and Purpose of Study 7

1.4 Objectives of Study 7

2 Literature Review **8**

2.1 Aerodynamic Forces on a Car 8

2.2 Aerodynamics of Wheels 10

2.3 Wind Tunnel Testing 12

2.3.1 Properties of Air in Wind Tunnel Testing 12

2.3.2 Velocity Measurement Techniques 13

2.3.3 Wind Tunnel Ground Plane Boundary Layer 15

2.3.4 Wheel Rotation in Wind Tunnel Testing 17

2.3.5 Flow Visualisation 18

2.3.6 Wind Tunnel Blockage Effects 18

2.3.6.1 Solid Blockage 19

2.3.6.2 Wake Blockage 20

2.4 Reynolds Number Independence 20

2.5 Numerical Techniques 21

2.5.1 Solvers 22

2.5.2 Turbulence Models 22

2.5.3 Boundary Layer Treatment 24

2.5.4 Mesh Independence 25

2.6 Summary of Literature Review 27

3 Method **28**

3.1 Overview 28

3.2 Wake Survey 29

3.3 Formula One Car Model . . . 30
3.4 Numerical Simulations . . . 31
3.4.1 Domain and Boundary Conditions . . . 32
3.4.2 Trailing Car Positions . . . 33
3.4.3 Geometry Preparation and Mesh Generation . . . 34
3.4.4 Numerical Model Setup . . . 37
3.5 Wind Tunnel Testing . . . 39
3.5.1 Wind Tunnel Setup . . . 40
3.5.2 Wind Tunnel Data Processing . . . 44
3.6 Summary of Method . . . 50

4 Validation and Verification **51**

4.1 Numerical Simulations . . . 51
4.1.1 Wall Treatment . . . 52
4.1.2 Mesh Independence Study . . . 53
4.1.3 Sensitivity to Domain Size . . . 56
4.2 Reynolds Number Independence . . . 57
4.3 Wind Tunnel Wake Survey . . . 59
4.3.1 Repeatability of Wind Tunnel Wake Survey . . . 61
4.3.2 Symmetry of Wind Tunnel Wake Survey . . . 62
4.4 Wind Tunnel Flow Visualisation . . . 64
4.5 Comparison of Numerical and Wind Tunnel Wake Surveys . . . 65
4.5.1 Uncertainty of Wind Tunnel Measurements . . . 71

4.6 Comparison of Scaled Numerical Models Utilising Stationary and Rotating Wheels . . . 71

4.7 Summary of Validation and Verification . . . 75

5 Results and Discussion **76**

5.1 Wake Survey of Full Size Numerical Results . . . 76

5.1.1 Wake Immediately Aft of Car ($z = 0.0L$) . . . 76

5.1.2 Wake at Aft Distance of Half a Car Length ($z = 0.5L$) . . . 83

5.1.3 Wake at Aft Distance of a Full Car Length ($z = 1.0L$) . . . 90

5.1.4 Wake at Car Symmetry Plane . . . 95

5.1.5 Wake at Wheel Midplane . . . 99

5.1.6 Streamlines at Rear Wheel . . . 102

5.1.7 Summary of Numerical Wake Survey . . . 104

5.2 Aerodynamic Performance of Trailing Car . . . 104

5.2.1 Summary of Aerodynamic Performance of Trailing Car . . . 112

6 Conclusion **113**

6.1 Recommendations . . . 116

References **118**

A Wind Tunnel Wake Survey Additional Figures **123**

B Wind Tunnel Measurement Uncertainty **125**

C MATLAB Function for Wind Tunnel Wake Survey Data Processing **127**

List of Figures

Figure 1.1: Number of overtakes during Grand Prix races versus year 1

Figure 1.2: Car with Centreline Downwash Generating (CDG) rear wing 2

Figure 1.3: Formula One car with DRS deactivated and activated 2

Figure 1.4: Concept car with front and rear wheel fairings 3

Figure 1.5: 2022 Formula One car with front wheel fairings as per regulations . . . 3

Figure 1.6: 'Mushroom-like' wake structure as found by Newbon et al. and Watts and Watkins 4

Figure 1.7: Mean u velocities in a wheel wake of an isolated wheel and a wheel in the proximity to a car as found by Knowles et al. 5

Figure 1.8: Drag and lift coefficients for leading and trailing cars found by Džijan et al. 6

Figure 2.1: Aerodynamic forces on a Formula One car 8

Figure 2.2: Increase in relative cornering speeds in motorsport versus year 9

Figure 2.3: Main downforce creating elements on a Formula One car 10

Figure 2.4: Flow visualisation showing separation over rotating and non-rotating wheels, with associated pressure coefficient distributions 10

Figure 2.5: Airflow for covered wheels 11

Figure 2.6: PIV measurement conducted by Nakagawa on the wake behind a Formula One car wheel for geometry at the start and end of a Formula One season 14

Figure 2.7: Rolling road setup in wind tunnel, illustrated by Katz 15

Figure 2.8: Boundary layer suction ahead and distributed under model, illustrated by Katz 16

Figure 2.9: Elevated ground plane and symmetry techniques, shown by Katz . . . 17

Figure 2.10:Reynolds number independence for pressure coefficients of a truck as shown by Bayındırlı 21

Figure 2.11:Dimensionless velocity u^+ distribution as a function of dimensionless wall distance y^+ for a turbulent boundary layer 24

Figure 3.1: Downstream planes investigated for wake survey 29

Figure 3.2: Formula One car used for study, with full size dimensions 30

Figure 3.3: Rear wheel with no wheel fairings, partial wheel fairings, and full wheel fairings, along with fairing geometry 31

Figure 3.4: Numerical model domain boundaries 32

Figure 3.5: Numerical model domain dimensions 33

Figure 3.6: Downstream positions of trailing car for simulations 34

Figure 3.7: Wheel contact block for meshing 35

Figure 3.8: Triangulated surface mesh of numerical model 35

Figure 3.9: Volume mesh of numerical model composed of hexahedral cells 36

Figure 3.10:Refinement zones for volume mesh 36

Figure 3.11:Modelling of prism layer for volume mesh 37

Figure 3.12:Side view of wind tunnel setup 39

Figure 3.13:Cross sectional view of wind tunnel setup 40

Figure 3.14:Calibration curve for draw-down wind tunnel as determined by Atherfold 41

Figure 3.15:Non-bevelled and bevelled ground plane leading edges 41

Figure 3.16:Elevated ground plane employed for wind tunnel tests 42

Figure 3.17:Section of boundary layer suction plate 43

Figure 3.18:Five-hole probe traverse grid for data measurement 44

Figure 3.19:Labelled five-hole probe with velocity components and angles 44

Figure 3.20:Carpet map of calibration data showing lines of constant pitch and yaws angles 46

Figure 3.21:Total pressure coefficient versus pitch angles with lines of constant yaw angle for calibration data 47

Figure 3.22:Static pressure coefficient versus pitch angles with lines of constant yaw angle for calibration data 47

Figure 4.1: Numerical simulation velocity contours for no wheel fairings at $z = 0.5L$, compared to contours by Newbon et al. 52

Figure 4.2: Wall $y+$ distribution for no wheel fairing configuration 53

Figure 4.3: Converged drag coefficient value of car versus number of mesh cells . . 55

Figure 4.4: Converged lift coefficient value of car versus number of mesh cells . . . 56

Figure 4.5: Carpet map from calibration data, compared to carpet map by Town and Camci 60

Figure 4.6: Wind tunnel velocity contours for no wheel fairings at $z = 0.5L$, compared to contours by Watts and Watkins 61

Figure 4.7: Repeatability of scale model normalised axial velocity contours for full wheel fairings at $z = 0.5L$ for wind tunnel tests 62

Figure 4.8: Symmetry of scale model normalised axial velocity contours for full wheel fairings at $z = 0.5L$ for wind tunnel tests 63

Figure 4.9: Tuft flow visualisation for no wheel fairings at $z = 0.5L$ compared to planar velocity components by Watts and Watkins 64

Figure 4.10:Scale model normalised axial velocity contours for no wheel fairings at $z = 0.5L$ for CFD and wind tunnel tests 66

Figure 4.11:Scale model normalised axial velocity contours for partial wheel fairings at $z = 0.5L$ for CFD and wind tunnel tests 67

Figure 4.12:Scale model normalised axial velocity contours for full wheel fairings at $z = 0.5L$ for CFD and wind tunnel tests 68

Figure 4.13:Numerical model and wind tunnel test normalised axial velocity distribution along height of car for no wheel fairing configuration 69

Figure 4.14:Numerical model and wind tunnel test normalised axial velocity distribution along height of car for partial wheel fairing configuration 70

Figure 4.15:Numerical model and wind tunnel test normalised axial velocity distribution along height of car for full wheel fairing configuration 70

Figure 4.16:Scale model normalised axial velocity contours for no wheel fairings at $z = 0.0L$ for non-rotating wheels 72

Figure 4.17:Scale model normalised axial velocity contours for no wheel fairings at $z = 0.0L$ rotating wheels 73

Figure 4.18:Scale model planar streamtraces for no wheel fairings at $z = 0.0L$ for non-rotating wheels 73

Figure 4.19:Scale model planar streamtraces for no wheel fairings at $z = 0.0L$ for rotating wheels 74

Figure 5.1: Full size normalised axial velocity contours for no wheel fairings at $z = 0.0L$ 78

Figure 5.2: Full size normalised axial velocity contours for partial wheel fairings at $z = 0.0L$ 79

Figure 5.3: Full size normalised axial velocity contours for full wheel fairings at $z = 0.0L$ 79

Figure 5.4: Full size planar streamtraces for no wheel fairings at $z = 0.0L$ 80

Figure 5.5: Full size planar streamtraces for partial wheel fairings at $z = 0.0L$ . . . 81

Figure 5.6: Full size planar streamtraces for full wheel fairings at $z = 0.0L$ 81

Figure 5.7: Normalised axial velocity and upwash/downwash component at centreline of car in $z = 0.0L$ plane 82

Figure 5.8: Normalised axial velocity and upwash/downwash component at centreline of wheel in $z = 0.0L$ plane 83

Figure 5.9: Full size normalised axial velocity contours for no wheel fairings at $z = 0.5L$ 85

Figure 5.10:Full size normalised axial velocity contours for partial wheel fairings at $z = 0.5L$ 85

Figure 5.11:Full size normalised axial velocity contours for full wheel fairings at $z = 0.5L$ 85

Figure 5.12:Full size planar streamtraces for no wheel fairings at $z = 0.5L$ 87

Figure 5.13:Full size planar streamtraces for partial wheel fairings at $z = 0.5L$ . . . 87

Figure 5.14:Full size planar streamtraces for full wheel fairings at $z = 0.5L$ 87

Figure 5.15:Normalised axial velocity and upwash/downwash component at centreline of car in $z = 0.5L$ plane 89

Figure 5.16:Normalised axial velocity and upwash/downwash component at centreline of wheel in $z = 0.5L$ plane 90

Figure 5.17:Full size normalised axial velocity contours for no wheel fairings at $z = 1.0L$ 91

Figure 5.18:Full size normalised axial velocity contours for partial wheel fairings at $z = 1.0L$ 91

Figure 5.19:Full size normalised axial velocity contours for full wheel fairings at $z = 1.0L$ 92

Figure 5.20:Full size planar streamtraces for no wheel fairings at $z = 1.0L$ 93

Figure 5.21:Full size planar streamtraces for partial wheel fairings at $z = 1.0L$ . . . 93

Figure 5.22:Full size planar streamtraces for full wheel fairings at $z = 1.0L$ 93

Figure 5.23:Normalised axial velocity and upwash/downwash component at centreline of car in $z = 1.0L$ plane 94

Figure 5.24:Normalised axial velocity and upwash/downwash component at centreline of wheel in $z = 1.0L$ plane 95

Figure 5.25:Normalised axial velocity contours in car symmetry plane for no wheel fairings 96

Figure 5.26:Normalised axial velocity contours in car symmetry plane for partial wheel fairings 97

Figure 5.27:Normalised axial velocity contours in car symmetry plane for full wheel fairings 97

Figure 5.28:Normalised axial velocity and upwash/downwash component in car symmetry plane 98

Figure 5.29:Normalised axial velocity contours in wheel midplane for no wheel fairings 100

Figure 5.30:Normalised axial velocity contours in wheel midplane for partial wheel fairings 100

Figure 5.31:Normalised axial velocity contours in wheel midplane for full wheel fairings 100

Figure 5.32:Normalised axial velocity and upwash/downwash component in wheel midplane 101

Figure 5.33:Streamlines at rear wheel for no wheel fairings 103

Figure 5.34:Streamlines at rear wheel for partial wheel fairings 103

Figure 5.35:Streamlines at rear wheel for full wheel fairings 103

Figure 5.36:Comparison of drag coefficients and lift coefficients for all configurations at trailing position A 106

Figure 5.37:Comparison of drag coefficients and lift coefficients for all configurations at trailing position B 107

Figure 5.38:Comparison of drag coefficients and lift coefficients for all configurations at trailing position C 109

Figure 5.39:Comparison of drag coefficients and lift coefficients for all configurations at trailing position D 110

Figure A.1: Flow visualisation for partial wheel fairings at $z = 0.5L$ 123

Figure A.2: Flow visualisation for full wheel fairings at $z = 0.5L$ 123

Figure A.3: Scale model normalised axial velocity contours for no wheel fairings at $z = 1.0L$ for CFD and wind tunnel tests 124

Figure A.4: Scale model normalised axial velocity contours for partial wheel fairings at $z = 1.0L$ for CFD and wind tunnel tests 124

Figure A.5: Scale model normalised axial velocity contours for full wheel fairings at $z = 1.0L$ for CFD and wind tunnel tests 124

List of Tables

Table 4.1: Grid convergence indices (GCI) for drag coefficient (C_D) 54

Table 4.2: Grid convergence indices (GCI) for lift coefficient (C_L) 54

Table 4.3: Drag and lift coefficients for different numerical setups 58

Table 4.4: Sample set of data of wind tunnel wake survey for no wheel fairings at $z = 0.5L$ 59

Table 4.5: Average uncertainty associated with measured wind tunnel velocity components 71

List of Symbols

α	Pitch angle (°)
β	Yaw angle (°)
$\varepsilon_{i,\ i+1}$	Relative error
ε_s	Solid blockage factor
ε_w	Wake blockage factor
λ	Model shape factor
μ_∞	Air dynamic viscosity (Pa.s)
ρ_a	Air density (kg/m^3)
τ	Wind tunnel shape factor
A	Projected frontal area (m^2)
B	Wind tunnel width (m)
C	Wind tunnel cross-sectional area (m^2)
C_D	Drag coefficient
C_L	Lift coefficient
$C_{P_{pitch}}$	Pitch pressure coefficient
$C_{P_{static}}$	Static pressure coefficient
$C_{P_{total}}$	Total pressure coefficient
$C_{P_{yaw}}$	Yaw pressure coefficient
$GCI_{i,\ i+1}$	Grid convergence index
H	Wind tunnel height (m)
h	Grid spacing (m)
h_c	Characteristic height (m)
L	Characteristic length (m)
P_{static}	Static pressure (Pa)
P_{total}	Total pressure (Pa)
$\overline{P}$	Average pressure (Pa)
q	Order of convergence parameter
q_0	Dynamic pressure (Pa)
q_c	Corrected dynamic pressure (Pa)
r	Refinement ratio
Re	Reynolds Number

R_H	Relative humidity (%)
T	Temperature (K)
T_R	Temperature (°R)
u	Velocity in x direction (m/s)
V	Velocity magnitude (m/s)
v	Velocity in y direction (m/s)
V_M	Model volume (m^3)
W_∞	Freestream velocity (m/s)
w	Velocity in z direction (m/s)
w_c	Characteristic width (m)
x	Width position (m)
y	Height position (m)
$y+$	Non-dimensional distance from wall
z	Depth position (m)

List of Acronyms

ABS	Acrylonitrile Butadiene Styrene
CAD	Computer-aided Design
CDG	Centreline Downwash Generating
CFD	Computational Fluid Dynamics
CTA	Constant Temperature Anemometry
DES	Detached Eddy Simulation
DRS	Drag Reduction System
F1	Formula One
FWF	Full Wheel Fairings
GCI	Grid Convergence Index
GP	Grand Prix
LDA	Laser Doppler Anemometry
LES	Large Eddy Simulation
NWF	No Wheel Fairings
PIV	Particle Image Velocimetry
PWF	Partial Wheel Fairings
RANS	Reynolds-averaged Navier-Stokes
URANS	Unsteady Reynolds-averaged Navier-Stokes

Chapter 1

Introduction

1.1 Background

In the last decade, Formula One (F1) racing has experienced a noticeable decline in the number of overtakes during a Grand Prix (GP) race (seen by the sharp decline circled in Figure 1.1) [1]. This has been seen by fans to have diminished the entertainment aspect of racing. Formula One is the top-tier of motorsport in the world, and having fans losing interest could have profound consequences in all levels and categories of racing.

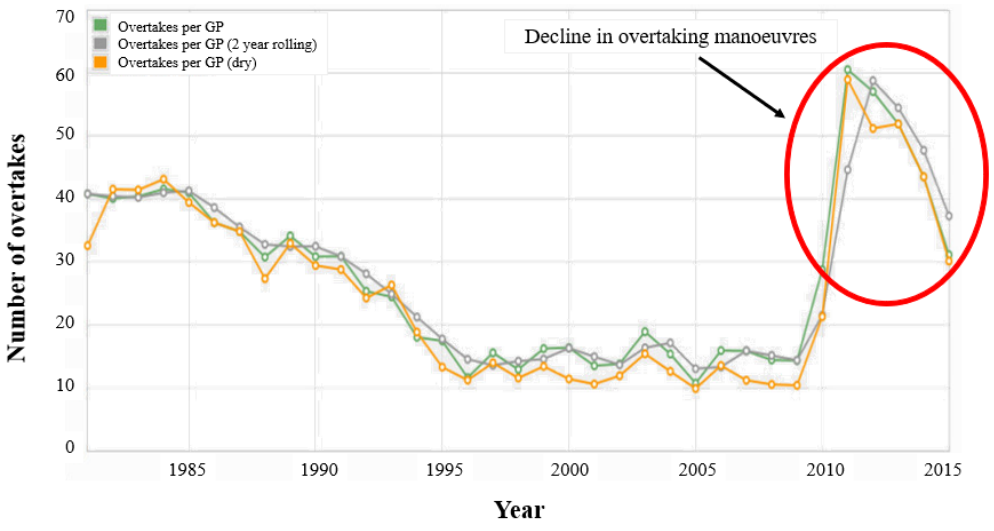


Figure 1.1: Number of overtakes during Grand Prix races versus year [1]

A traditional Formula One car has an open-wheel configuration. This wheel configuration, together with the aerodynamic shape of the cars, creates a highly turbulent wake behind the car, often referred to as 'dirty air'. Any trailing vehicle attempting to overtake is forced to

operate in this turbulent wake. This wake is attributed by drivers as a contributing factor to the lack of overtaking. This is due to a car experiencing a reduction of downforce when following a leading car here. This results in a trailing car losing downforce when in this wake and losing control margins into corners, resulting in a failed overtaking manoeuvre [2]. Modifying the wake of a leading car would eliminate this problem, allowing for closer racing.

Some solutions to the overtaking problem have been suggested over the years. One of the most radical solutions proposed was the implementation of the Centreline Downwash Generating (CDG) rear wing, seen in Figure 1.2, that enabled a trailing car to experience enhanced downforce and less drag in a leading car's wake. This concept made use of two separate smaller rear wings over the rear wheels of the car, as opposed to one single rear wing over the majority of the car's width [3]. However, this design was never implemented.

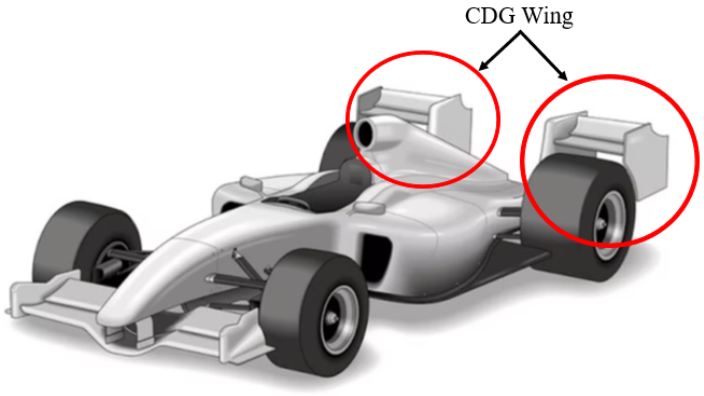


Figure 1.2: Car with Centreline Downwash Generating (CDG) rear wing [2]

One solution that has been implemented is the Drag Reduction System (DRS). This was introduced in 2011 to aid overtaking. In certain parts of a race track, a trailing car is allowed to make use of this system. As seen in Figure 1.3, it functions by lowering the angle of attack of the trailing car's rear wing, effectively reducing the frontal area of the rear wing thus reducing the drag force and increasing speed [4].

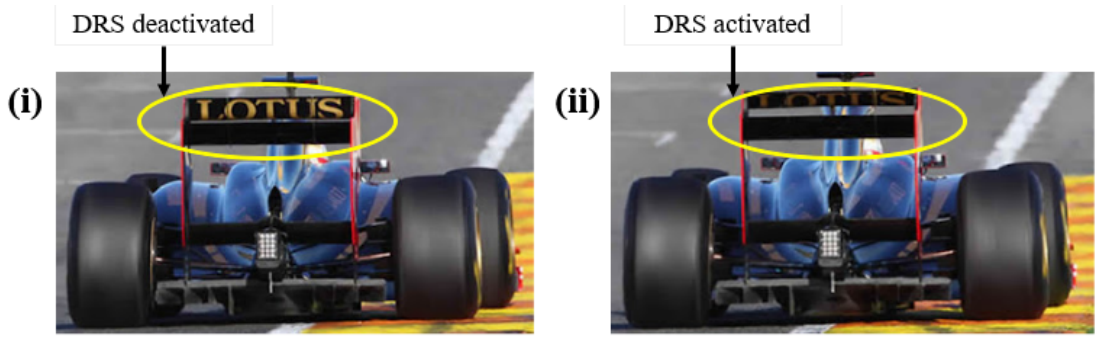


Figure 1.3: Formula One car with DRS deactivated (i) and activated (ii) [5]

Towards the end of 2018, concept images were released for the 2022 car regulations. These concepts included the addition of front and rear wheel fairings (shown in Figure 1.4). Formula One's managing director of motorsport, Ross Brawn, indicated that these fairings would function to clean up the 'dirty air' from the rotating wheels to improve the conditions of the wake behind a car [6].

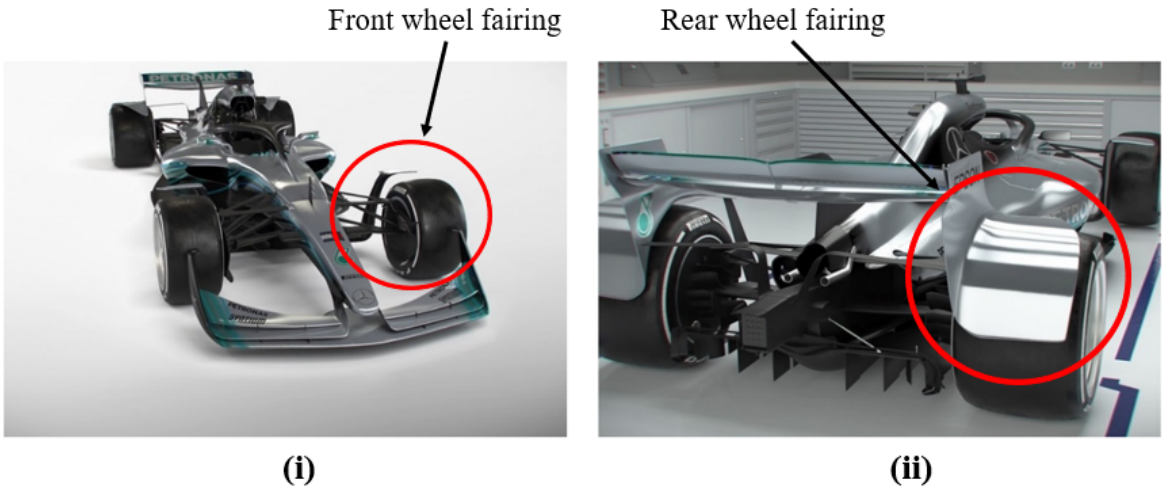


Figure 1.4: Concept car with front (i) and rear (ii) wheel fairings [7]

The finalised car configuration, shown in Figure 1.5, was announced in 2019. This configuration only included front wheel fairings. No further mention of rear wheel fairings has been announced.



Figure 1.5: 2022 Formula One car with front wheel fairings as per regulations [8]

1.2 Wake Behind a Car

1.2.1 Wake Structure

Watts and Watkins [9] characterised, with wind tunnel tests, the wake behind a 30% scale model Formula One car, without the effects of wheel rotation. This was done using a four-hole pressure probe. The wake structure was identified as being dominated by two counter-rotating vortices that originated from the rear wing of the car. A prominent centreline upwash, together with these vortices gave rise to the 'mushroom-like' wake structure, shown in Figure 1.6(ii). These vortices then combined with low-speed airflow that exited at the diffuser from underneath the car. These wake features resulted in a highly turbulent wake behind the scale model.

Newbon et al. [10] surveyed the wake behind a car through a numerical investigation. This investigation yielded the same 'mushroom-like' wake structure (seen in Figure 1.6(i)) as noted by Watts and Watkins [9], consisting of the same flow features (namely the counter-rotating vortices and centreline upwash). Thus numerical and experimental results from two separate studies yielded similar results in wake structure. This wake from a leading car would be localised at the height of a trailing car, with centreline upwash influencing the height of this wake significantly. The height of these vortices influenced the size of the wake behind a leading car. The height of the wake was dependant on the distance behind the car. This would have different implications on a trailing car at different distances downstream of a leading car. The amount of decreased downforce on the trailing car would depend on the distance between it and the leading car.

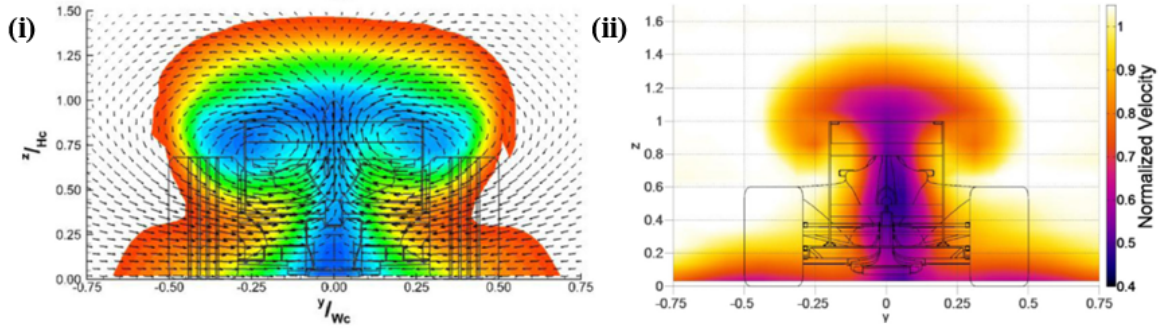


Figure 1.6: 'Mushroom-like' wake structure as found by Newbon et al. [10] (i) and Watts and Watkins [9] (ii)

Knowles et al. [11] used laser Doppler anemometry to describe the wake of a rotating wheel (in isolation, and in proximity to a scale car). This was done in order to ascertain any differences in wake structure caused by the presence of the car. The presence of the car resulted in earlier flow separation at the wheel resulting in a larger downstream wake. The airflow recirculation was upwards in the presence of the car, and backwards when in isolation. It could be concluded from this study that the wake structure displayed high sensitivity to the presence of additional aerodynamic components, as seen by the difference in mean u velocities in Figure 1.7. It was also found in this study that the presence of support struts for the wheel influenced the turbulent intensity in the near wake. This effect however was more prominent for an isolated wheel case, with the car body having a higher effect on the near wake in comparison to the strut.

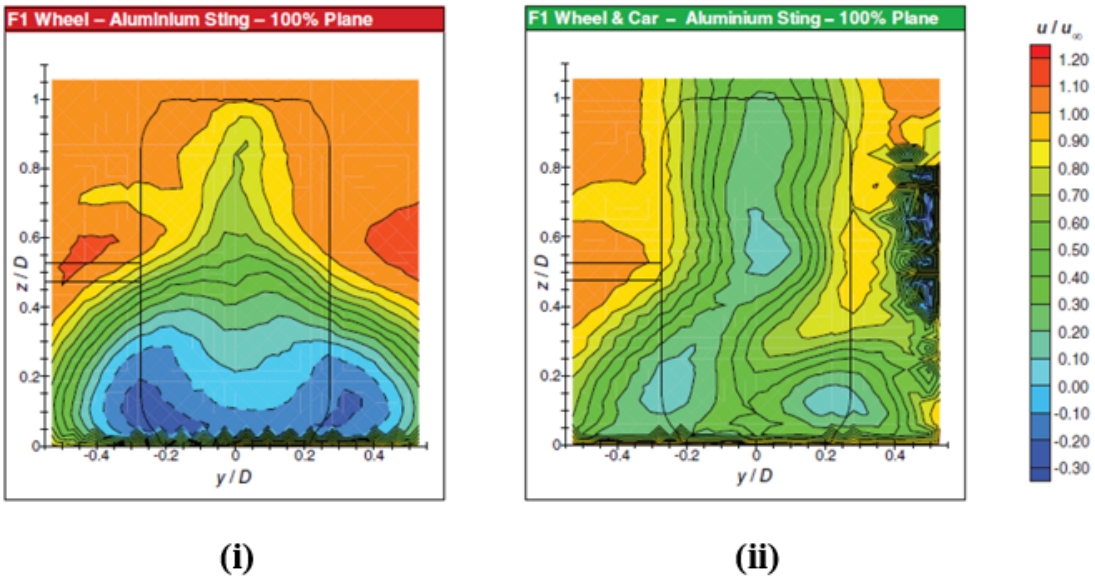


Figure 1.7: Mean u velocities in a wheel wake of an isolated wheel (i) and a wheel in the proximity to a car (ii) as found by Knowles et al. [11]

1.2.2 Slipstream Effects

It is possible for a trailing car to take advantage of the low pressure wake behind a leading car. This is done by following the leading car closely in its slipstream, in a manoeuvre known as drafting. During drafting, a trailing car experiences less aerodynamic drag than the car ahead by operating in this region of lower pressure. This manoeuvre is used during overtaking manoeuvres along straight portions of a race track. It is not suitable for overtaking in corners as it comes at the expense of a considerable loss of downforce on the trailing car [12]. In a study by Dominy [13] the effects of slipstreaming reduced downforce and drag on a trailing vehicle by as much as 36% and 23% respectively.

As part of the study by Newbon et al. [10], a bluff bodied wake generator was placed upstream of a car model to determine the effects this would have on the performance of the car. It was found that a trailing car experienced a loss of downforce of up to 38% when operating in the wake of the leading vehicle, which was attributed to the dynamic pressure deficit in the wake. This resulted in the changes in loading on the downforce generating elements, which affected the aerodynamic balance of the car, leading to more prominent understeering effects.

Džijan et al. [14] utilised computational fluid dynamics (CFD) models to examine the effects of a trailing car drafting in a slipstream of a leading car. It was found that the benefits of the slipstream were only experienced at certain distances behind the leading car. The leading car experienced a lower drag coefficient at all tested distances (shown in Figure 1.8(i)). This was due to an effective increase in fineness ratio (the ratio of object length to maximum width) due to the close presence of a trailing car. Higher fineness ratios are associated with smaller wakes and thus less momentum transfer occurs from the leading car to the downstream wake. This minimised the drag experienced by the leading car and thus also minimised the loss of speed. A decrease in downforce was also found for the leading car, albeit small (shown in Figure 1.8(ii)). The trailing car experienced an increase in drag when positioned further away from the leading car. This was due to the highly turbulent wake structures, referred to as the drag bubble. The slipstream effect was enhanced at distances less than a car length behind the leading car, but at the expense of losing up to 82% of downforce.

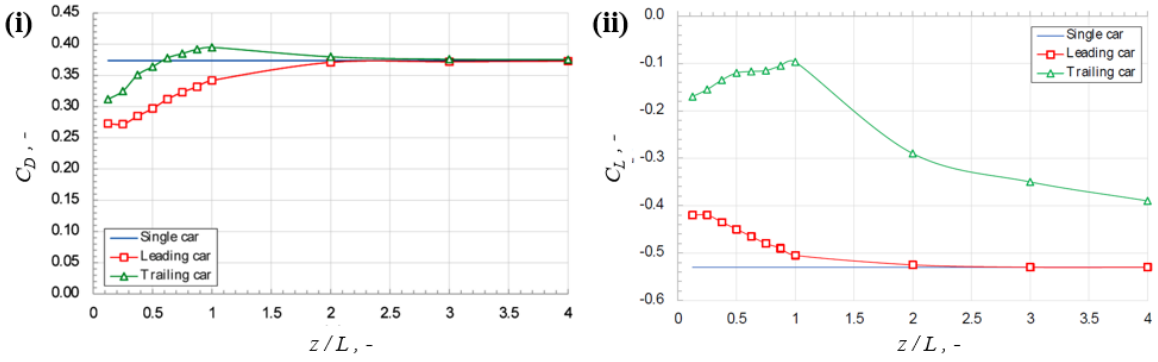


Figure 1.8: Drag (i) and lift (ii) coefficients for leading and trailing cars found by Džijan et al. [14]

These previous studies are relevant to the presented research as the results provide a means of comparison for validation purposes. The general wake structure is expected to be similar to the 'mushroom-like' shape previously found due to the very similar overall car geometry, and the presence of new parts in close proximity to the wheel would alter the wake here. This would change the drag and lift experienced by a trailing car operating in a leading car's wake/slipstream. These studies can thus provide confidence in the undertaken method and associated results.

1.3 Problem Identification and Purpose of Study

The turbulent wake that is enhanced by the effect of the current open-wheel configuration causes aerodynamic complications for a trailing car. Front wheel fairings are already going to be implemented in an attempt to remedy this problem. This study will focus on the effect rear wheel fairings might have on the wake behind a car.

1.4 Objectives of Study

The focus of this research is to examine the aerodynamic effects caused the addition of wheel fairings. The rotating wheels are a significant contributor to the high turbulence in the wake downstream of a car, which causes unfavourable conditions for trailing cars operating in this wake. This adversely effects the aerodynamic balance of the trailing cars which has negative implications on overtaking opportunities. The objectives of this research are to:

- Examine the aerodynamic wake structure aft of a single car, for both uncovered and covered rear wheel configurations.
- Investigate the influence on the aerodynamic performance of a trailing car operating in this wake, by considering changes in aerodynamic drag and downforce caused by covering the rear wheels with fairings.
- Suggest if the addition of wheel fairings could improve overtaking opportunities in Formula One racing, by changing the wake structure of a leading car, thus providing an aerodynamic benefit to a trailing car.

Chapter 2

Literature Review

2.1 Aerodynamic Forces on a Car

There are three primary aerodynamic forces that act on a car during normal operation. These are drag force, downforce (or negative lift), and side force, shown in Figure 2.1.

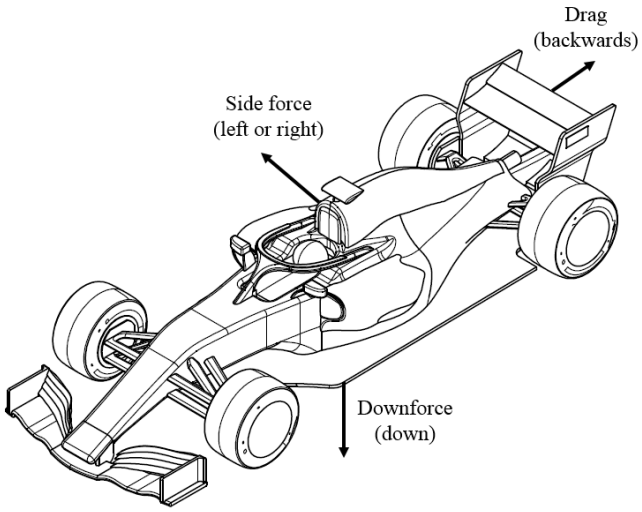


Figure 2.1: Aerodynamic forces on a Formula One car [15]

Drag is the resistive force of air that causes a reduction in vehicle speed. Side force acts to the left or right and is usually caused by crosswinds or an effective side slip angle for oncoming flow. However, side force is insignificant in most cases. Downforce pushes the car towards the ground. This increases the mechanical grip offered by the tyres. High levels of downforce are important for a vehicle to be able to corner at high speeds. Increased downforce comes at the expense of increased drag and thus the balance between these two forces must be setup carefully for different race tracks. Track layouts with a high number of sharp corners will

require a car setup favouring the production of downforce. Track layouts with long straights will require a setup that minimises drag such that as high a top speed as possible is attainable. Downforce is still required nonetheless for following the racing line and overtaking in corners for these low drag track configurations [16].

Since the late 1960's, aerodynamics have dramatically increased the cornering speed of Formula One cars. The general shape of the car is important in creating the high levels of downforce to allow for these high speeds. Inverted wings were a simple approach that began to be attached to the front and rear of the vehicle. Lotus were the first team to utilise rear wings for the Monaco Grand Prix in 1968. What followed was a series of aerodynamic innovations that exploited the aerodynamics of the car to create high levels of downforce, as noted by Jenkins [17]. This increase in relative cornering speeds (relative to value of 1.0 for that of 1993 Corvette) over the years is shown in Figure 2.2. The dashed line indicates the effects of improved tyre and aerodynamic technology over cars with no such developmental changes (shown by the solid line).

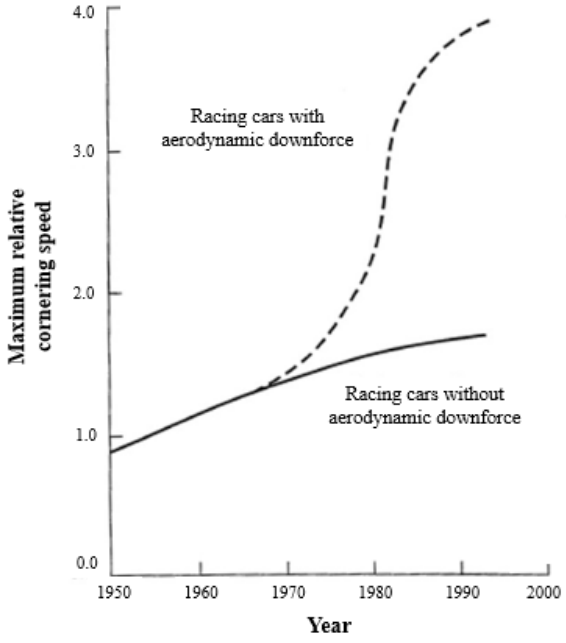


Figure 2.2: Increase in relative cornering speeds in motorsport versus year [16]

The main downforce producing elements of a Formula One car are the front wing, the rear wing, and the diffuser and underbody, as shown in Figure 2.3. The underbody creates downforce by exploiting the ground effect of high speed air flowing under the car. Lower speed airflow along the car surface results in a pressure differential between the underside surface of the car, which causes a resultant aerodynamic force downwards. The balance between the front and rear wheels is an important factor during car setup. More downforce produced by the front wing will result in oversteer and more downforce produced by the rear wing will result in understeer [10]. The aerodynamic efficiency depends on the conditions

of the air the car has to operate in. A car moving through highly disturbed air will lose aerodynamic efficiency for these elements.

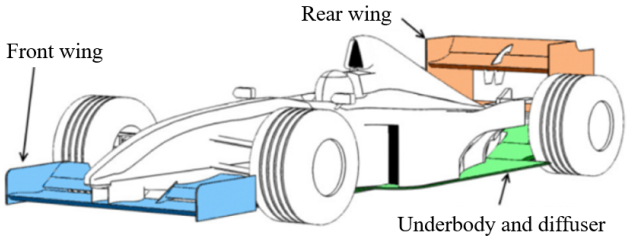


Figure 2.3: Main downforce creating elements on a Formula One car [10]

2.2 Aerodynamics of Wheels

As noted by Katz [16], air flow does not remain attached when moving over wheels. A point of separation thus exists along the the circumference of a wheel. This leads to periodicity in the wake behind the car, contributing significantly to the turbulence intensity here. The point at which airflow separates from the surface of the wheel differs based on the motion of the wheel. The separation point for a rotating wheel exists further upstream due to the increased velocity gradient due to the tangential velocity imposed by the rotation at the tread of the tyres. With a lower velocity gradient when stationary, the separation point exists further downstream for non-rotating wheels. This results in significantly different pressure distributions between the two cases as seen in Figure 2.4.

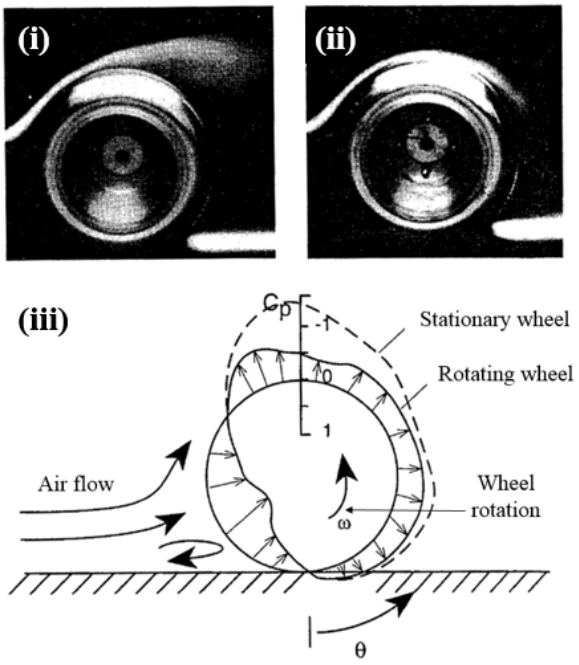


Figure 2.4: Flow visualisation showing separation over rotating (i) and non-rotating wheels (ii), with associated pressure coefficient distributions (iii) [16]

The rotation of the wheels can have a significant influence on the drag and downforce of the vehicle. The earlier separation results in a higher static pressure aft of the wheels in comparison to stationary wheels. A higher static pressure exists ahead of the wheel due to air slowing down and recirculating. The pressure difference fore and aft of the wheel will therefore have an effect on the drag and downforce experienced by the car. The rotation of the wheels also affects the way in which air recirculates ahead of it. Rotation induces motion of air that will interact with this recirculating flow. Should the wheels be covered, this interaction would be enhanced. The motion of the wheel drives the airflow in the space between the wheel and any covering (as seen in Figure 2.5), and this can have an effect on the wake of the wheels depending on how the air is channelled [16]. These changes in wake structure by covering the wheels can be explored numerically to ascertain the effects on a trailing car.

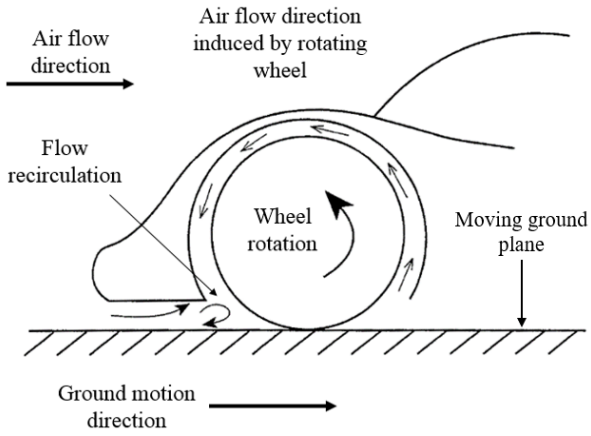


Figure 2.5: Airflow for covered wheels [16]

Tests conducted by Audi (cited by Wickern et al. [18]) showed that covering the wheels of a passenger car influenced the associated drag coefficient. The baseline drag coefficient for the car was measured as being 0.316. Covering the rear wheel reduced this value to 0.310 and covering the front wheel reduced the value to 0.303. A combination of rear and front covers resulted in a drag coefficient of 0.294. A similar relationship was also seen by Cavusoglu [19] utilising a CFD study on electric vehicle aerodynamics in which covering the wheels had a reduction on total body drag. If the covering of wheels was implemented in Formula One racing, both a leading and trailing car would have to make use of such coverings, and both would thus experience effects in aerodynamic forces. This could be even more pronounced for a trailing car operating in a leading car's wake.

Wäschle [20] investigated the effect of wheel rotation on the aerodynamics of passenger vehicles. Steady state numerical simulations were conducted, utilising a half car model assumed to be symmetrical about the centreline. The rotation of the wheels caused a reduction in drag and lift at the front wheel. The wake aft of non-rotating wheels was found to be larger

in comparison to the wake caused by rotating wheels. This was the case for tests conducted by Bearman et al. [21] in which wind tunnel wake surveys for both rotating (with a moving ground plane) and non-rotating wheels were conducted. It was found that the wake for the different configurations varied significantly, with the non-rotating wake being dominated by the wheel and the boundary layer of the floor, with the vortices in the wake of the rotating wheels being much weaker. This is because the rotation of the wheels allowed for the additional transfer of energy, thereby resulting in reduced flow losses in the wake aft of the wheel. This reduced the size of the turbulent wake behind the car, which could create more favourable overtaking conditions. For the current study, it can be expected that a model with non-rotating wheels will thus not be truly representative of real-world conditions, but can be useful for verification and validation purposes.

Wäschle [20] noted the size of the wake of passenger cars was found to influence the efficiency of the diffuser. The diffuser functions by allowing for a gradual expansion of high speed airflow from underneath the car. A large wake interfered with this expansion, causing a reduction of downforce experienced by the a leading car. Due to these wake differences, it was thus preferable to utilise models with rotating wheels as these simulate, more closely, real-world operating conditions. At higher speeds associated with Formula One cars, these effects may be more pronounced than for passenger cars. This confirms the need to utilise rotating-wheels for numerical models.

The aerodynamics of wheels have a significant impact of the overall flow structure around a car. The way in which the wheel geometry is designed and modelled can affect the performance of a vehicle in terms of drag and lift production, as well as having flow structure effects far downstream. It can be expected that any design alterations to the wheel geometry of a Formula One car will have aerodynamic effects on the car itself, while also effecting the flow around it and by association, other cars close by.

2.3 Wind Tunnel Testing

Wind tunnel testing simulates the real-world aerodynamics of a car by a change of reference frame. It is impractical to test a car during normal operation and therefore wind tunnel tests utilise a stationary model with airflow past it.

2.3.1 Properties of Air in Wind Tunnel Testing

Air is often idealised when calculating its properties. However, this comes with a certain level of approximation. Jones (see Barlow et al. [22]) developed equations of state for the

properties of air. Air density is given by:

$$\rho_a = \left(\frac{0.0034847}{T}\right)(P - 0.003796 R_H e_s) \tag{2.1}$$

The saturation vapour pressure of air can be related by:

$$e_s = \left(1.7526 \times 10^{11}\right) e^{(-5315.56/T)} \tag{2.2}$$

An approximation for the air viscosity is given by Barlow et al. [22] and was found using Sutherland's law [23]:

$$\frac{\mu_\infty}{\mu_0} = \left(\frac{T_R}{T_0}\right)^{3/2} \frac{T_0 + 198.6}{T_R + 198.6} \tag{2.3}$$

2.3.2 Velocity Measurement Techniques

In a wind tunnel wake survey, it is important to measure the three dimensional velocity components, u, v and w. Two commonly used methods to measure these quantities are constant temperature anemometry (CTA) or hot-wire anemometry and multi-hole pressure probes. Constant temperature anemometers make use of a heated metal wire at a constant temperature. When exposed to airflow, the temperature will change due to forced convection, thereby inducing a voltage change across the wire, which can be correlated to find the velocity components. CTA also provides time resolved data which allows for unsteady behaviour and turbulence intensity to be measured directly [24]. Hot-wire anemometry was employed by Kim et al. [25] to successfully survey the wake of a passenger car mirror by measuring velocity components along with vorticity.

Optical methods for velocity measurement also exist, namely laser Doppler anemometry (LDA) and particle image velocimetry (PIV). Both these methods contaminate the flow with small particles or markers. In LDA, a beam of light is shone into the flow field, where it is scattered by the moving particles. The frequency of the scattered light is detected by a photodetector and converted to an electrical signal that can be processed to extract the velocity components. PIV utilises a pulsed beam of light that illuminates the markers over short predefined exposure times. A camera then captures the movement of these particles at these different exposure times and the distance travelled by the markers can be used to determine the velocity components of the particles [24]. Knowles et al. [11] successfully surveyed the structure of the wake behind a wheel using LDA (§1.2.1). Nakagawa et al. [26] examine the flow structure around a Formula One car. The study was successful in analysing the wake behind the front wheel of the car, with comparisons made with different geometries based on development throughout a Formula One season. Quantities such as

mean velocities were able to be extracted from the PIV data (shown in Figure 2.6). The PIV measurements were also successful in resolving flow features such as vortices. Both LDA and PIV allow for flow fields to be measured without causing obstructions in the flow through blockage effects (such as in the case of CTA and multi-hole probes and the associated traverse mechanisms). However, these systems are difficult to implement due to substantially high experimental costs. In addition, while seeding the test section with these particles does not significantly change the flow density or other transport properties of the fluid, the model can be contaminated during prolonged tests.

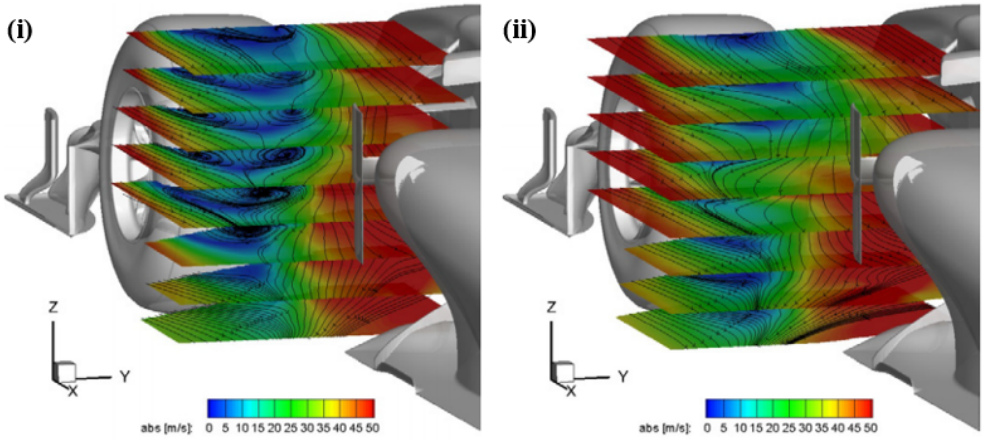


Figure 2.6: PIV measurement conducted by Nakagawa [26] on the wake behind a Formula One car wheel for geometry at the start (i) and end (ii) of a Formula One season

Multi-hole probes allow for the measurement of pressures at a point that are then converted to non-dimensional pressure coefficients. These coefficients can then be correlated to calibration data to form various combinations of pitch and yaw angles to extract the velocity components of a flow. An advantage to the use of multi-hole probes over hot wire-anemometry is the insensitivity to external temperature changes and lower costs [27].

Ruchała et al. [27] calibrated a multi-hole pressure probe using a non-nulling technique, achieving low uncertainty values for pitch and yaw angles. This technique involves keeping the probe parallel to the freestream flow and then interpolating the results based on the calibration data. This is opposed to the nulling technique that rotates the probe during tests to known pitch and yaw angles until the pressures measured by the probe are balanced [28]. The nulling technique results in easier data processing but has the disadvantage of requiring sophisticated rotation equipment.

Thus, the use of a non-nulling technique for using a five-hole probe presents a simplified and accurate method of conducting a wake survey. However, it is only suitable for providing time averaged data due to the inertia of the fluid in the probe, as well as due to the response rate

of the attached manometer/s. This makes a five-hole probe suitable for mapping a pseudo steady wake, allowing for suitable information needed to map the steady wake of a Formula One car.

2.3.3 Wind Tunnel Ground Plane Boundary Layer

Under normal real-world conditions of a car driving, the car moves through stationary air. Wind tunnel testing employs a change in reference frame so that the car remains stationary with air flowing past it. This replicates the real-world conditions very well but some discrepancies do exist. One of the most prominent is the boundary layer formation over the ground plane. This boundary layer does not form during real-world conditions because there is no relative motion between the air and ground. Because the boundary layer consists of low-speed rotational air flow, this region can influence the results from wind tunnel tests, especially for car models with low ride heights. Barlow et al. [22] suggested various removal solutions in reducing the effect of this boundary layer. A widely used method is a rolling road (shown in Figure 2.7). This setup employs a moving belt underneath the car. It moves at the same speed as the freestream airflow. Thus there is no relative motion between the air and the floor and no boundary layer will form. This method is costly to implement and can have the unwanted effect of the belt lifting up towards the underside of the car. This is caused by suction effects due to the low pressure underneath the car. It is also difficult to match the belt speed exactly to the airflow speed and thus some form of boundary layer will always be present. Axon [29] suggested that the ratio between the freestream velocity and the local region velocity within 2 mm of the ground plane should be equal to at least 99%.

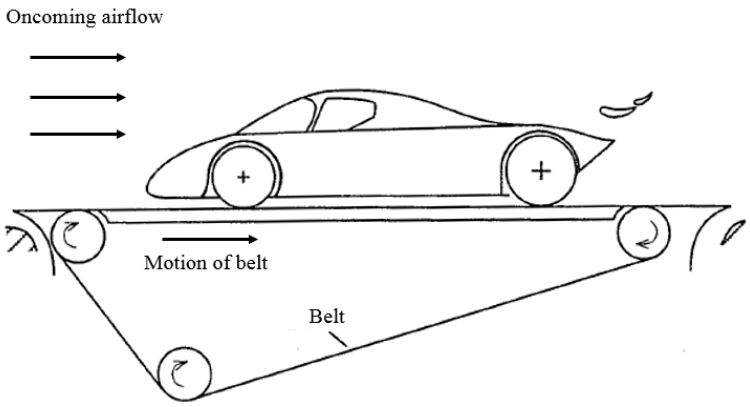


Figure 2.7: Rolling road setup in wind tunnel, illustrated by Katz [16]

It is possible to speed up this air so that the boundary layer reduces in thickness. This is achieved through suction. One form of suction involves placing a slot ahead of the car model. This reduces the thickness of the boundary layer at the start of the model position (shown

in Figure 2.8(i)), allowing a new thinner boundary layer that will have less interference to form aft of the slot. Katz [16] recommended that the thickness of this new boundary layer should not exceed 10% of the model's ground clearance. It is also possible to use distributed suction under the entirety of the model length using a perforated plate (shown in Figure 2.8(ii)). Each hole of this plate would remove the boundary layer formed over the distance between it and the hole immediately ahead of it. A combination of a suction slot ahead and a distributed suction plate was used by Lutz and Sayers [30] during wind tunnel tests on model trucks. This device made use of larger diameter holes for the slot ahead of the model, with the distributed suction plate having smaller holes over the length of the model. The suction was provided by means of fans connected to a box with a perforated top. This device successfully removed 60% of the boundary layer thickness ahead of the model, as well as removing 80% of the boundary layer displacement thickness. The drag values for the truck model increased between 3.8% and 10% due to the implementation of the suction device.

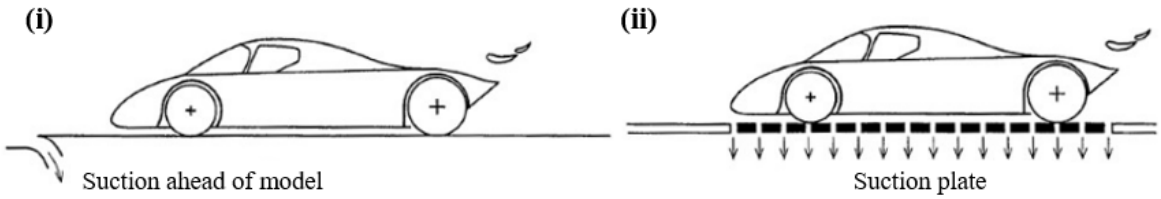


Figure 2.8: Boundary layer suction ahead (i) and distributed under (ii) model, illustrated by Katz [16]

A simple method proposed by Katz [16] that reduces the boundary layer thickness is using an elevated ground plane (shown in Figure 2.9(i)). Boundary layer thickness at a point depends on the length at which that point is from the leading edge of the ground plane. Thus if the length from the leading edge is shorter, a thinner boundary layer will form. An elevated plane is shorter in length than the the length of an entire wind tunnel floor. Thus a thinner boundary layer would form along it in comparison, thus reducing the interference effects of the boundary layer. Stevenson [31] utilised an elevated ground plane along with a suction ahead and under the model in the wind tunnel tests of a Le Mans prototype. This suction was not able to remove the boundary layer and displacement thickness sufficiently but did contribute towards experimental results matching numerical ones. Furthermore, a final method suggested by Katz [16] is the use of model symmetry. This involves using a second exact model that is symmetrical about the ground plane underneath the original model (shown in Figure 2.9(ii)). This eliminates the need for a physical ground plane altogether, with a streamline forming the ground plane. Doig [32] utilised a symmetry plane in a study on compressible ground effect aerodynamics. This method creates the complication in creating two exact models. It also creates the need to use a larger wind tunnel cross section as doubling the frontal area of the model increases blockage effects.

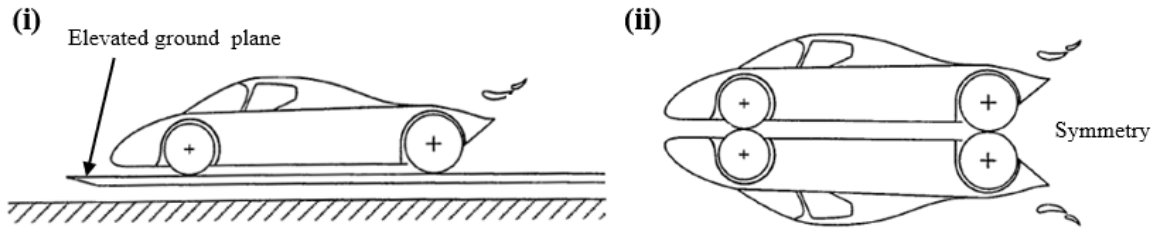


Figure 2.9: Elevated ground plane (i) and symmetry (ii) techniques, shown by Katz [16]

Cooper et al. [33] noted that boundary layer removal methods with a stationary ground plane are not suitable for wind tunnel test involving race cars due to these cars having sophisticated underbody diffuser designs. These methods are only suitable for passenger vehicles. Thus only rolling road configurations should be used. However in the absence of a rolling road, (or any other form of ground boundary layer removals) Pagliarella [34] demonstrated strong correlation in a replication of wind tunnel results of a bluff body first investigated by Ahmed et al. [35].

Thus, in term of simplicity, an elevated ground plane is suitable for boundary layer reduction. When surveying a wake, an elevated ground plane (in combination with some suction) would reduce the boundary layer effects sufficiently to obtain accurate results that can be used as validation for more sophisticated numerical models.

2.3.4 Wheel Rotation in Wind Tunnel Testing

As noted by Wäschle [20] (§2.2), tests with non-rotating wheels do not replicate real-world conditions and models with wheel rotation should be favoured. Barlow et al. [22] has suggested ways of successfully achieving tyre rotation. These methods include a rolling road, rotation mechanisms attached directly to the wheels and rollers embedded in the ground plane that make contact with the wheels to cause rotation. This method of floor rollers was utilised by Cogotti [36] during tests in the Pininfarina wind tunnel, before an upgrade to a rolling road was made. The method of rotation mechanism in the model itself requires a hole clearance in the floor to allow space for the wheel to rotate. This clearance hole creates a gap through which air flow can move through and thus has to be carefully implemented and sealed off. The use of a moving ground plane is desirable because this method also has the added effect of avoiding boundary layer development on the ground plane (§2.3.3). Hennig et al. [37] performed numerical simulations replicating the effects of rolling roads and stationary floors with rotating wheels using both a Formula 3 car and Le Mans prototype. Rotating wall boundary conditions were applied to the wheels, with a tangential velocity component applied to the ground plane for the rolling road simulations. Different belt configurations for

the moving ground were also considered - namely single belt, 3-belt, 5-belt and T-belt configurations. For both cars, it was concluded that a rolling road setup was necessary (utilising either a single belt or 3-belt configuration) to accomplish wheel rotation as using only rotating wheels resulted in incorrect values of drag and lift being measured due to the interaction of the underbody flow with the boundary layer. This was the same result found by Cooper et al [33].

Axon et al. [38] showed that CFD models can accurately predict the qualitative flow structures around both stationary and rotating wheels, thus providing useful validation data for experimental studies. Therefore, in the absence of such facilities for the proposed study, stationary wheel wind tunnel wake surveys can still provide validation to a numerical setup through comparison to a numerical model without wheel rotation. If successful validation is achieved in this case, the same numerical setup can be confidently applied to a numerical model with rotating wheels.

2.3.5 Flow Visualisation

Flow visualisation techniques enable qualitative data to be gathered on the aerodynamics around a car. Flow visualisation involves contaminating the airflow with particles that flow along the streamlines of the fluid flow, enabling flow behaviour to be better understood. McBeath [39] mentions various flow visualisation techniques in addition to LDA and PIV (§2.3.2) . The simplest technique uses tufts that are attached to a surface that follow the direction of the flow. Bird [40] utilised a tuft grid in order to visualise wake behaviour behind delta wings. This method however does not allow a full streamline to be visualised as the tufts have to remain attached to the surface. To enable full streamlines to be seen, it is also possible to use contaminants such as smoke trails and helium bubbles that have no hindrance in movement and can move freely through a test section. Stevenson [31] utilised the method of coating the Le Mans prototype surfaces with liquid that leaves examinable streaklines as it flows over the surface of the model. However, tuft grids can be effectively utilised to visualise the flow structure in a two-dimensional plane, and can be used to effectively validate flow phenomena from two-dimensional planar velocity contours.

2.3.6 Wind Tunnel Blockage Effects

Under normal operating conditions, the free-stream cross-sectional area a vehicle operates in is effectively infinite. Wind tunnel testing introduces physical boundaries in the form of walls, creating a finite cross-sectional test area that differs slightly from these regular free-stream conditions. It is therefore necessary to implement certain corrections that account for

these differences, enabling wind tunnel test results to be as reflective of real-world operating conditions as possible. Two of these corrections serve to account for solid and wake blockage effects as per Barlow et al.[22]. These blockage effects result in an increase in dynamic pressure, and thus local air velocity, in the test section. Mercker [41] developed a correction to be applied to the dynamic pressure, being composed of both solid and wake blockage factors, ε_s and ε_w respectively:

$$q_c = q_0(1 + 2\varepsilon_s + 2\varepsilon_w) \tag{2.4}$$

2.3.6.1 Solid Blockage

The presence of a scale-model (along with other components such as ground planes and measurement apparatus) within the finite wind tunnel test section is an important consideration. The scale model (and other components) have a certain cross-sectional area. This effectively reduces the cross-sectional area of the wind tunnel, causing the air flow to speed up. The ratio of these cross-sectional areas is referred to as the blockage ratio, and is suggested by Barlow et al. [22] to be no higher than 5% in order to be considered insignificant. The solid blockage factor, ε_s, is given by Lock [42] as:

$$\varepsilon_s = \tau\lambda\left(\frac{A}{C}\right)^{3/2} \tag{2.5}$$

A and C correlate to the model projected frontal area and wind tunnel cross sectional area respectively. The approximate value of τ developed by Thompson (see Cooper [43]), the tunnel shape factor, is given by:

$$\tau = 0.41\left(\frac{B}{H} + \frac{H}{B}\right) \tag{2.6}$$

B and H correspond to the width and height of the wind tunnel respectively. An approximation for the model shape factor (λ), incorporating the model volume (V_M), is given by Young and Squire [44]:

$$\lambda = \frac{\sqrt{\pi}}{2}\left(\frac{V_M}{A^{3/2}}\right) \tag{2.7}$$

The solid blockage factor allows for the model to be appropriately sized in relation to the wind tunnel cross section such that the qualitative flow field is a true representation of the aerodynamics of the model, without alteration due to size.

2.3.6.2 Wake Blockage

Wake blockage is blockage caused by the size of the wake of the model. The wake has a mean velocity that is lower than the free-stream velocity. In order for the continuity criterion to be maintained, the airflow surrounding the wake must be of a higher velocity than that of the free-stream further away from the wake [22]. The wake blockage factor is given by Mercker [41], based on the summation of wake blockage factors presented by Thom (as seen in Mercker [41]) and Maskell [45], as:

$$\varepsilon_w = \frac{A}{C}\left(\frac{1}{4}C_D + \eta\right) \tag{2.8}$$

Where constant $\eta = 0.43$. Other types of interference effects in addition to solid and wake blockage exist, such as buoyancy and streamline curvature. However, Mercker [41] has found that these are of less significance for automotive aerodynamic testing. The wake blockage factor, together with the solid blockage factor provide a correction to apply to the acquired data such that any loss of accuracy, due to blockage effects, is removed.

2.4 Reynolds Number Independence

Most wind tunnels are not sufficiently large to accommodate a full-size car model. To avoid the size constraints, scale models can be used that closely replicate the behaviour of full-size vehicles. As noted by Barlow [22], being able to correlate results between models of two different sizes is known as dynamic similarity. A convenient measure for dynamic similarity is the Reynolds number defined as:

$$Re = \frac{\rho_a V L}{\mu_\infty} \tag{2.9}$$

It is often not possible to match Reynolds numbers for high speed race cars. This is because a reduction in size of the car needs to be accompanied by an increase in velocity. These required speeds are often in excess of the capabilities of a wind tunnel facility and may introduce compressibility effects. However, above a certain Reynolds number non-dimensional

quantities such as drag and lift coefficient remain unchanged as Reynolds number changes. This is known as Reynolds number independence and was shown in a study conducted by Bayındırlı et al. [46] that aimed to determine the drag coefficient of a truck. In this study, it was found that at Reynolds numbers corresponding to a turbulent flow regime, beyond a certain threshold the pressure coefficients remained constant (shown in Figure 2.10). This can be applied to turbulent flows with high Reynolds numbers.

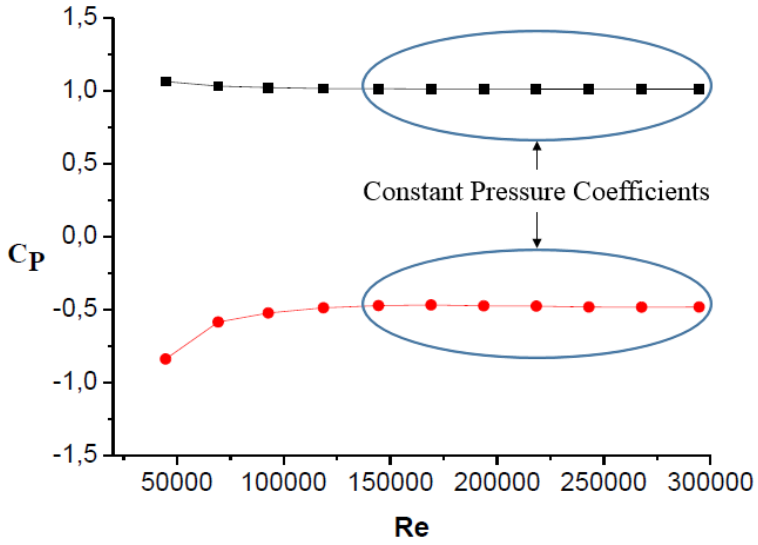


Figure 2.10: Reynolds number independence for pressure coefficients of a truck as shown by Bayındırlı [46]

2.5 Numerical Techniques

The use of computational fluid dynamics (CFD) is advantageous because it allows for the aerodynamics simulation of full scale vehicles at real-world speeds. It also allows for geometry changes of the model to be quickly employed and tested in comparison to real-world experiments. This process involves importing CAD files of the model geometry into a domain with set boundaries with conditions. The air around the model is then discretised into small elements, altogether composing a three-dimensional mesh. An initial solution is applied to the mesh. The fluid dynamics governing equations (conservation of mass, momentum and energy), along with a turbulence model, are then applied to each element iteratively until a converged solution to the flow problem is achieved. The absolute error of the measured variables from these equations are referred to as residuals. Decreasing residual values are used as a measure of convergence for a numerical solution. However, these are considered an inadequate evaluation of convergence. This is particularly true for oscillating solutions, where residuals may never drop to low values, thereby creating a false impression that the

solution is not converged. It is therefore important to also monitor engineering quantities (such as forces coefficients), together with the residuals, in order to judge convergence [47].

2.5.1 Solvers

As per the STAR-CCM+ User Guide [47], two main distinct time model solvers are available for use for external aerodynamics simulations. These are namely steady and unsteady solvers. The main difference between these solvers is the use of a physical time step to resolve the flow features of the domain. The steady state solver does not implement a time step, and thus the resultant flow structure does not vary with time. Thus time averaged results are obtained from the use of a steady state solver. For an unsteady solver, flow characteristics change with time. The solution progresses in predefined increments (or time steps), with the solution being calculated for each time increment. Steady state simulations are less computationally expensive with faster turnaround times, whereas unsteady simulations are better suited for resolving variating or periodic flow features.

Krastev and Bella [48] conducted a study in which unsteady and steady state Reynolds-Averaged Navier Stokes (URANS and RANS respectively) turbulence models were applied to an Ahmed body in order to evaluate the differences in results between the two different solvers. The results were then compared to experimental ones. It was found that both URANS and RANS models accurately predicted mean flow aerodynamic parameters such as drag coefficients which successfully matched and validated the experimental results. Thus it was recommended that the use of RANS simulations for predicting mean flow parameters and structures should be favoured over URANS simulations, as a compromise between accuracy of results and computational times.

Thus for the presented study, RANS turbulence models were considered appropriate in being able to obtain accurate time averaged results that would provide a good understanding of the macroscopic flow structure of a Formula One car's wake. This modelling approach would also allow for the successful interrogation of any change in the macroscopic flow structures caused by covering the wheels, along with changes in mean aerodynamic parameters such as drag and lift coefficients.

2.5.2 Turbulence Models

It is necessary to apply turbulence modelling to the fluid dynamics governing equations. This is done by a statistical approach as developed by Reynolds [49]. A point in a turbulent flow is the sum of a mean and a fluctuating component, U_i and u_i' respectively. Time averaging

equation for conservation of momentum results gives the Reynolds-averaged Navier-Stokes (RANS) equation:

$$\rho\frac{\partial U_i}{\partial t} + \rho U_j\frac{\partial U_i}{\partial x_j} = -\frac{\partial P}{\partial x_i} + \frac{\partial}{\partial x_j}\left(2\mu S_{ji} - \rho\overline{u_i' u_j'}\right) \tag{2.10}$$

The last term in equation 2.10 is the Reynolds stress tensor. The specific Reynolds stress tensor is denoted as:

$$\tau_{ij} = -\overline{u_i' u_j'} \tag{2.11}$$

This creates a closure problem as there exists 10 unknowns with only four equations that can be solved. For closure to exist, more equations are required. This is provided by means of suitable turbulence models. As per Wilcox [50], the starting point for the most commonly used turbulence models is the Boussinesq eddy-viscosity approximation. This equation is used to calculate the Reynolds stress tensor as the product of an eddy viscosity (ν_T) and the mean strain rate tensor (S_{ij}), i.e:

$$\tau_{ij} = 2\nu_T S_{ij} - \frac{2}{3}k\delta_{ij} \tag{2.12}$$

This introduces two terms, k and δ_{ij}. These are the turbulent kinetic energy per unit mass and the Kronecker delta respectively. The Kronecker delta equals 1 when $i = j$, and equals 0 when $i \neq j$. The eddy viscosity acts in a way analogous to viscous stresses in the flow, as stated by Versteeg and Malalasekera [51]. There exist one-equation and two-equation turbulence models based on this approximation that provide a turbulence length scale and are therefore complete. Two-equation models are more commonly used and employ two transport equations that are used to solve for the turbulent kinetic energy (k) and either the specific dissipation rate (ϵ) or the turbulent dissipation rate (ω). The k – ω and k – ϵ are the most widely used turbulence models for aerodynamic modelling. The k – ω model is superior in predicting flow near a wall, whereas the k – ϵ model has the advantage of better predicting free shear flows. Igali et al. [52] employed k – ω, k – ϵ, and SST turbulence models in predicting the flow around an Ahmed body with a slant angle of 25°. The SST (or Menter's Shear Stress Transport) model is a hybrid model that combines the advantages of the k – ω and k – ϵ into a single turbulence model. It was found that the SST model was the most successful in correlating to experimental results, as well as results obtained utilising Large Eddy Simulations.

2.5.3 Boundary Layer Treatment

The turbulent boundary layer consists of three distinct regions (shown in Figure 2.11), namely the viscous sub-layer, the buffer layer, and the log-law layer. These layers differ in the relationship between the dimensionless distance from the wall (y^+) and the dimensionless velocity (u^+). In the viscous sub-layer, the shear stress is constant and equal to the shear stress at the wall, with u^+ being equal to y^+. This region is valid for values of y^+ up to a value of 5. Above a y^+ of 30, the log-law layer is valid where both viscous and turbulent effects are prominent, with a logarithmic relationship between u^+ and y^+. In between these two regions, exists the buffer layer, where the viscous and turbulent stresses are similar in magnitude [51].

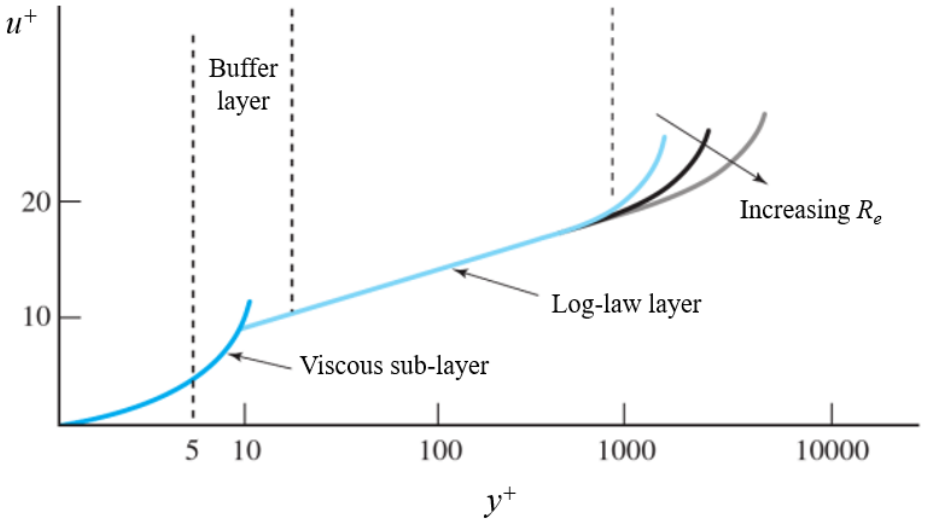


Figure 2.11: Dimensionless velocity u^+ distribution as a function of dimensionless wall distance y^+ for a turbulent boundary layer [24]

In a numerical model, it is thus important to choose an appropriate region for boundary layer treatment. This depends on a chosen value of y^+. Thus the size of the cell layer immediately adjacent to the wall needs to capture the correct chosen value of y^+. Schlichting and Gersten [53] suggested the following equation in determining the height of the first layer of cells:

$$y^+ = 0.172 \left(\frac{y}{L}\right) R_e^{0.9} \tag{2.13}$$

This equation should not be used for y^+ values of between 5 and 30 (i.e. the buffer layer) as it is undesirable to choose this boundary layer treatment for numerical models.

It is possible to either model both low y^+ and high y^+ values. When modelling low y^+ values, a fine mesh at the boundary wall is required for the viscous layer to be resolved. This requires y^+ of all locations of the boundary wall to be approximately 1, which is extremely computationally expensive. Modelling high y^+ uses a wall-function approach with a coarser mesh in comparison to low y^+ modelling. The wall-function employs the use of algebraic relations to develop boundary conditions based on temperature, turbulence quantities, and velocity. This results in the log layer region being modelled. For high Reynolds number flows, the viscous sublayer is often small and insignificant. Therefore high y^+ treatment is recommended for high Reynolds number flows, such as the high speed external aerodynamics of a Formula One car in this study [47].

2.5.4 Mesh Independence

It is important to ascertain that the results of a numerical study are due to the setup of the numerical model, and not due to the resolution of the mesh itself. This is done by means of a mesh independence/grid refinement study. According to Versteeg and Malalasekera [51], the traditional approach for a mesh independence study is the process of refinement (decreasing cell size and thus increasing the number of cells) of the mesh of the fluid domain. This refinement is repeated while certain parameters (such as force coefficients) of the flow field are monitored. Smaller cells are capable of capturing smaller scale flow phenomena which may affect the values of these parameters. When further refinement does not cause a change in the values of the monitored parameters, the domain is considered mesh independent. Another method for such a study was outlined by Roache (cited separately in Roache [54]). The procedure for such a study is outlined here. Such a study makes use of three separate meshes with three different grid spacings (or cell sizes). The three meshes are a fine grid, a medium grid, and a coarse grid, with grid spacing values corresponding to h_1, h_2 and h_3 respectively. These grid spacing values should have a common refinement ratio (r), that is:

$$r = \frac{h_3}{h_2} = \frac{h_2}{h_1} \tag{2.14}$$

This refinement has the condition of $r \geqslant 1.1$. A parameter known as the order of convergence (q) is then required. To compute this parameter requires known values of some monitored quantity (f_1, f_2, and f_3 for the fine, medium, and coarse meshes respectively), such as drag or lift coefficient. This order of convergence parameter is defined by Roache [54] as:

$$q = \ln\left(\frac{f_3 - f_2}{f_2 - f_1}\right) / \ln(r) \tag{2.15}$$

Roache [54] suggested the use of a grid convergence index (GCI) as an indication of the effect refinement has on the value of a monitored quantity. The GCI indicates how far the computed monitored quantity is from the asymptomatic true value of that quantity in the form of a percentage. Thus, the GCI value also provides an indication of the relative error of the computed quantity from the true value. The GCI is given by:

$$GCI_{i,\,i+1} = \frac{F_s|\varepsilon_{i,\,i+1}|}{r^q - 1}\,, \qquad i = 1, 2 \tag{2.16}$$

F_s is a factor of safety value that is approximately equal to 1.25 when performing the independence study using three separate meshes. The parameter $\varepsilon_{i,\,i+1}$ is the relative error between the computed value of a certain mesh, and that of the mesh with the coarser level of refinement. This is given by Roache [54] as:

$$\varepsilon_{i,\,i+1} = \frac{f_{i+1} - f_i}{f_i}\,, \qquad i = 1, 2 \tag{2.17}$$

The GCI value is used in conjunction with the Richardson's extrapolation. This extrapolation provides the continuum value of the monitored quantity. This correlates to the value at zero grid spacing i.e. the value as the cell size approaches an infinitesimally small one. This is defined by Roache [54] as:

$$f_{h=0} \approxeq f_1 + \frac{f_1 - f_2}{r^q - 1} \tag{2.18}$$

By comparing the two calculated values for the grid convergence index (i.e. GCI_{12} and GCI_{23}), it can be determined if the monitored quantities are within the asymptomatic range of convergence. The ratio of these two values is given by Roache [54] as:

$$GCI_{23} = r^q GCI_{12} \tag{2.19}$$

If the ratio of GCI_{12} and GCI_{23} is approximately equal to 1, the solution can be considered to be within the acceptable range of convergence, and the solution can be concluded to be independent of the mesh level of refinement.

2.6 Summary of Literature Review

This section has summarised previous research, as well as discussed numerous research techniques that can be employed for the proposed research problem. Extensive research has previously been conducted on the aerodynamics of Formula One cars. This has included extensive studies on the wake of a Formula One car. However, this research has only ever focused on an open-wheel configuration for the car. No research exists as to what the effect of covering the wheels may have on the aerodynamics of the wake behind a car, or the effects on any other cars in the vicinity.

Chapter 3

Method

3.1 Overview

The method outlined here was followed in order to meet the stated objectives of this study (§1.4). In order to evaluate the wake of a Formula One car, and the changes made by covering the rear wheels, numerical simulations were employed to simulate the associated high speed aerodynamics. A baseline model with no wheel coverings was tested, after which the wheels were covered and the differences in wake structure between the baseline were evaluated. An investigation of the wake structure was done through extracting the three-dimensional velocity components of the airflow (u, v, and w in the x, y, and z directions respectively). These components allowed for various two-dimensional planes of the wake structure to be developed, which made for useful comparison between configurations. Numerical models were also performed to ascertain the changes caused by wheel fairings on the aerodynamic performance of a trailing car.

Scale wind tunnel wake surveys were conducted in order to provide validation to the numerical model. The same two-dimensional planes of the wake structure created using velocity components were created for various distances downstream of a car. These could then be used to compare to scale numerical models to confirm that the numerical setup was correct. The numerical model was also verified through tests such as mesh independence.

After this data had been interrogated, it was then possible to make conclusions as to the effects of rear wheel fairings on the wake structure and if such changes in configuration would be beneficial in creating more overtaking opportunities in Formula One Racing. A specific fairing geometry could also be recommended, if found to be beneficial.

3.2 Wake Survey

A wake survey was conducted in order to understand the effects that the addition of wheel fairings had on the flow structure aft of the car. Various planes were examined for this purpose. Results for three planes perpendicular to the flow direction were studied, at various characteristic lengths behind the car. These three planes corresponded to immediately aft of the car ($z = 0.0L$), half a car length behind the car ($z = 0.5L$), and a full car length behind the car ($z = 1.0L$). Examining planes in increments downstream of the car enabled the growth of the wake to be accurately visualised. However, a wind tunnel wake survey was not possible at the plane $z = 0.0L$. This was due to the presence of a protrusion parallel to the freestream flow on the probe itself. This protrusion is used to correctly orientate the probe, but would collide with the car model during operation, thus preventing accurate traversing movements. Only half planes are interrogated, with the wake having been assumed to be symmetrical about the car centreline (this assumption was validated during the wind tunnel wake survey). Two aft planes parallel to the flow direction were also considered, namely along the symmetry/midplane of the car, and the midplane of the rear wheel. These planes are shown in Figure 3.1.

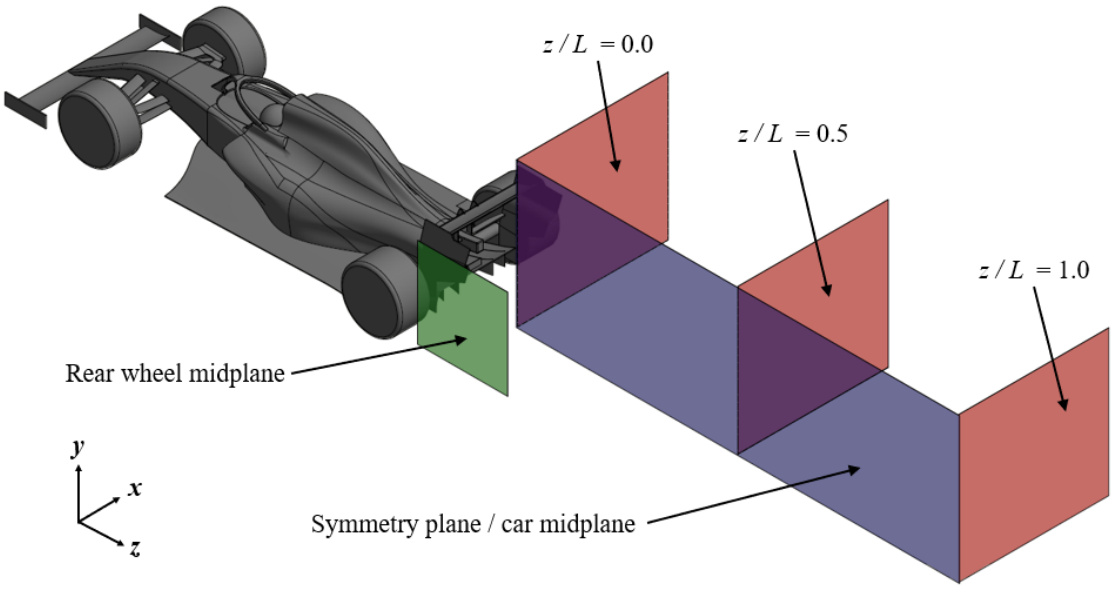


Figure 3.1: Downstream planes investigated for wake survey

3.3 Formula One Car Model

A generic Formula One car was used for this investigation (shown in Figure 3.2, with dimensions). The model did not have any specific aerodynamic components unique to a particular team. This model was based on openly published CAD geometry [15]. The model had all downforce generating components, namely the underbody, diffuser, front wing, and rear wing. Simplifications were made to the model in order to allow for easier scale wind tunnel model manufacturing. These simplifications included using simple airfoil shapes for the front and rear wings. This would result in downforce and drag values that were not of similar magnitude to those of a competition car, but still resulted in wake structures that were qualitatively similar. Changes in drag and downforce values could still be compared between different configurations, regardless of the actual magnitudes of these values. The complicated rear wheel suspension was replaced with a simple axle. The detail of the wheel hub was neglected and the sidewall of the wheel was simply a smooth surface. The helmet of the driver was modelled as a simple sphere and the cockpit of the car was enclosed. The sidepods of the car were sealed off and no internal flow through the radiators was considered. Thus no interaction between internal and external air flows occurred.

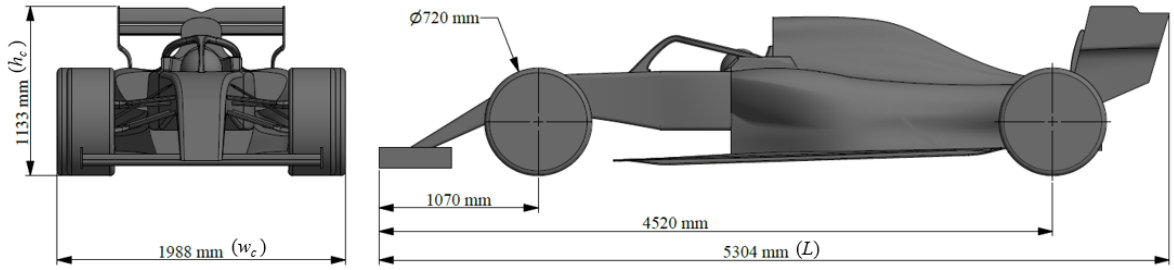


Figure 3.2: Formula One car used for study, with full size dimensions

Three different rear wheel configurations were considered for this investigation - no wheel fairings, partial wheel fairings, and full wheel fairings (shown in Figure 3.3(i), (ii), and (iii) respectively). The fairings began at the front of the wheel, at a clockwise angle of 30° from the horizontal. This angle was chosen somewhat arbitrarily such that the fairing did not circumferentially cover the entire wheel tread, and thus stray too far from the traditional open-wheel configuration. The fairings then extended backwards circumferentially to the back of the wheel, by 180° [55]. By extending past the horizontal midplane of the wheel at the trailing edge, added safety would be realised by preventing a car from launching

upwards, should contact be made with the wheel of another car. This geometry is illustrated in 3.3(iv). The difference between the partial and full fairings was the placement of a cover over the sidewall of the wheel for the full fairing configuration. Both fairing configurations fully covered the tread width of the wheel. The chosen fairing geometries/configurations served as an initial design concept to investigate the aerodynamic effect of covering the rear wheels and thus additional geometries were not considered for this study.

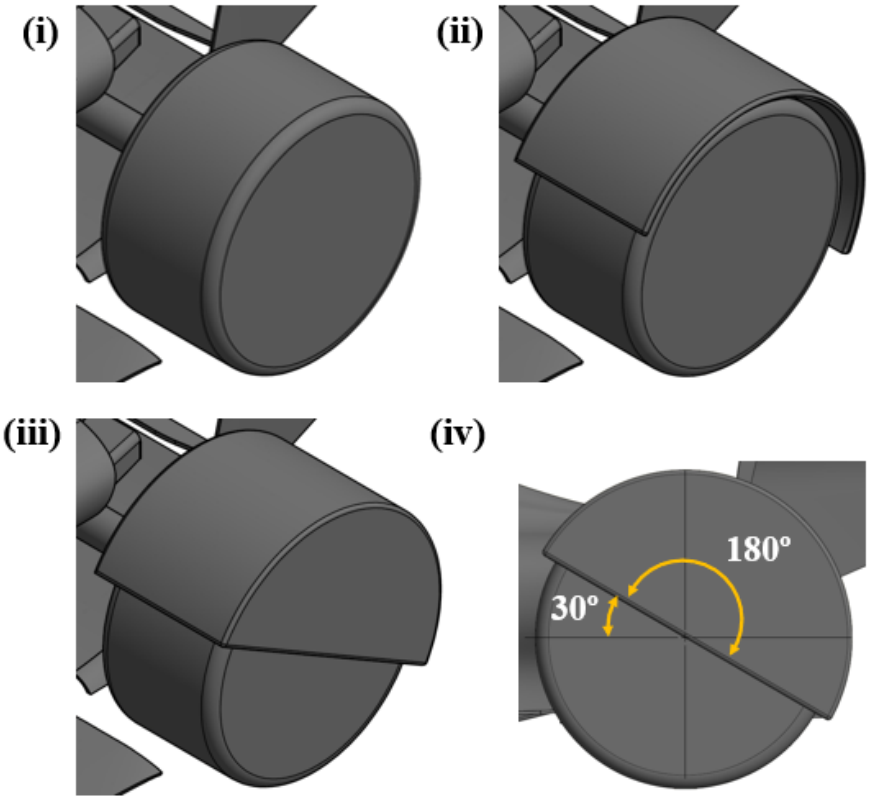


Figure 3.3: Rear wheel with (i) no wheel fairings, (ii) partial wheel fairings, and (iii) full wheel fairings, along with (iv) fairing geometry

3.4 Numerical Simulations

Numerical simulations allowed for the full scale car geometry to be tested at a speed applicable to real-world conditions. In addition, 1/6 scaled numerical models were conducted for comparison with experimental wind tunnel results, for validation of the numerical model setup. Verification was conducted by means of successive refinement to determine grid independence, along with verifying the wall $y+$ values and assessing the sensitivity of the model to domain sizes. The velocity components of the wake were surveyed for all three rear wheel configurations, having examined a full-size and scale model for each. Simulations were also conducted that evaluated the change in drag and lift coefficients of a trailing car positioned

in the wake of a leading car. Variations in these coefficients due to the changes in wake structure by the addition of partial and full fairings could be determined. All numerical models were run using Simcenter STAR-CCM+ 2020.3.1 (15.06.008). All meshing and setup procedures were completed using recommendations outlined in the Simcenter STAR-CCM+ User Guide [47]. Various two-dimensional velocity planes (shown in Figure 3.1 above, §3.2) were developed using Tecplot 360 (version 2018.2.0.92317). These planes displayed the w velocity component, along with the vectors of u and v in the xy plane.

3.4.1 Domain and Boundary Conditions

The domain of the numerical model had various conditions imposed at each boundary (shown in Figure 3.4). The surface of the car model, along with the ground plane, were modelled as smooth walls. This allows for the boundary layer growth along these surfaces. A boundary layer does not normally appear in real-world operating conditions as there is no relative velocity between the air and ground. A boundary layer along the ground plane is thus a CFD specific phenomena. A velocity inlet plane was imposed upstream of the car model, and a pressure outlet plane existed downstream of the model. The numerical model was assumed to be symmetrical about the mid-plane (symmetry plane) of the car. This assumption was made in order to reduce the size (and number of cells) of the model by half, thereby drastically reducing computational time. This plane was thus modelled as a symmetry plane. The top and side surfaces of the domain were sufficiently far away from the car model to be modelled as inviscid boundaries. These planes were part of the flow far-field and thus had no impact on the development of the wake structure aft of the car.

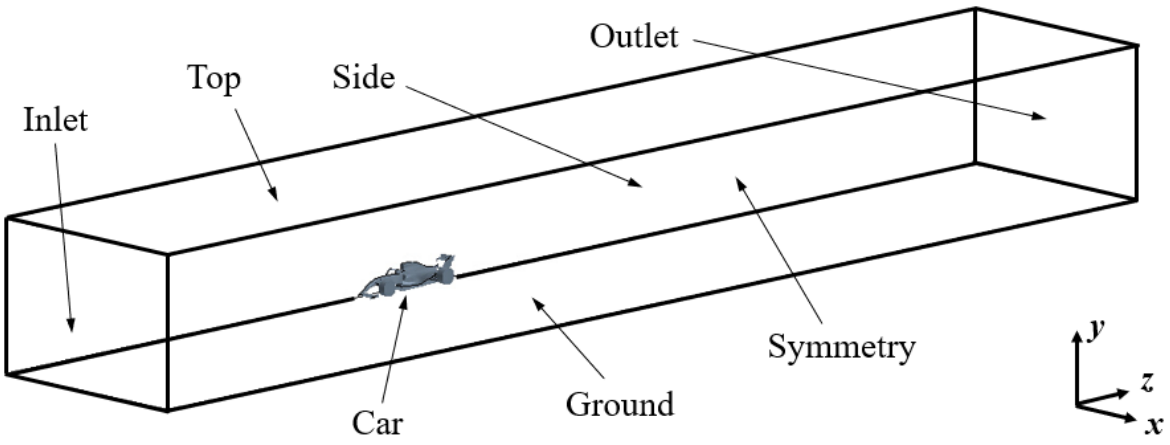


Figure 3.4: Numerical model domain boundaries

The sizing of the domain was an important consideration in order to avoid blockage effects due to close proximity to the imposed boundary conditions. The sizing of the domain was chosen based on a recommendation by Siemens [56], which had been previously found to result in a blockage ratio of less than 1%. The dimensions of the domain (shown in Figure 3.5) were chosen as increments of characteristic measurements of the car (i.e. car length (L), width (w_c) and height (h_c)). The domain extended upstream of the model by a distance of $4L$. the domain extended downstream of the model by a distance of $6L$. The width of the domain extended by a distance of $5w_c$ from the symmetry plane. The height of the domain had a distance equal to $6h_c$.

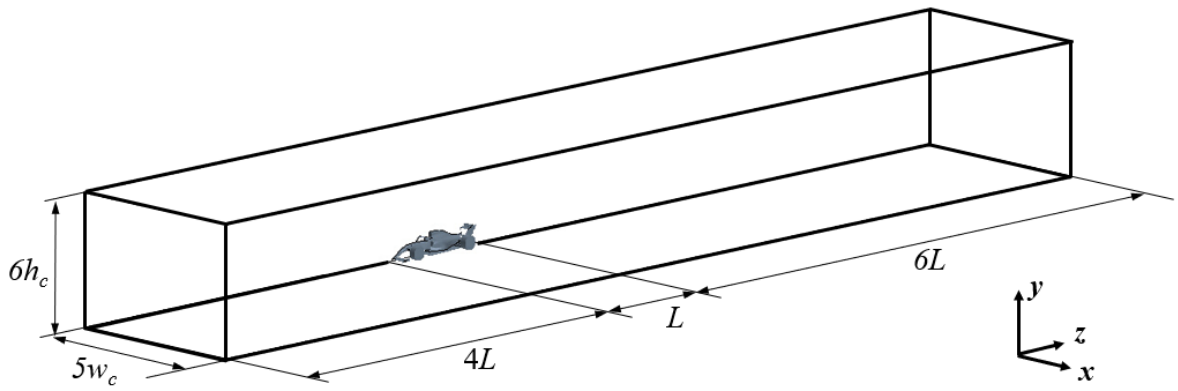


Figure 3.5: Numerical model domain dimensions

3.4.2 Trailing Car Positions

Four different positions were considered for the trailing car simulations, namely positions A, B, C, and D. The centre of the front wing of the trailing car was positioned at these locations, as shown in Figure 3.6. Positions A and B correlated to the slipstream of a leading car, while positions C and D were to the side of a leading car. Positions A and C was half a car length downstream of the leading car, and positions B and D were a full car length downstream of the lead car. The same mesh settings were applied for both cars. The domain size was altered such that the minimum boundary distances away from the car (§3.4.1) were implemented for both cars. Half car models were used for positions A and B with the midplane of the car being a plane of symmetry. For positions C and D, the midplane of the leading car was too close to the full geometry of the trailing car. A symmetry plane would have resulted in blockage effects due to the modelling of the presence of another trailing car about this plane. Thus full car models were used here with no plane of symmetry midplane implemented. The domain extended by the recommended width in both the positive and negative x directions.

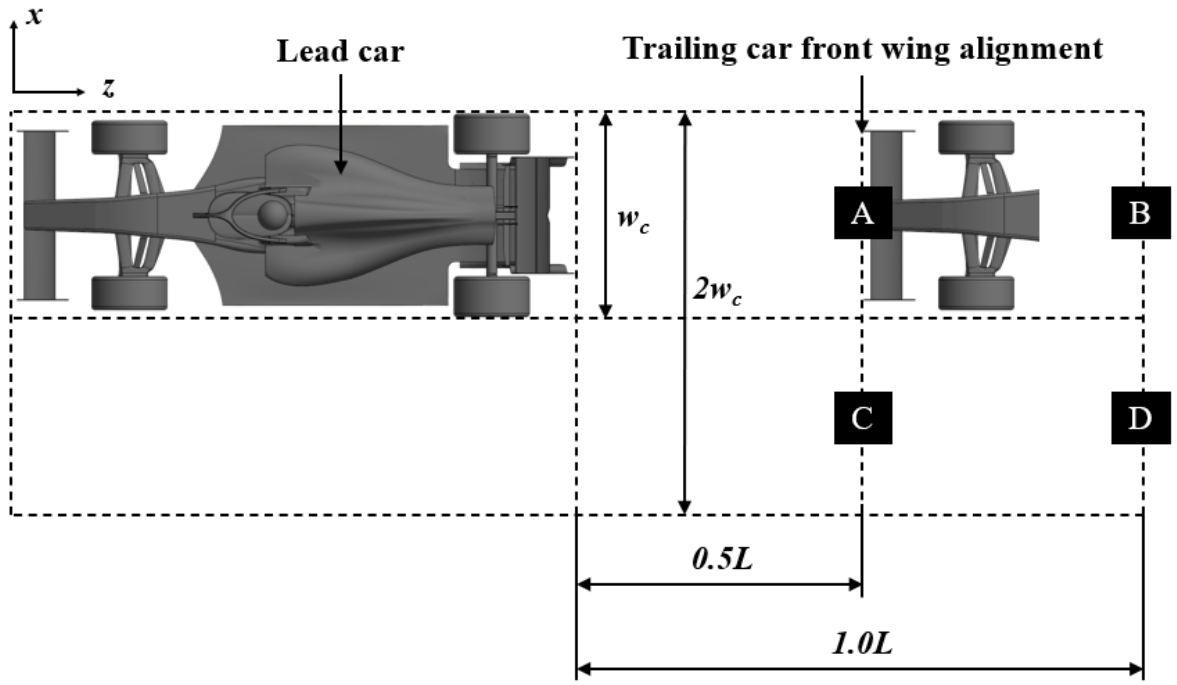


Figure 3.6: Downstream positions of trailing car for simulations

3.4.3 Geometry Preparation and Mesh Generation

Before meshing, certain repairs were required to be made to the CAD geometry. These were mostly the covering of gaps in the CAD model that were created during the modification process in which simplifications to the geometry were made. This surface repair was completed using the built-in surface wrapper tool. This tool created a closed manifold, consisting of surface cells, around the CAD geometry, thus closing any gaps/holes in the model. The size of these cells were set to a base value of 12 mm. Further size refinement controls were implemented to create a finer cell density at parts of the geometry with high curvature, such as the wheels and wings. This resulted in a high quality geometry surface suitable for meshing.

Special modelling treatment was required at the location representing the contact point between the wheels and the ground plane. This prevented the formation of poor quality cells close to this contact point. A wheel contact block/socket was superimposed on the geometry at this contact point and was wrapped in the manifold created during surface wrapping. This prevented a sharp angle between the wheel tread and ground from forming close to the contact point. This contact block extruded from the ground plane, through the wheel. Consequently, the wheel did not rest on top of this contact block and still made contact with the ground plane. Thus, the ride height of the car was not altered by the addition of this

contact block/socket. A comparison of the wheel geometry before and after the addition of the contact block is shown in Figures 3.7(i) and (ii) respectively.

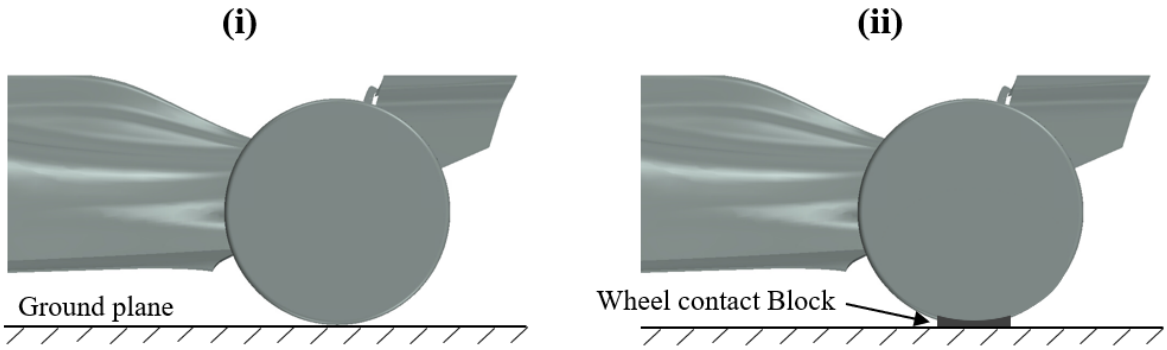


Figure 3.7: Wheel contact block for meshing

The generation of a surface mesh, utilising an automated parts-based meshing tool, then discretised the surface of the closed manifold, along the domain boundaries into a collective triangulated representation of the model and domain surfaces (shown in Figure 3.8). A suitable cell base size (h) was selected depending on the refinement level required for a particular mesh. Refinement controls were implemented on different surfaces of the car model, in order to accurately capture the curvature of the car. These refinement controls were setup to be a function of the base cell size. Therefore, when the base cell size was altered, all refinement controls were automatically adjusted to yield the appropriate mesh density. Cells in the freestream/far-field were increased in size to reduce cell count, as no interesting flow phenomena existed in these regions, and a high grid density was not required here to capture any of these features.

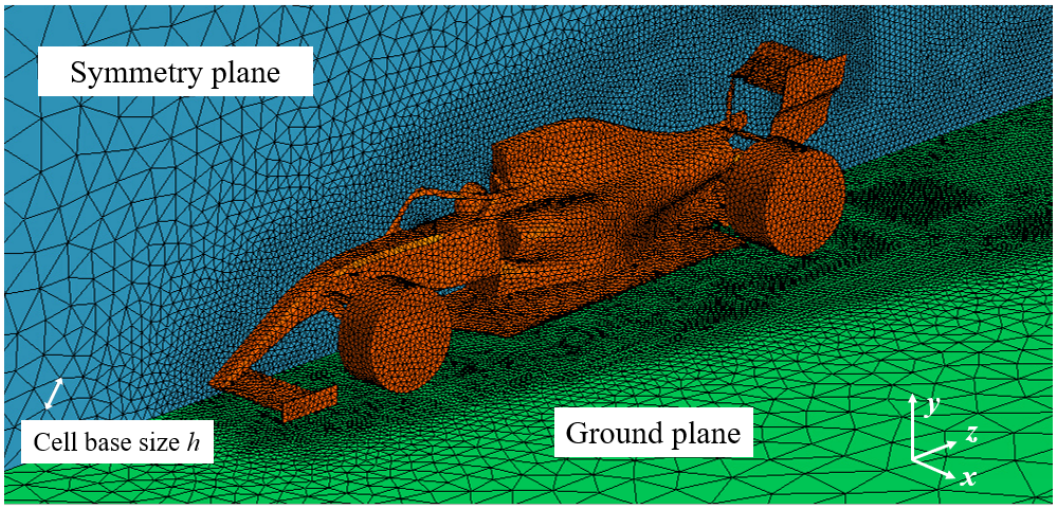


Figure 3.8: Triangulated surface mesh of numerical model

The resultant discretisation by the surface mesh provided a surface around which the air in the domain was discretised to form a three dimensional volume mesh consisting of hexahedral cells (shown in Figure 3.9).

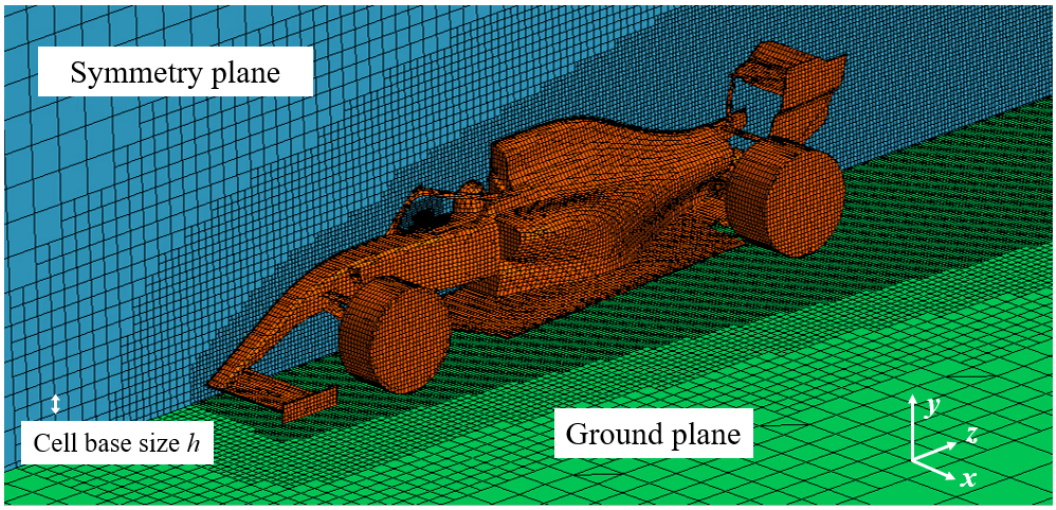


Figure 3.9: Volume mesh of numerical model composed of hexahedral cells

It was necessary to include refinement zones in the wake region aft of the vehicle in order to accurately capture the flow structure. Two refinement zones were applied to the mesh (shown in Figure 3.10). These refinement zones extended slightly upstream of the model, and downstream of the model far enough such that at least one characteristic length behind the model was refined. The first refinement zone was set to have a cell size that was 5% of the volume mesh base cell size. The second refinement zone was set to have a cell size that was 10% of the volume mesh base cell size.

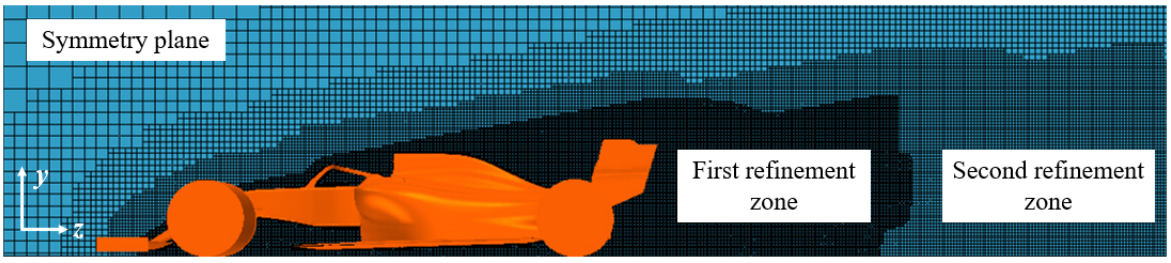


Figure 3.10: Refinement zones for volume mesh

A prism layer for boundary layer effects was generated around the surfaces of the car (shown in Figure 3.11), based on a surface $y+$ value of 50 (i.e. corresponding to the log-law region of the turbulent boundary layer). As per the STAR-CCM+ User Guide [47], a high $y+$ treatment is recommended when cell count is required to be minimised for faster turnaround times. It is also recommended as an appropriate wall treatment for turbulence models that do not damp turbulence in the near-wall region (such as SST $k-\omega$). The recommended range

for $y+$ values when using high $y+$ treatment is between 30 and 50. However, cells that yield $y+$ values below this range due to separation are considered acceptable with this treatment. A high $y+$ wall treatment was thus chosen as modelling lower $y+$ values requires a greater number of prism cell layers. The resolution of the boundary layer was considered to be of secondary importance to the examination of the wake structure, and therefore the high $y+$ wall modelling was chosen to reduce the number of mesh cells. The height of the first prism layer cell immediately adjacent was determined by the the formula given by Schlichting and Gersten [53] (§2.5.3) as 0.825 mm for the full scale car. A total of 5 layers of prism cells were included, giving a total thickness of approximately 16.5 mm for the full scale car. These values were appropriately scaled for the 1/6th scale models. No prism layer cells were included at the domain boundaries.

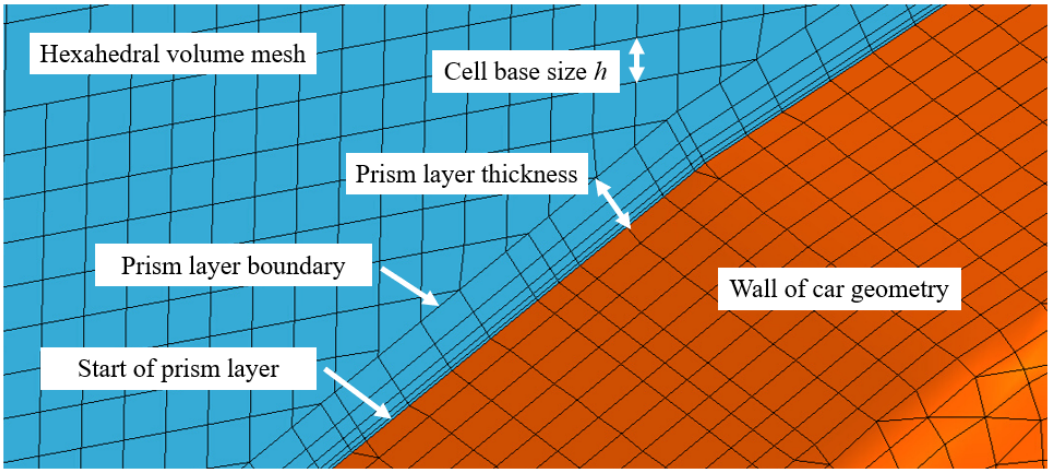


Figure 3.11: Modelling of prism layer for volume mesh

All mesh settings were applied for all three configurations, for both full size and scaled models. Three meshes (coarse, medium, and fine) were constructed for the full size mesh in order for grid convergence to be investigated. This resulted in meshes with approximately 12 million, 27 million, and 63 million cells for the coarse, medium, and fine meshes respectively.

3.4.4 Numerical Model Setup

The setup of the numerical solution was based on best practices for vehicle aerodynamics as recommended by Siemens [56]. The airflow for all numerical models was modelled as steady and incompressible. A coupled solver for calculating the governing equations was used as this provided a faster rate of solution convergence in comparison to a segregated solver, at the expense of more computational resources. The SST $k-\omega$ turbulence model was employed as this was the model recommended by Siemens [47], and has been used successfully in previous studies, such as by Stevenson [31]. The coefficient a_1 of the turbulence governing equation

was set equal to 1, as opposed to the default of 0.31. The realisability coefficient was set as 1.2. These values have been shown by Evans et al. [57] to improve the stability of the solution, and speed up convergence, while still accurately predicting flow trends. Initialisation of the solution was performed using the STAR-CCM+ grid sequencing initialisation mode. This mode initialised the grid with an inviscid solution to the flow problem, which enabled convergence to be reached faster. The CFL number was ramped linearly from 0.25 to 100, over the first 100 iterations. This improved the stability of the solution and prevented rapid divergence at the start of the iteration. A CFL number is not only applicable to unsteady simulations in STAR-CCM+. This is because for steady-state simulations in STAR-CCM+, a pseudo-transient term is used in place of the physical time derivative typically employed for unsteady simulations. This pseudo-transient term reduces to zero as the steady-state solution progresses in pseudo-time [47].

The velocity at the inlet plane was set to 60 m/s for the full size models, based on a rounded value of ∼59.8 m/s for the average speed of all Formula One tracks for the 2019 season [58]. This was chosen as the most applicable inlet velocity, as choosing a velocity based on a specific track/section of a track would not have been general enough such that the results would be relevant to as many race conditions as possible. The inlet velocity selection was incidental as this study was an exploratory work of the wake structure. The qualitative wake structure was expected to be similar at the various speeds relevant to race conditions. The inlet velocity for the scale models was set as 20 m/s such that it corresponded with the wind tunnel testing speed. A linear velocity, equal to the inlet velocity, was applied in the same direction as the airflow to the ground plane. This prevented the formation of a boundary layer along the ground surface. The wheels were assigned a rotational speed of 166.67 rad/s. This corresponded to the linear speed of 60 m/s. Two different setups were considered for the scale model, namely the implementation of rotating and non-rotating wheels. A linear speed of 20 m/s was applied to the ground plane, with a wheel rotational speed of 333.33 rad/s, for the scale model using rotating wheels. This setup corresponded to Reynolds numbers of 2.03×10^7 and 1.13×10^6 for the full size and scaled simulations respectively. While the Reynolds numbers differ by an order of magnitude, both flows are within the turbulent regime. A Reynolds number independence study was conducted (§4.2) to ascertain any differences in drag and lift coefficients, as a result of the variation in Reynolds number between the scaled and full size models. Normalised values also allow for easier comparison between models of different Reynolds numbers. While some numerical differences can be expected between the full size and scaled models, the overall wake structure would be qualitatively similar between the two sizes.

Monitors for drag coefficient, lift coefficient, mass flow rate, and maximum velocity were included as a means to check for convergence of the solution. Normalised residuals were

monitored throughout the solution. Celik et al. [59] recommended that a solution can be considered to have reached numerical convergence when all normalised residuals dropped to below at least 10^{-3}. For all numerical models, the monitored quantities adequately converged, with all normalised residuals dropping below 10^{-4}. Periodic flow features such as rotating vortices within the flow field prevent residual convergence to significantly smaller magnitudes. However, this does not imply the absence of a converged solution, as other criteria for convergence (i.e. the monitored quantities above) were met (§2.5).

3.5 Wind Tunnel Testing

Scale wind tunnel tests served as validation for the numerical model setup, by creating two-dimensional representations of the velocity distribution of the wake. By being able to compare results between wind tunnel tests and a scaled numerical model, the validity of a full size numerical model could be examined. All tests took place in the draw-down wind tunnel at the University of the Witwatersrand, shown in Figure 3.12. This wind tunnel makes use of a fan located downstream of the diffuser that sucks air through the inlet and nozzle into the test section. Honeycomb mesh flow straighteners are positioned at the test section inlet and outlet. These flow straighteners reduce the velocity components of the airflow that are not parallel to the test section length. The wind tunnel has a long test section of 11 m and an inlet area ratio of 9. This results in a low turbulence intensity which is ideal for studies pertaining to wakes and vortices.

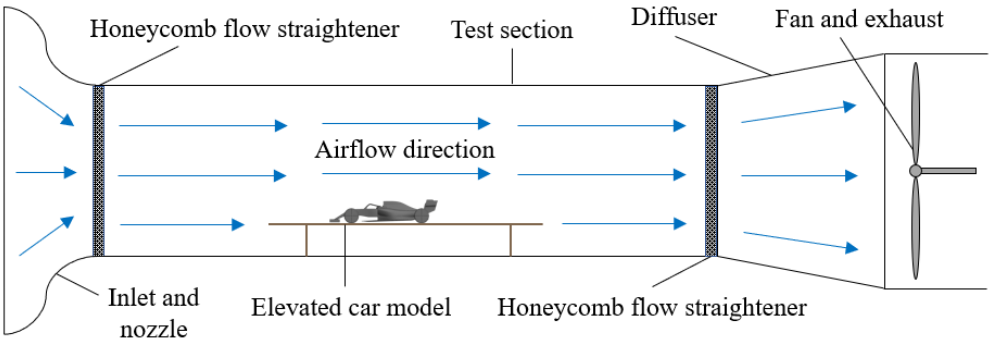


Figure 3.12: Side view of wind tunnel setup (not to scale)

A 1/6 scale model Formula One car was used for the wind tunnel tests. This model was constructed of acrylonitrile butadiene styrene (ABS) plastic and was 3D printed in parts and then assembled together. ABS plastic was chosen as when exposed to acetone vapours, the surface of these pieces smoothed out, eliminating the layered surface finish associated with 3D printing. The surface of the assembled model was further finished through sanding, after which a coat of polyurethane was applied to ensure an even surface for all parts of the model.

3.5.1 Wind Tunnel Setup

The model was placed on an elevated ground plane in the wind tunnel. This served as a means of boundary layer reduction. The wind tunnel has an octagonal cross section. The ground plane was fitted to a raised aluminium frame such that it was at a height of 330 mm above the floor of the wind tunnel. This raised the model to a height such that it was positioned at the widest possible wind tunnel cross section. This also positioned the model away from the influence of corner vortices that form along the walls of the wind tunnel. This same height was used by Stevenson [31] for tests of a Le Mans prototype that utilised the same wind tunnel facility. A five-hole probe to extract velocity data, along with a traverse mechanism, was mounted to the elevated ground plane at various characteristic lengths behind the scale model. The car was held in position by mounts through the wheels and the floor of the wind tunnel. This setup is shown in Figure 3.13.

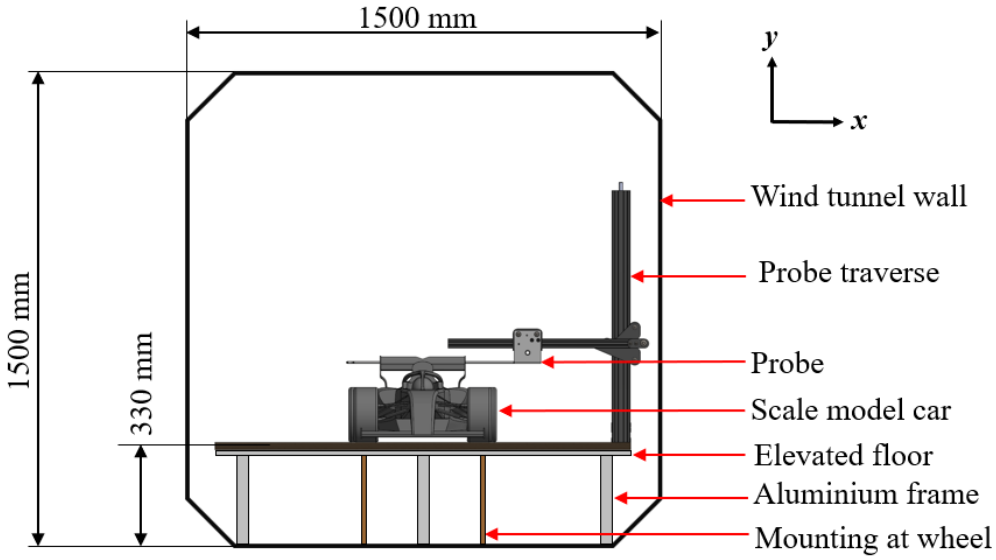


Figure 3.13: Cross sectional view of wind tunnel setup

All tests took place at the maximum wind tunnel speed in order to maximise the Reynolds number during the tests. The maximum motor speed of the wind tunnel was approximately 1500 rpm. This corresponded to a wind tunnel speed of approximately 20 m/s (for scale car, $R_e \sim 9.44 \times 10^5$), based on calibration data recorded by Atherfold [60] (calibration curve shown in Figure 3.14). Scale model CFD simulations were conducted for validation purposes, at the same Reynolds number corresponding to the wind tunnel tests.

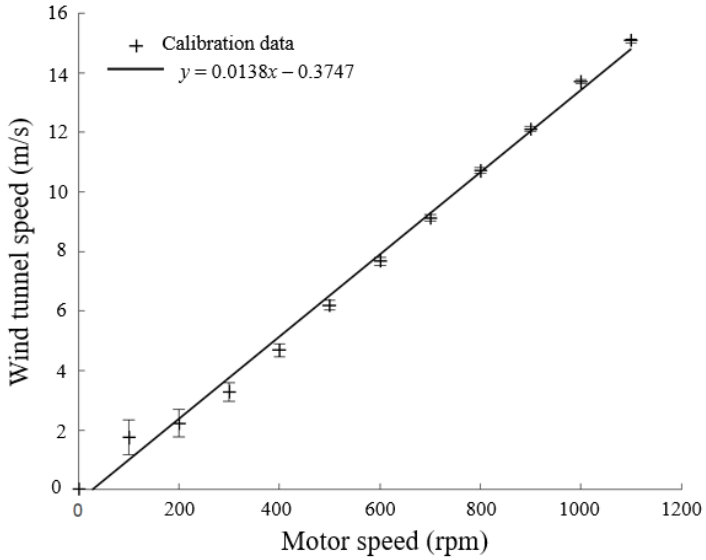


Figure 3.14: Calibration curve for draw-down wind tunnel as determined by Atherfold [60]

The elevated ground plane (shown in Figure 3.16) was constructed of medium density fibre-board. A notch was hollowed out for the placement of a mild steel boundary layer suction plate that was flush with the surface of the wooden ground plane. The suction plates were supported underneath by aluminium struts to prevent deflection during testing. The leading edge of the elevated ground plane was bevelled at a 45° angle to prevent a stagnation point upstream of the model. Without the bevelled leading edge, separation bubbles/recirculation zones tend to form as the air flow deflects around the leading edge, as shown in Figure 3.15(i). By having a bevelled leading edge (shown in 3.15(ii)), a recirculation zone only forms on the underside of the ground plane as the air moves around the sharp corner on the underside of the ground plane. This prevents recirculation zones from forming on the top surface, which may influence wake survey results.

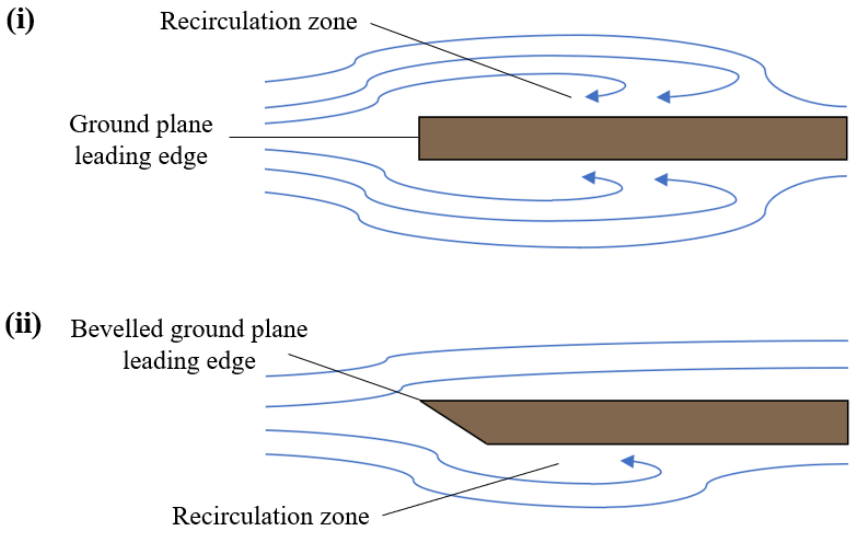


Figure 3.15: Non-bevelled (i) and bevelled (ii) ground plane leading edges

The elevated ground plane extended by a distance of $2w_c$ ahead of the model, and by a distance of $4.85w_c$ behind the model. This was based on the recommendation made by Cooper [61]. This recommendation stated that the distance of the ground plane upstream of the model should be at least two characteristic widths, and the distance downstream should be between at least 4 and 6 characteristic widths. The five-hole probe mounted to the traverse moved along the xy plane while taking measurements (directions of movement shown by yellow arrows in Figure 3.16). Each hole of the probe was connected to a separate digital manometer that provided pressure readings. The movement of the probe was controlled manually from outside the wind tunnel from an electrical control unit that was connected to the traverse mechanism.

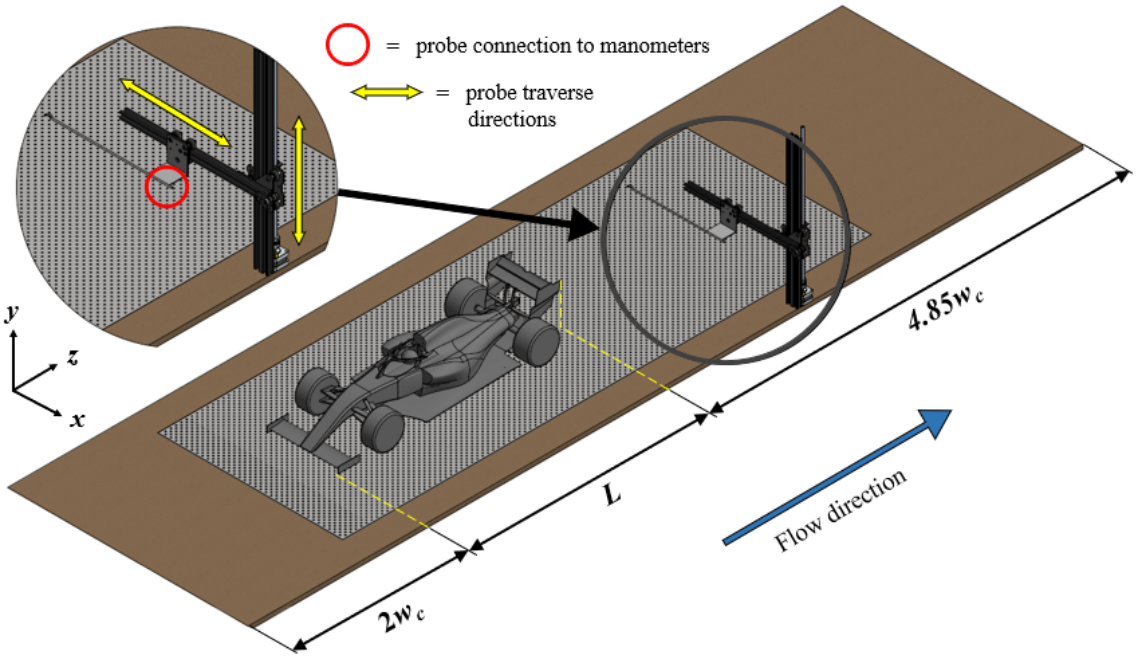


Figure 3.16: Elevated ground plane employed for wind tunnel tests

The boundary layer suction plate was designed based on the geometry employed previously by Lutz and Sayers [30]. This suction plate consisted of an upstream suction section ahead of the model. The upstream suction section consisted of 5 mm diameter holes and was responsible for removing the boundary layer that had developed from the leading edge of the elevated ground plane, along with the boundary layer formed along the gap between successive holes. This section extended backwards by 105 mm, after which the distributed suction section began. The distributed suction section consisted of 4 mm diameter holes and extended backwards by 1895 mm such that it extended past a distance of one characteristic length aft of the model. The distributed suction was responsible for removing the boundary layers formed along the plate, along the gap between successive holes. A detailed diagram of the geometry of a section of this suction plate is shown in Figure 3.17. This design

resulted in a total suction flow rate of approximately 0.8 m^3/s being required. However, in the absence of a suitable suction fan capable of such a flow rate (and of overcoming the back pressure outside of the tunnel test section), no external suction device was used. Any pressure difference between the upper and lower surface during testing would provide some degree of suction (or blowing) during testing. This approach was considered adequate based on the results of Pagliarella [34] in which a suitable replication of aerodynamic results was achieved for an Ahmed body without the use of any boundary layer removal. Furthermore, Watts and Watkins [9] obtained a qualitatively suitable wake structure of a Formula One car without the implementation of boundary layer removal.

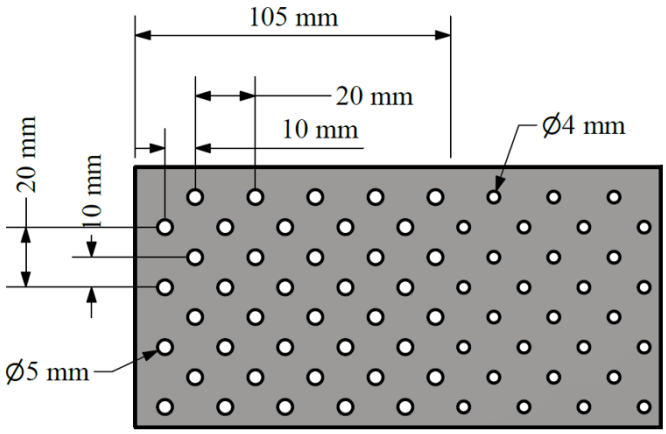


Figure 3.17: Section of boundary layer suction plate

Due to the high costs of apparatus needed for wheel rotation, the wheels were kept stationary as was the case for the study by Watts and Watkins [9]. The wind tunnel results served only as a means of validation for the numerical model, and not to investigate the difference in flow structures for the three rear wheel configurations. Thus the rotation of wheels was not considered a necessary factor for the wind tunnel tests, with stationary wheels adequately serving the purpose of validation. The car model was mounted at the wheels through the four holes of the suction plate. This prevented any mounting struts from causing any blockage effects or altering the flow underneath the car.

The five-hole probe was moved along the xy plane starting from the centreline of the car (i.e. only a half plane was surveyed). Due to the physical limitations of the traverse mechanism, a grid with a width of $0.9w_c$ and a height of $1.5h_c$ was surveyed. A grid spacing of 15 mm $\times$ 15 mm was employed, resulting in measurements being taken at 420 points for a single half-plane. This spacing was chosen to create a fine enough surveying grid, while also minimising the time for tests to be conducted. These points are indicated by the red circles in Figure 3.18. these points also served as the placement locations of tufts for flow visualisation using a tuft grid. In order to create continuous contour plots, interpolation was performed between data points over the spaces between the probing points.

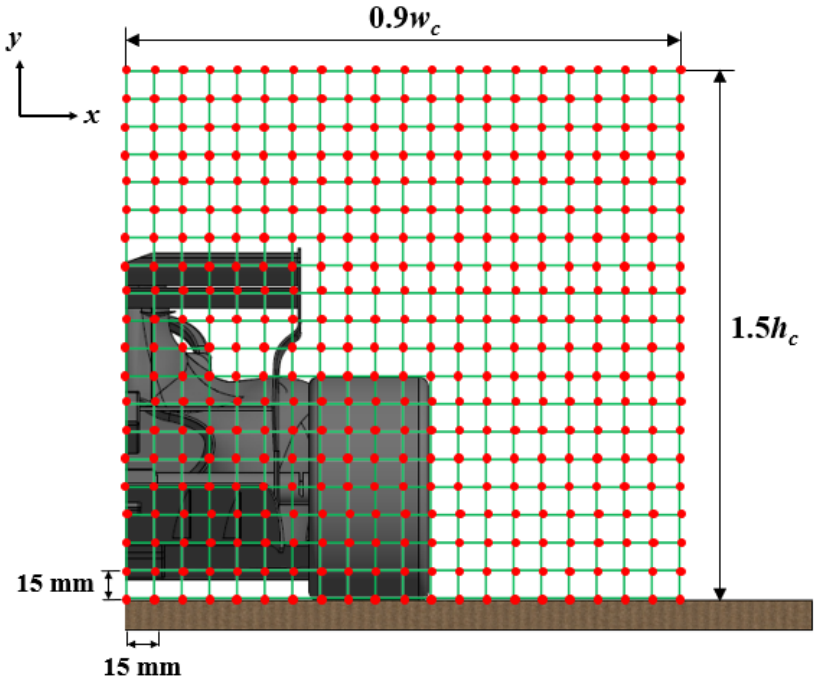


Figure 3.18: Five-hole probe traverse grid for data measurement

3.5.2 Wind Tunnel Data Processing

A labelled schematic of the five-hole probe used for the wind tunnel tests is shown in Figure 3.19. Each hole of the five-hole measured a pressure at the probe point. A non-nulling technique was used for calibration of the five-hole probe. Results from the wind tunnel tests were used in conjunction with the calibration data to extract the velocity components in x, y, and z directions (u, v, and w respectively) of the local velocity V, along with values for the pitch (α) and yaw (β) angles of the oncoming flow at each surveying point.

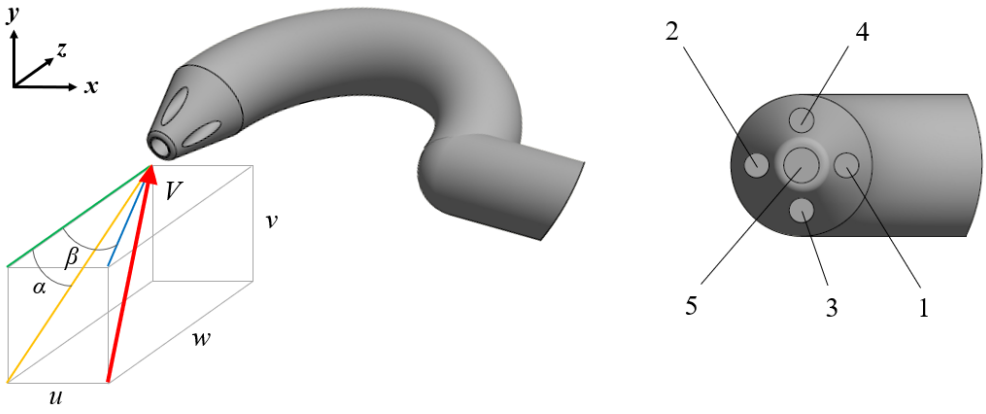


Figure 3.19: Labelled five-hole probe with velocity components and angles

Calibration was performed for pitch and yaw angles between -30° and 30°. This calibration took place at a range of air speeds, with a maximum calibration speed of approximately 20 m/s. The calibration and data processing procedure was based on a method previously laid out by Town and Camci [62]. Calibration data could be found for a specific velocity by interpolating the data within the calibration air speed range, Pressure readings for pitch (holes 3 and 4 in Figure 3.19) and yaw (holes 1 and 2 in Figure 3.19) were converted to non-dimensional pressure coefficients. The hole labelled 5 is the centre-hole and measured the total pressure in the positive z direction at each point. The pitch coefficient was calculated by:

$$C_{P_{pitch}} = \frac{P_3 - P_4}{P_5 - \overline{P}} \tag{3.1}$$

The yaw pressure coefficient was calculated by:

$$C_{P_{yaw}} = \frac{P_2 - P_1}{P_5 - \overline{P}} \tag{3.2}$$

The term $\overline{P}$ represents the average pressure of the holes of the probe (excluding that measured by the centre-hole i.e. P_5) such that:

$$\overline{P} = \frac{P_1 + P_2 + P_3 + P_4}{4} \tag{3.3}$$

The pressure coefficients for the known combinations of pitch and yaw angles during calibration were then plotted to form a carpet map shown by the points in Figure 3.20. Quadratic lines of best fit was plotted between points of constant pitch and yaw. Lines for pitch and yaw angles beyond the calibration range were then extrapolated. This was done by extrapolating the coefficients of the quadratic lines of best fit for the known calibration angles. Equations for lines for these pitch and yaw angles beyond the calibration range could then be plotted. These are shown in Figure 3.20 as the lines with no plotted data points.

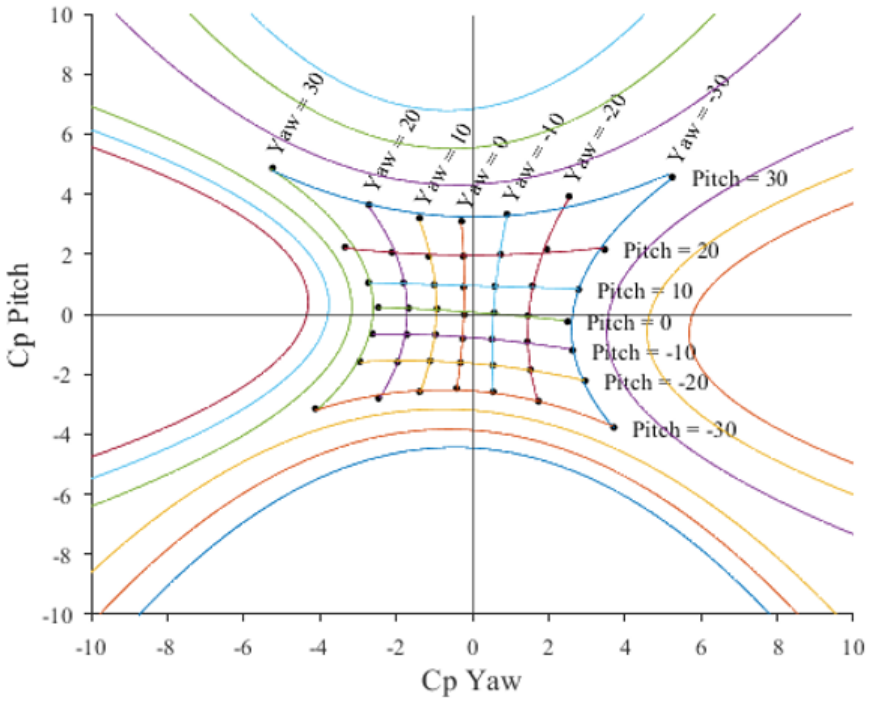


Figure 3.20: Carpet map of calibration data showing lines of constant pitch and yaws angles

Non-dimensional pressure coefficients for the total and static pressure were then calculated. The total pressure coefficient was given by:

$$C_{P_{total}} = \frac{P_5 - P_{total}}{P_5 - \overline{P}} \tag{3.4}$$

The static pressure coefficient was given by:

$$C_{P_{static}} = \frac{\overline{P} - P_{static}}{P_5 - \overline{P}} \tag{3.5}$$

The pressure coefficients for total and static pressure were then plotted, with lines of constant yaw angle, as a function of pitch angle. These are shown in Figures 3.21 and 3.22 respectively.

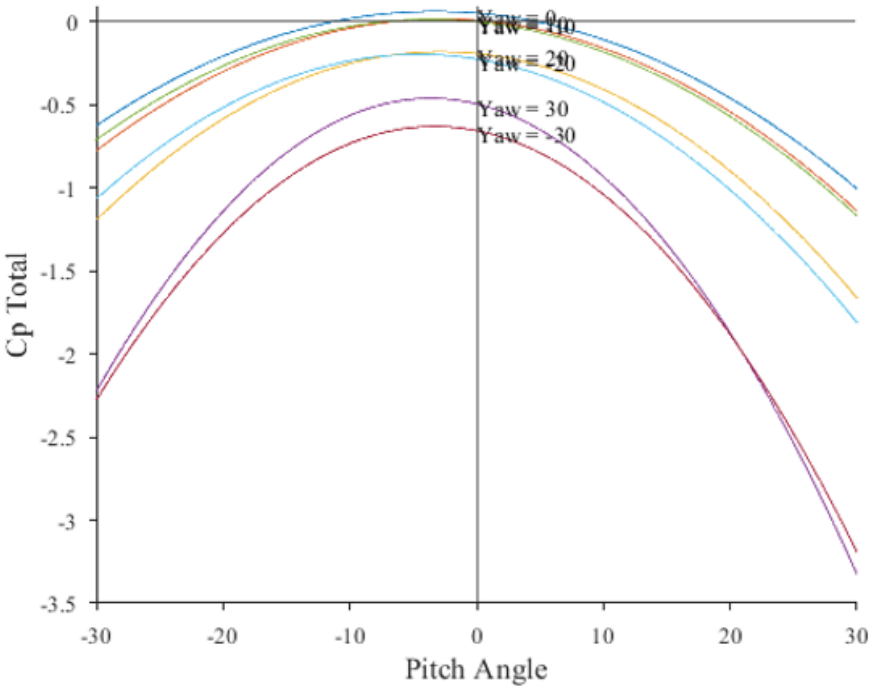


Figure 3.21: Total pressure coefficient versus pitch angles with lines of constant yaw angle for calibration data

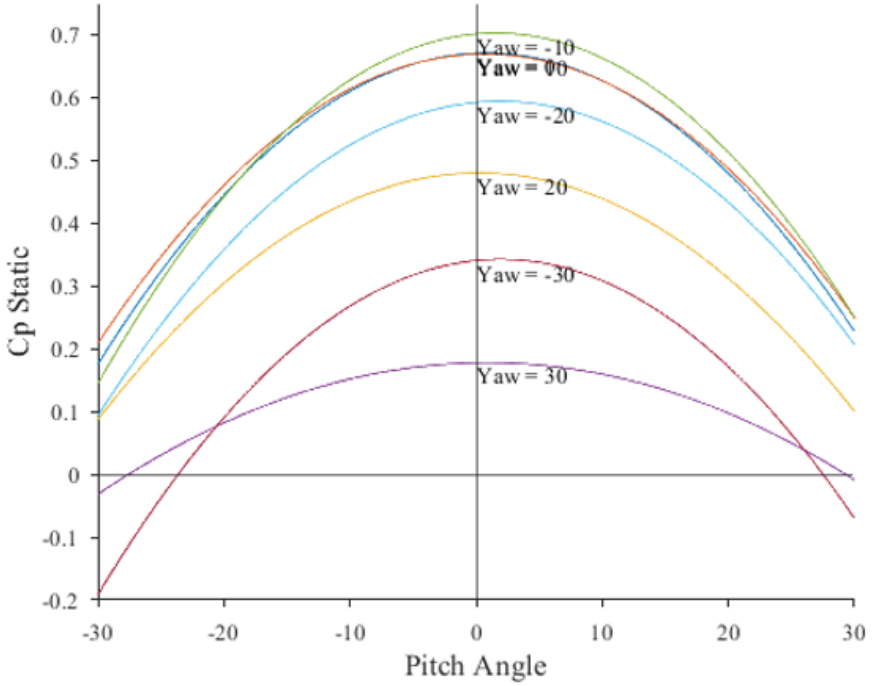


Figure 3.22: Static pressure coefficient versus pitch angles with lines of constant yaw angle for calibration data

The experimental data is then used in conjunction with the calibration data to extract the velocity components though a series of linear interpolations. This was done by calculating the pitch and yaw pressure coefficients, along with the average pressure, at each point measured by the five-hole probe. The yaw pressure coefficient was compared to the calibration data of the carpet map (Figure 3.20). This was done by extracting the range of pitch pressure coefficients that the calculated yaw pressure coefficient spanned. These extracted pitch pressure coefficients were then compared to the calculated local pitch pressure coefficient, which enabled the pitch angle (α) to be determined. The yaw angle (β) was then determined by using the calculated pitch angle value and extracting the yaw pressure coefficients this pitch angle spanned. The calculated local yaw pressure coefficient was then compared to these values to determine the yaw angle.

The pitch angle value, along with the extracted pitch angles, were then used to extract a range of total pressure coefficients from the calibration data (Figure 3.21). The yaw angle value was then used to extract the local total pressure coefficient. This same procedure using the local pitch and yaw angle values was used to extract the local static pressure coefficient from the calibration data in Figure 3.22.

The local total and static pressure at the probe point were then calculated using the local total and static pressure coefficients. The total pressure at the probe point is given by:

$$P_{total} = P_5 - C_{P_{total}} \left(P_5 - \overline{P}\right) \tag{3.6}$$

The static pressure at the probe point is given by:

$$P_{static} = \overline{P} - C_{P_{static}} \left(P_5 - \overline{P}\right) \tag{3.7}$$

The total and static pressure coefficients were then used to calculate the magnitude of the velocity at the probe point by using Bernoulli's equation:

$$V = \sqrt{\frac{2\left(P_{total} - P_{static}\right)}{\rho_a}} \tag{3.8}$$

Finally, the local velocity components (u, v, and w), as shown in Figure 3.19, were calculated using the local velocity value (V), along with the pitch (α) and yaw (β) values.

The velocity component in the x direction, u was given by:

$$u = V \cos\alpha \, \sin\beta \tag{3.9}$$

The velocity component in the y direction, v was given by:

$$v = V \sin\alpha \tag{3.10}$$

The velocity component in the z direction, w was given by:

$$w = V \cos\alpha \, \cos\beta \tag{3.11}$$

This data processing procedure was automated by means of a MATLAB function. The code for this function can be found in Appendix C. The precision associated with the five-hole probe is small, with the repeated measurements at each probe location being within a range of approximately 5 Pa. The sensitivity associated with the probes correlated to the digital manometers used to measure each pressure during calibration and testing. The same Fluke 922 digital manometers were utilised during calibration and testing, with the same specifications for each manometer measuring the different pressures at each hole of the probe. The sensitivity of the digital manometers, as per the manufacturers specifications [63], is 1 Pa. In the absence of available manufacture specifications for the digital barometer and hygrometer, the sensitivity of these instruments was assumed to be the smallest measurable increment. This correlated to sensitives of 0.1 mbar, 0.1 C, and 1% for the readings of atmospheric pressure, temperature, and relative humidity respectively. A full uncertainty analysis of error propagation during the experimental data processing, based on the procedure recommended by Holman [64], is provided in Appendix B.

3.6 Summary of Method

The highlighted research method was developed utilising recommended and previously used techniques in order to successfully achieve the stated objectives. Numerical simulations were employed to interrogate the different wake structures of cars with partial and full fairings, using a car with no wheel fairings as a baseline comparison. The wake was interrogated in two-dimensional planes at various distances downstream of each car configuration. Mid-planes of the car and rear wheels were also investigated. In addition, numerical models were used to investigate the change in force coefficients (drag and lift) of a trailing car positioned in this wake. This was done by simulating a trailing car (for each configuration) behind a lead car in various downstream positions. The drag and lift coefficient for the trailing car could then be extracted to determine the aerodynamic effects of the fairings on the performance of a trailing car.

The numerical models have been set up using recommended standards for vehicle aerodynamics and were verified as accurate. This was done with 1/6 scale model wind tunnel tests designed to confirm the validity of the numerical model. Wake surveys utilising five-hole probe pressure measurements were conducted, with measurements taken at numerous probing points in a predefined two-dimensional grid aft of the scale model. These readings were then processed to create two-dimensional colour-flooded plots that represented the wake structure at locations downstream of each car configuration. Furthermore, flow visualisation with tuft grids was done to ensure the wake structures from the five-hole probe colour plots were correctly resolved.

The research method would thus provide results that appropriately meet the stated objectives, indicating either the benefit or adverse aerodynamic effect of covering the rear wheels of a Formula One car.

Chapter 4

Validation and Verification

4.1 Numerical Simulations

The presented discussion of validation and verification of the numerical simulations, pertains only to the full size no wheel fairing configuration, unless otherwise stated. The normalised residuals dropped to the desired level of below 10^{-3} as recommended by Celik et al. [59]. The monitored quantities of drag and lift coefficient, mass inflow and outflow, and maximum velocity converged to steady values. The three velocity components (u, v, *and* w) were then extracted at each cell for the predefined survey planes (shown in Figure 3.1, §3.2). All colour-flooded plots/contours were created using custom macros that normalised the w velocity component with respect to the freestream velocity. The velocity components u and v were used to create planar streamtraces in the xy plane. All distances used as the plot axes were normalised by the respective characteristic dimension of the car.

A sample resultant contour plot at a plane of $z = 0.5L$ is presented in Figure 4.1(i). The previously seen 'mushroom-like' wake structure was achieved. In Figure 4.1(ii), the wake structure at the same aft plane as found by Newbon et al. [10] is shown. The same flow phenomena were noted between the presented and previous studies. The region labelled B in both contour plots correlated to the lower normalised axial velocity region of rear wing-tip vortices. The region labelled C in both contour plots indicated a centreline column of low axial velocity airflow, and thus a dynamic pressure deficit. The low axial velocity to the side of the rear wheel (labelled A) extended further outwards from the car centreline for the presented study. This was attributed to the different car geometries used for the different studies. Overall, the same qualitative wake structure was achieved, thus giving confidence in the numerical model setup.

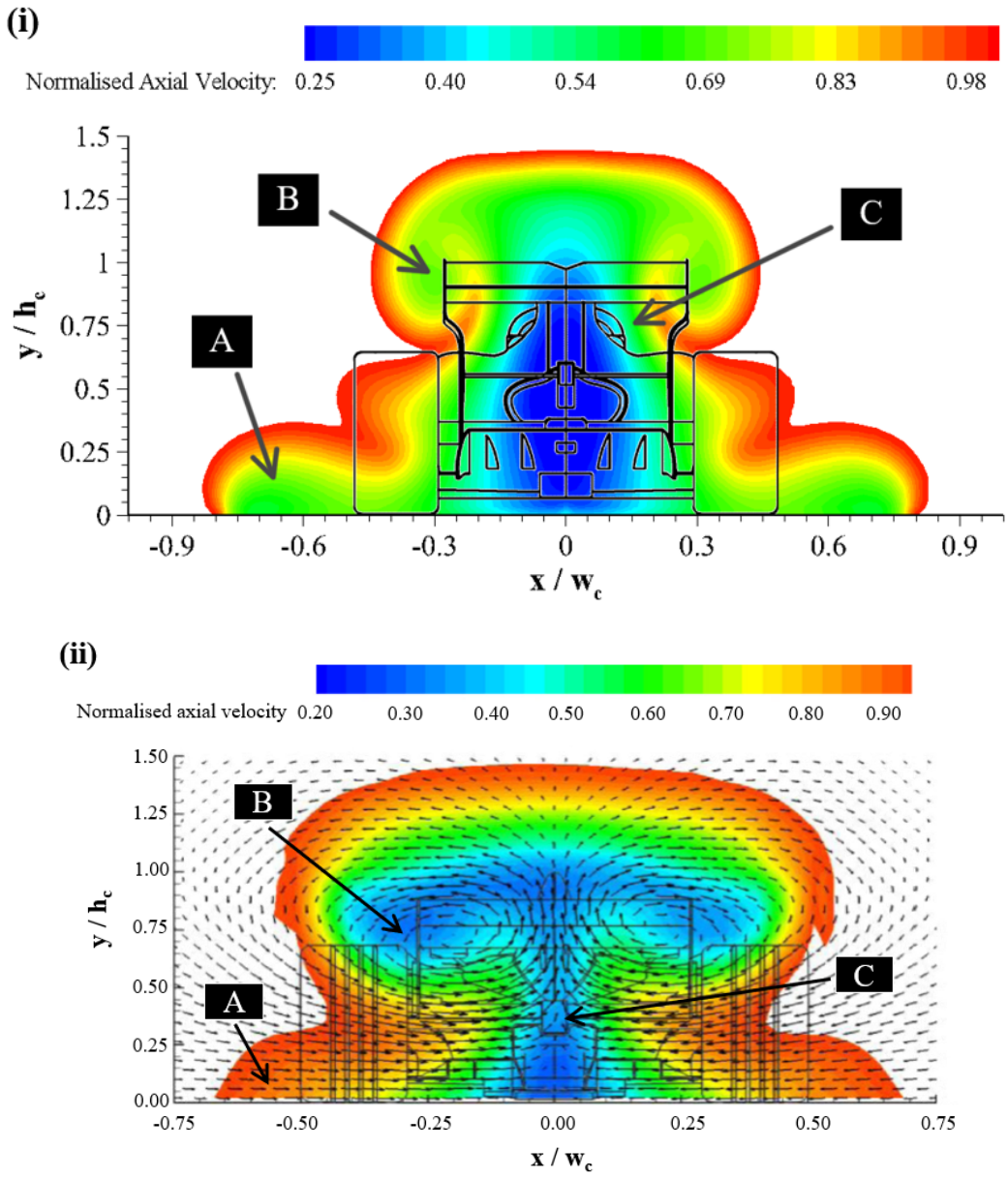


Figure 4.1: Numerical simulation velocity contours for no wheel fairings at $z = 0.5L$ (i), compared to contours by Newbon et al. [10] (ii)

4.1.1 Wall Treatment

A target $y+$ value of 50 was chosen for the surfaces of the car (i.e. to model the log law region of the turbulent boundary layer). As seen in Figure 4.2, a wall $y+$ value of between approximately 50 and 70 was achieved over a large portion of the surface of the car. However, at certain locations, the target $y+$ value was not achieved. At the front and rear wheels (labelled A and B), the $y+$ value was as high as 150. This was caused by the rotation of

the wheels. Because of the varying relative velocity between the rotating wheel tread and oncoming airflow, boundary layer growth was not possible here. Thus the high $y+$ values here indicated very little boundary layer growth. Towards the rear of the vehicle (labelled C), the wall $y+$ values were lower than the target value of 50. This value was as low as 30. This was attributed to upstream flow separation. Downstream of the separation points, reattachment points existed where new boundary layer growth began. Thus the boundary layer would not have been as developed in this region, leading to the lower $y+$ values. However, the $y+$ values here were still within the log-law region, and $y+$ values applicable to the buffer layer region were mostly avoided.

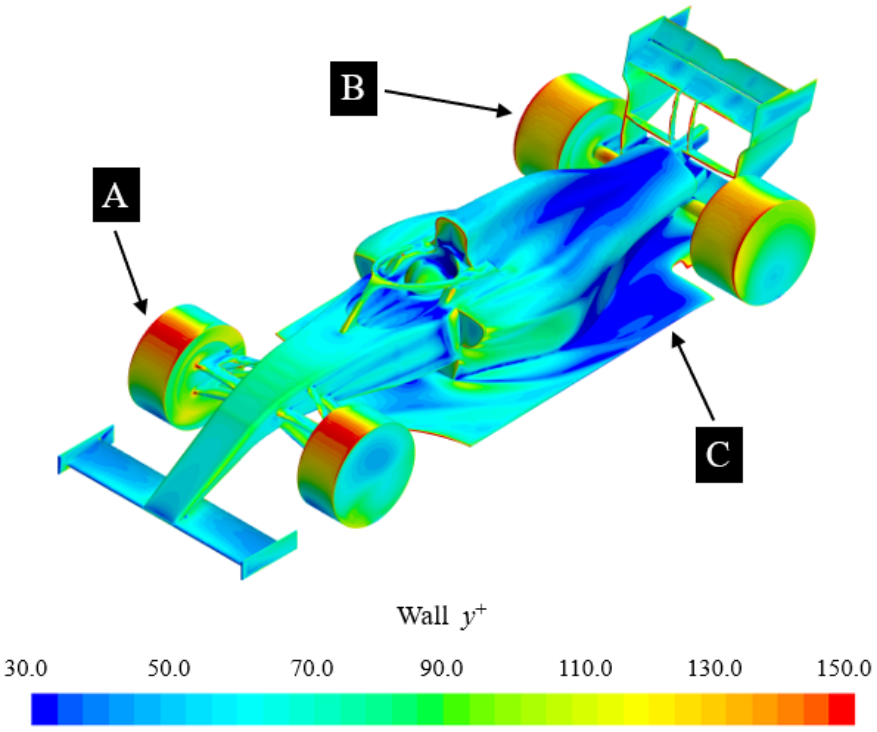


Figure 4.2: Wall $y+$ distribution for no wheel fairing configuration

4.1.2 Mesh Independence Study

A constant refinement ratio of 4/3 was used between the base cell sizes of the different meshes. The drag and lift coefficients were used as the monitored quantities of interest in judging mesh independence. The grid convergence indices based on drag coefficients in Table 4.1 show a maximum grid convergence index (GCI) value (as defined in §2.5.4) of 0.163%, 0.577%, and 0.350% for the no fairing, partial fairing, and full fairing configurations respectively.

Table 4.1: Grid convergence indices (GCI) for drag coefficient (C_D)

Rear Wheel Configuration	Mesh	C_D	GCI_{12} (%)	GCI_{23} (%)	GCI Ratio
No Wheel Fairings	Coarse	0.788	0.096	0.163	0.999
	Medium	0.771			
	Fine	0.770			
Partial Wheel Fairings	Coarse	0.801	0.107	0.577	0.996
	Medium	0.785			
	Fine	0.782			
Full Wheel Fairings	Coarse	0.802	0.029	0.350	0.997
	Medium	0.778			
	Fine	0.776			

The grid convergence indices based on lift coefficients in Table 4.2 show a maximum GCI value of 0.170%, 0.618%, and 1.27% for the no fairing, partial fairing, and full fairing configuration respectively.

Table 4.2: Grid convergence indices (GCI) for lift coefficient (C_L)

Rear Wheel Configuration	Mesh	C_L	GCI_{12} (%)	GCI_{23} (%)	GCI Ratio
No Wheel Fairings	Coarse	0.634	0.0021	0.170	1.00
	Medium	0.713			
	Fine	0.714			
Partial Wheel Fairings	Coarse	0.485	0.0235	0.618	1.01
	Medium	0.553			
	Fine	0.556			
Full Wheel Fairings	Coarse	0.456	0.0753	1.27	1.01
	Medium	0.544			
	Fine	0.549			

The grid convergence indices indicated that the error band associated with the drag and lift coefficients at zero grid spacing were small and thus within an acceptable range. All grid GCI ratios were within 1% of unity. This indicated that the monitored quantities of drag and lift coefficient for all meshes, of all three configurations, were within the desired asymptotic range of convergence.

Mesh independence was tested by considering the change in monitored quantities caused by changing the number of mesh cells. The two monitored quantities of interest were the drag and lift coefficients for each rear wheel configuration for the full size simulations. The drag coefficient versus number of cells is shown in Figure 4.3. For the no wheel fairing configuration, refinement from a coarse mesh to a medium mesh resulted in a 2.05% decrease in drag coefficient, and refinement from a medium mesh to a fine mesh resulted in a 0.13% decrease in drag coefficient. For the partial wheel fairing configuration, refinement from a

coarse mesh to a medium mesh resulted in a 2.02% decrease in drag coefficient, and refinement from a medium mesh to a fine mesh resulted in a 0.38% decrease in drag coefficient. For the full wheel fairing configuration, refinement from a coarse mesh to a medium mesh resulted in a 3.04% decrease in drag coefficient, and refinement from a medium mesh to a fine mesh resulted in a 0.26% decrease in drag coefficient.

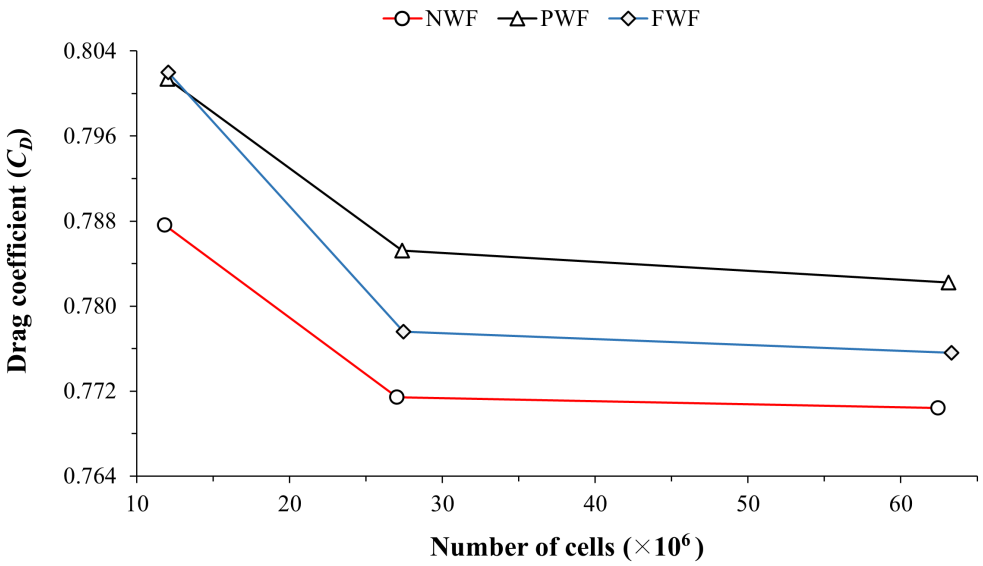


Figure 4.3: Converged drag coefficient value of car versus number of mesh cells

The lift coefficient versus number of cells is shown in Figure 4.4. For the no wheel fairing configuration, refinement from a coarse mesh to a medium mesh resulted in a 12.5% increase in lift coefficient, and refinement from a medium mesh to a fine mesh resulted in a 0.11% increase in lift coefficient. For the partial wheel fairing configuration, refinement from a coarse mesh to a medium mesh resulted in a 14.2% increase in lift coefficient, and refinement from a medium mesh to a fine mesh resulted in a 0.47% increase in lift coefficient. For the full wheel fairing configuration, refinement from a coarse mesh to a medium mesh resulted in a 19.2% increase in lift coefficient, and refinement from a medium mesh to a fine mesh resulted in a 0.96% increase in lift coefficient.

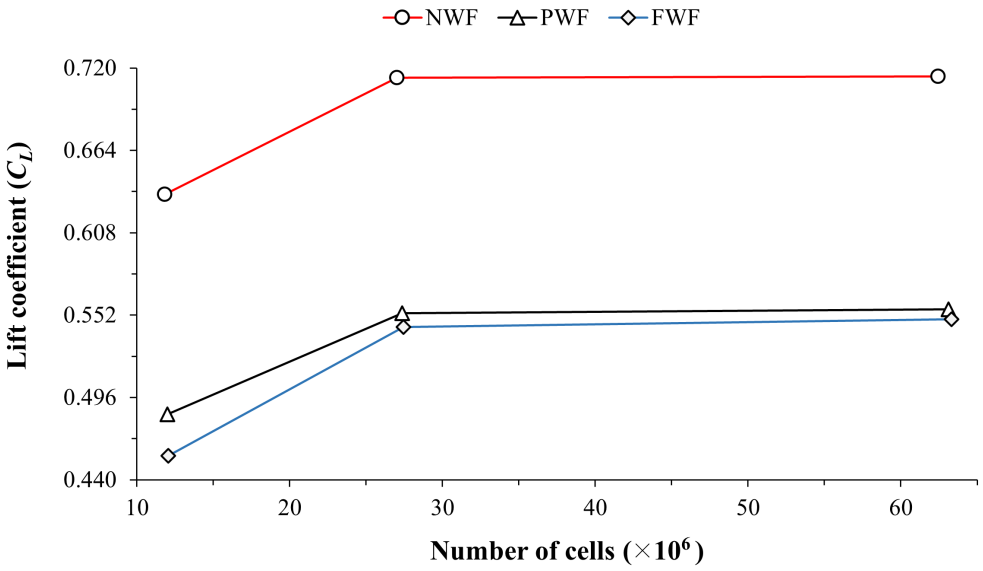


Figure 4.4: Converged lift coefficient value of car versus number of mesh cells

The change in mesh refinement resulted in insignificant changes in drag coefficients for all three configurations. However, the change from a coarse refinement level to a medium refinement level caused noticeable increases in lift coefficient (as high as 19.2%). The change from a medium refinement level to a fine refinement level caused minor percentage changes to the lift coefficients. Thus utilising the medium level of refinement, mesh independent solutions were achieved for all three full size rear wheel configurations.

4.1.3 Sensitivity to Domain Size

In order to ascertain if the boundaries of the domain were far enough away from the walls of the car, the size of the domain was changed in order to evaluate the effect on the converged drag and lift coefficients. The distance of the domain top, side, inlet, and outlet boundaries from the car was varied. This was achieved by increasing and decreasing the distances of these boundaries by one characteristic dimension (as seen in Figure 3.5, §3.4.1) to form a larger and smaller domain respectively. This sensitivity test was done in accordance with that done by Mo et al. [65]. For the full size no wheel fairing configuration, reducing the domain size increased the drag coefficient by 0.51% and decreased the lift coefficient by 4.47%. Extending the domain size decreased the drag and lift coefficients by 0.68% and 4.23% respectively. Both modifications to the domain size produced small changes to the overall drag and lift coefficients of the car, and thus the positions of the domain boundaries were seen to not greatly influence the results. The domain boundaries were concluded to be a suitable distance away from the model.

4.2 Reynolds Number Independence

The comparison of drag and lift coefficients was made between the full size and scaled numerical models for all configurations, in order to ascertain if the solution was independent of the Reynolds number of the flow regime. The Reynolds numbers for the full size and scaled models were 2.03×10^7 and 1.13×10^6 respectively (with a characteristic length equal to the car length of 5304 mm and 884 mm for the full size and scaled models respectively). These values are shown in Table 4.3.

For the no wheel fairing configuration, the differences in drag coefficient between the full size model, and scaled numerical models (with rotating and stationary wheels) were 4.9% and 0.03% respectively. The differences in lift coefficient between the full size model and scaled numerical models (with rotating and stationary wheels) were equal to 7.4% and 34.7% respectively. These discrepancies in lift coefficient between the full size and scale models was due to the difference in Reynolds numbers for the two models. The higher Reynolds number of the full size model was associated with a larger turbulent boundary layer along the car. This larger turbulent boundary layer would have resulted in delayed separation in comparison to the scale model, leading to higher downforce generated by the full size car. The scale model, with the lower associated Reynolds number, may have been partially stalled due to the earlier separation. This would have caused lower downforce generation, while changes in drag remained less noticeable.

For the partial wheel fairing configuration, the differences in drag coefficient between the full size model, and scaled numerical models (with rotating and stationary wheels) were 11.6% and 9.19% respectively. The differences in lift coefficient between the full size model, and scaled numerical models (with rotating and stationary wheels) were equal to 14.1% and 16.3% respectively.

For the full wheel fairing configuration, the differences in drag coefficient between the full size model, and scaled numerical models (with rotating and stationary wheels) were 0.63% and 2.00% respectively. The differences in lift coefficient between the full size model, and scaled numerical models (with rotating and stationary wheels) were equal to 14.6% and 17.7% respectively.

Table 4.3: Drag and lift coefficients for different numerical setups

Rear Wheel Configuration	Car Size	Drag Coefficient (C_D)	Lift Coefficient (C_L)
No wheel fairings	Full Size	0.788	0.634
	1/6 Scale - Rotating Wheels	0.827	0.589
	1/6 Scale - Stationary Wheels	0.787	0.447
Partial wheel fairings	Full Size	0.727	0.485
	1/6 Scale - Rotating Wheels	0.817	0.421
	1/6 Scale - Stationary Wheels	0.797	0.412
Full wheel fairings	Full Size	0.802	0.456
	1/6 Scale - Rotating Wheels	0.807	0.394
	1/6 Scale - Stationary Wheels	0.786	0.382

The difference in drag coefficients was smaller between the different numerical model sizes than the differences in lift coefficients. Overall, the percentage differences were quite large in some cases. This was not of particular concern for the stationary wheel models, as the Reynolds number did not take into account wheel motion. These large differences at different Reynolds number indicated that the solution could not be seen to be independent of Reynolds number. This was due to the high speed of the full size models. Reynolds number independence is thus more easily achieved for low speed ground vehicles such as commercial cars. Due to the scaling of the car, it would have been necessary to substantially increase the velocity for the scaled model (to values close to supersonic speeds), or substantially decrease the full-size CFD inlet velocity, to more appropriately match the Reynolds numbers. This would have introduced compressibility effects which are not present for Formula One aerodynamics, as well as have been beyond the physical capabilities of the utilised wind tunnel. Differences were thus present in the flow fields around the full size and scale models. While these differences resulted in variations in drag and lift coefficients between the different size models, significant similarity still existed in the structures of the wakes. The scale model tests could still provide an indication of the overall nature/structure of the wake. Force data was not of primary importance for the scale model tests. This highlighted the limitations of scale model tests for high speed vehicle aerodynamic testing. Scale model tests are effective for validating numerical model setups, that can then be applied to full size models. After the numerical model was validated, full size models could then be utilised to fully understand the aerodynamic performance of a car, along with a more detailed understanding of the wake structure. It must be noted that the simplification of the wings as standard airfoils presents a limitation on the use of this data outside of this study. The standard airfoils are more prone to flow separation than an actual Formula One front/rear wing (with associated complex geometry). This simplification was made in order to easily manufacture the scale model for wind tunnel tests. While this limitation on the use of data outside of this study exists, no

such limitation exists on the understanding of the flow field. This is because the flow fields are qualitatively similar irrespective of the wing geometry (§4.1).

4.3 Wind Tunnel Wake Survey

The results presented in this section pertain to the plane $z = 0.5L$ for the no wheel fairing configuration, unless otherwise stated. This section demonstrates the collection and processing of experimental data as used to verify and validate the results presented in subsequent chapters. Table 4.4 below shows raw data from two randomly selected probe locations during wind tunnel testing. The only measurements taken during testing were the five pressure readings of the five-hole probe ports (namely P_1 – P_5). Five measurements for each pressure reading were taken at each probing location. The readings at each probing location are automatically time averaged by the digital manometer over a small time scale, and thus the readings provided are representative of steady conditions – potential unsteadiness in the flow field is not considered. The data was then processed according to the procedure shown previously (§3.5.2). Pressure coefficients for yaw and pitch were then calculated for each of the five separate measurements, according to equations 3.1 – 3.3. The relevant blockage factors (§2.3.6) were accounted for when calculating the final velocity values.

Table 4.4: Sample set of data of wind tunnel wake survey for no wheel fairings at $z = 0.5L$

x	y	P_1	P_2	P_3	P_4	P_5	$C_{P_{yaw}}$	$C_{P_{pitch}}$
150	150	-276	-256	-301	-223	-134	0.154	-0.601
		-277	-258	-302	-225	-136	0.147	-0.594
		-274	-256	-301	-221	-133	0.138	-0.615
		-275	-258	-305	-224	-136	0.131	-0.626
		-275	-254	-299	-222	-132	0.161	-0.590
150	165	-252	-250	-291	-211	-110	0.014	-0.567
		-252	-249	-289	-209	-107	0.021	-0.560
		-254	-250	-291	-209	-106	-0.028	-0.566
		-254	-251	-291	-212	-110	0.021	-0.556
		-254	-251	-291	-210	-108	-0.021	-0.564

The average values between the five yaw and pitch pressure coefficients at each probing location were compared to a carpet map based on calibration data (such as that shown in Figure 4.5(i)). The layout of these calibration data carpet maps was found to be similar to that found by Town and Camci [62], shown in Figure 4.5(ii), with quadratic lines of best fit for lines of constant yaw and pitch angles. This gave a high level of confidence in the calibration procedure and results.

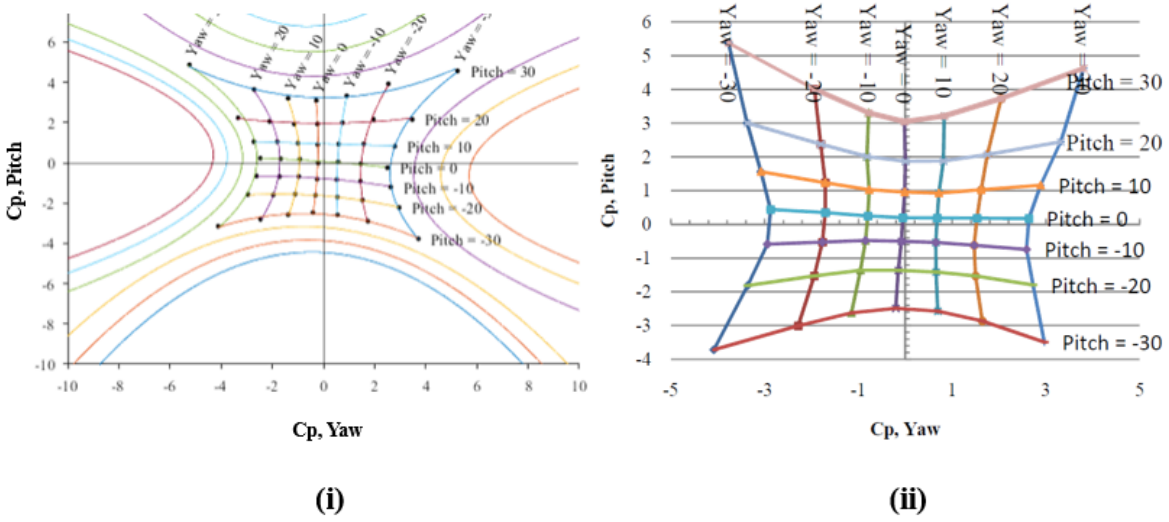


Figure 4.5: Carpet map from calibration data(i), compared to carpet map by Town and Camci (ii) [62]

A series of linear interpolations was performed by means of a MATLAB function (presented in Appendix C). This incorporated total and static pressure values at each probe location, along with trigonometric relations (equations 3.4 – 3.11), to extract the three dimensional velocity components u, v, and w. These velocities could then be plotted as colour flooded plots (or contours) at normalised probing point locations, which resulted in figures such as that shown in Figure 4.6(i). The produced contour displayed the 'mushroom-like' wake structure as previously described by Watts and Watkins [9] (shown in Figure 4.6(ii)). Three distinct flow phenomena were observed. To the sides of the rear wing, an increased axial velocity core was present which correlated to the core of a forming vortex. A low axial velocity column also existed at the centreline of the car. A low-axial velocity region was present to the sides of the wheels. These phenomena correspond to labels A, B, and C in Figures 4.6(i) and (ii) respectively. Thus the previously seen overall qualitative wake structure was replicated in the current study.

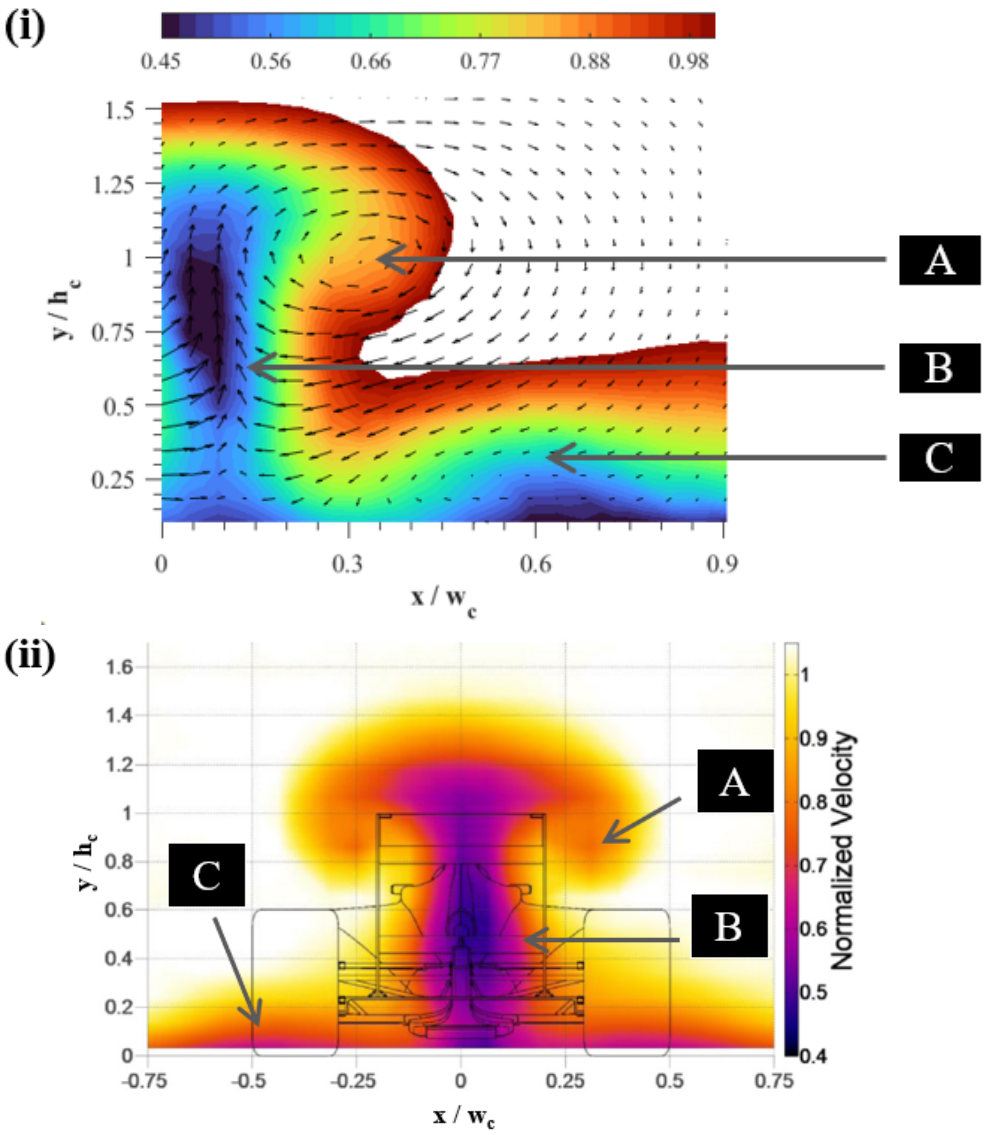


Figure 4.6: Wind tunnel velocity contours for no wheel fairings at $z = 0.5L$ (i), compared to contours by Watts and Watkins [9] (ii)

4.3.1 Repeatability of Wind Tunnel Wake Survey

A wind tunnel test at an axial distance of $z = 0.5L$ was repeated for the full fairing configuration in order to ascertain if the results could be considered repeatable. The contours for original test and repeated test 4.7(i) and (ii) respectively showed a good level of correlation. The vortex emanating from the rear wing (labelled A) had a core at the coordinates of $x = 0.32w_c$ and $y = 0.98h_c$ for both the original and repeated test. The height of the centreline column of low axial velocity flow (labelled B), with a normalised value of ~0.25,

had a normalised height of 0.317 for the original test, and 0.397 for the repeated test. This represented a 22.4% difference between the original and repeated test. The low velocity core of the vortex to the side of the rear wheel (labelled C) started at a distance of $x = 0.67w_c$ for both the original and repeated tests. However, this region had a normalised width of 0.14 and 0.18 for the original and repeated tests respectively. This indicated a 25% difference between the two tests. This was due to the inlet disturbances characteristic of draw-down wind tunnels. These disturbances are caused by varying atmospheric conditions outside the wind tunnel test section, or the absence of adequate flow straighteners upstream of the model. The planar arrows for both tests, indicating the flow direction, showed diagonally downward inwash towards the centreline, which formed upwash. This upwash then turned into vortices upon reaching the height of the rear wing.

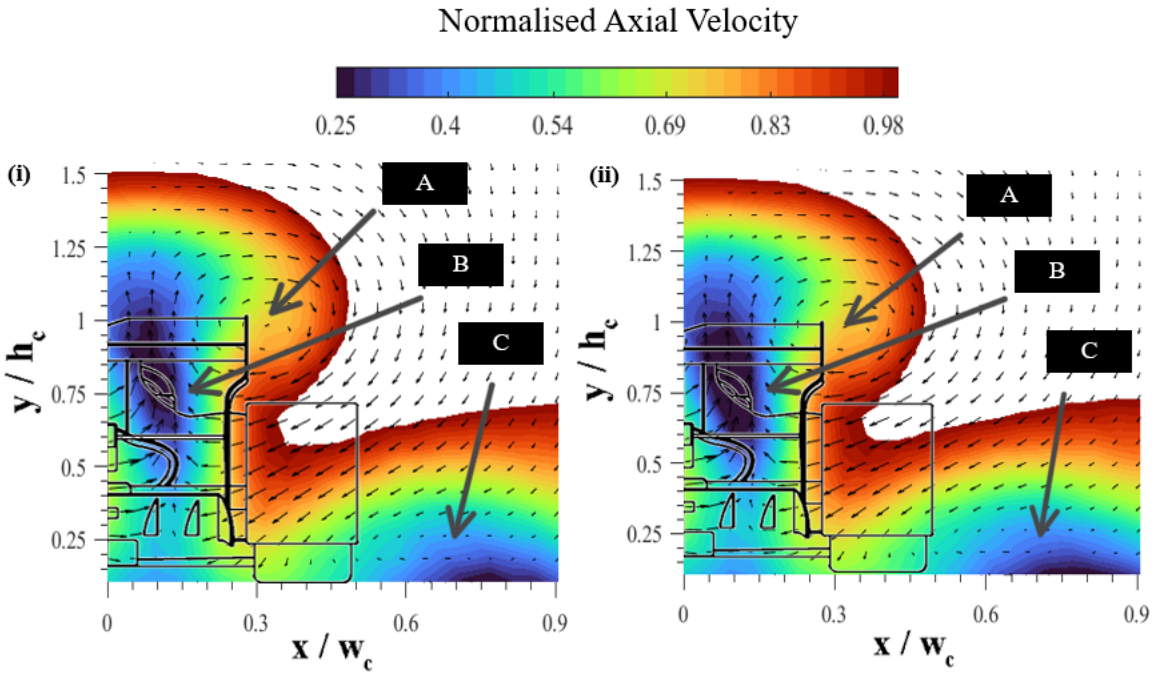


Figure 4.7: Repeatability of scale model normalised axial velocity contours for full wheel fairings at $z = 0.5L$ for wind tunnel tests

Despite the difference in size of the low velocity regions, the overall structure of the wake at this length was mostly identical. These were the only discernable differences between the tests, and thus it was concluded that the wind tunnel test were repeatable.

4.3.2 Symmetry of Wind Tunnel Wake Survey

A wind tunnel test on the other half-plane of the car with full wheel fairings was conducted to determine if the assumption of symmetry, and thus surveying the wake of only half the car, was a correct one. This symmetry test in Figure 4.8(i) yielded a near mirror image of

the original test in 4.8(ii). The general flow structure remained the same for both tests. An inwash towards the centreline became centreline upwash that then formed counter-rotating vortices at the tips of the rear wing. The core of the rear wing vortex (labelled A) for the symmetry test had a centre at $0.27w_c$ and $y = 0.98h_c$. The height of this core was thus unchanged but there was a 16.9% difference in the width position. Another noticeable difference between the two tests is that the symmetry test did not yield a centreline region of axial velocity (labelled B) of $\sim$0.25. This region still consisted of low velocity axial flow but with values of $\sim$0.4. These two difference indicated that the five-hole probe probe had slight horizontal offset for the tests, with the probe tip not mounted perfectly at the centreline for these readings. The vortex to the side of the rear wheel (labelled C) for the symmetry test still began at approximately $x = 0.67w_c$ but had a higher normalised axial velocity value of $\sim$0.32 in comparison to $\sim$0.25 for the original test. This was attributed to the positioning of the scale car model. The model was not mounted exactly in the centre of the wind tunnel, in order to reduce the blockage effects during survey of the half-plane of the original tests. The half-plane measured for the symmetry test was closer to the wind tunnel wall and affected more greatly by the blockage, causing the airflow to be at a higher speed in this vortex.

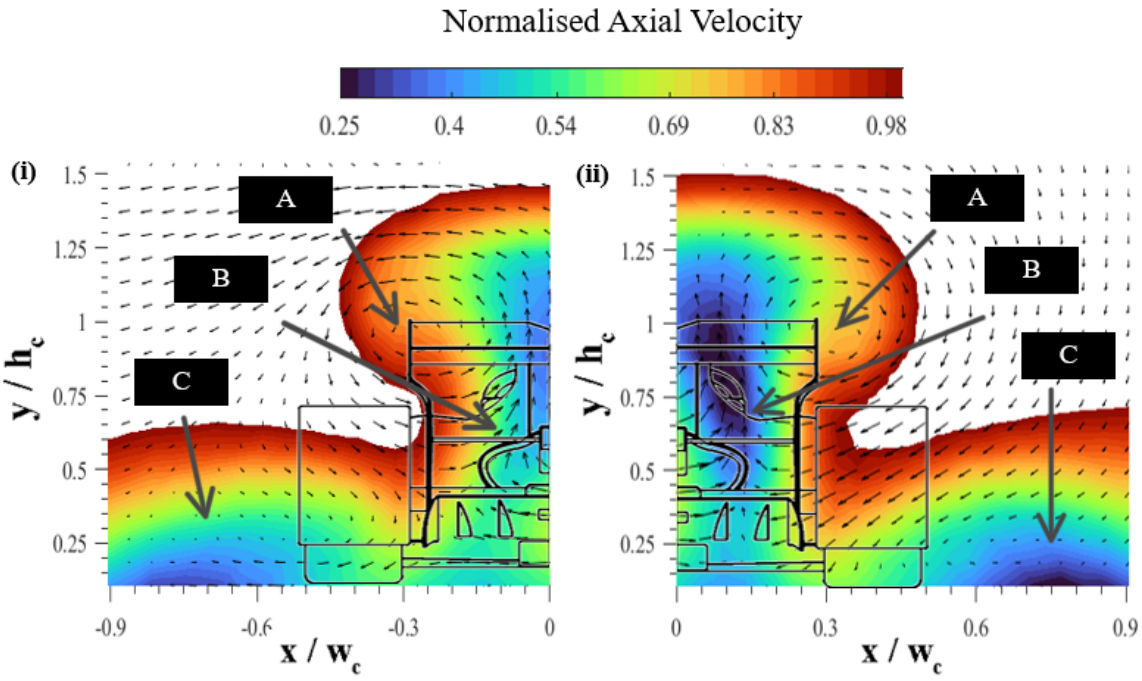


Figure 4.8: Symmetry of scale model normalised axial velocity contours for full wheel fairings at $z = 0.5L$ for wind tunnel tests

These differences were deemed to be minor and had reasonable explanations. The overall structure of the wake was seen to be mostly symmetrical about the centreline of the car, and thus the symmetry assumption was a valid one. Thus, the wind tunnel data yielded sufficient detail for direct comparison with numerical data.

4.4 Wind Tunnel Flow Visualisation

The tuft grid visualisation shown in Figure 4.9(i)-(iii) was for a no fairing configuration at a normalised axial distance $z = 0.5L$. The distinct flow features, as seen by Watts and Watkins in Figure 4.9(iv) [9], were captured during flow visualisation. The vortex to the side of the rear wheel, together with centreline inwash, is labelled *C*. While this vortex was not prominent in Figure 4.9(iv), the comparison of the broader flow field was still relevant. At the centreline, the tufts changed direction and formed a centreline column of upwash (labelled *B*). These tufts changed direction outwards at the rear wing and formed counter-rotating vortices from the rear wing (labelled *A*). These features successfully correlated to the interpreted flow phenomena noted in Figure 4.6 (§4.3).

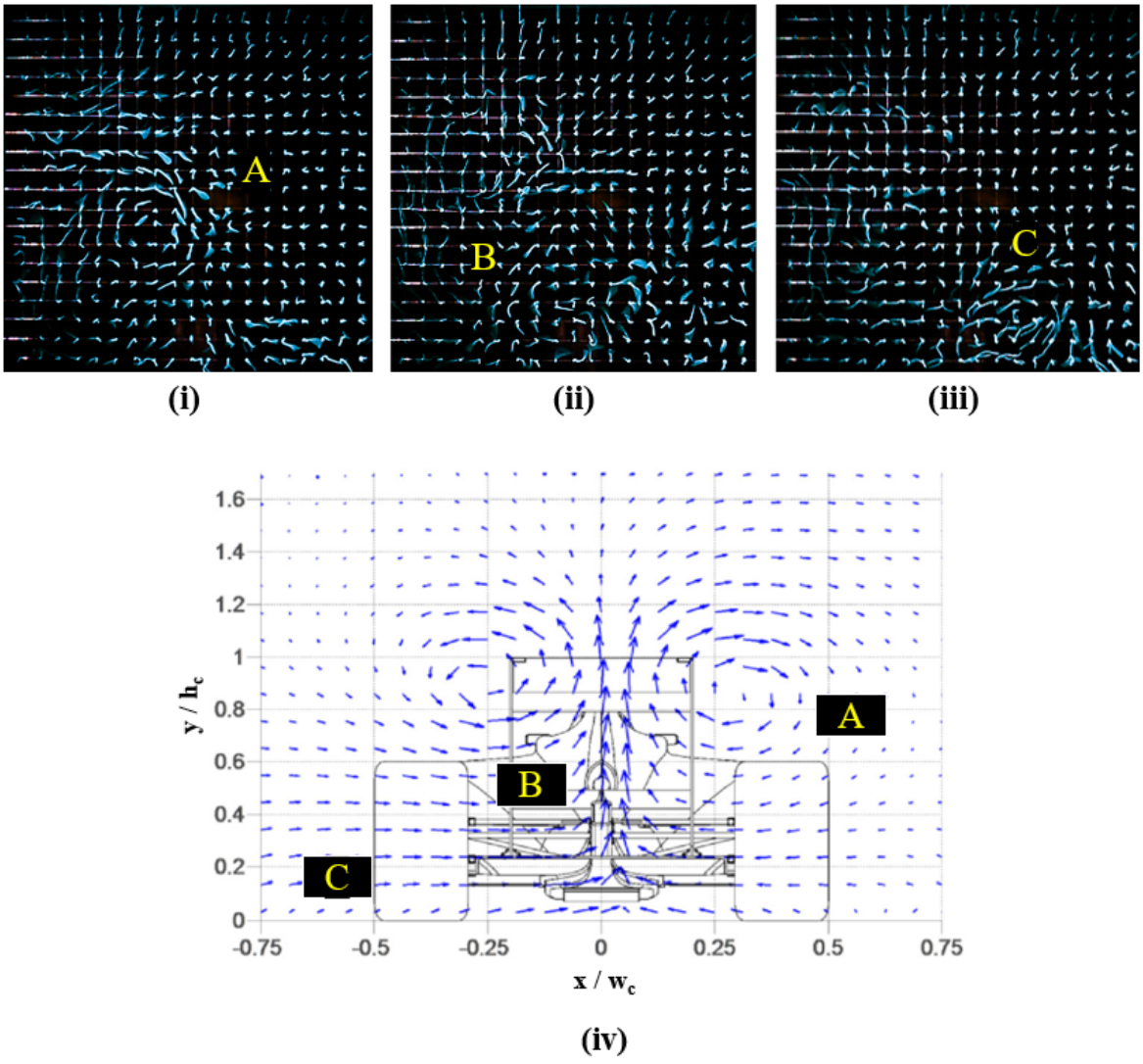


Figure 4.9: Tuft flow visualisation for no wheel fairings at $z = 0.5L$ (i) - (iii) compared to planar velocity components by Watts and Watkins [9] (iv)

The phenomena seen during the tuft grid flow visualisation confirmed that the experimental data was correctly analysed, thus validating the process of utilising a five-hole probe for the wake survey. The structure of the flow field was visually confirmed with the tuft grids and thus the produced colour contours correctly resolved the wake structure.

4.5 Comparison of Numerical and Wind Tunnel Wake Surveys

The purpose of the wind tunnel test was to provide validation to the numerical model. This validation was performed for all three rear wheel configurations. By comparing results for the wind tunnel tests to scale numerical models with the same conditions, the mesh and setup of the model could be deemed valid. Results for an axial distance of $z = 0.5L$ are presented in section 4.5. Results for an axial distance of $z = 1.0L$ can be found in Appendix A. The contours for the numerical and experimental results were created using two separate software packages. Thus the colour maps/scales used for the numerical and experimental contours are not exactly alike, and direct colour comparison cannot be made.

For the no fairing numerical simulation contours in Figure 4.10(i), the vortex from the rear wing (labelled A) had a core at $x = 0.28w_c$ and $y = 0.91h_c$. The low axial velocity column (labelled B), with normalised value of $\sim$0.25, had a normalised height of approximately 0.294. The vortex to the side of the wheel (labelled C) began at a distance of approximately $x = 0.6w_c$, with a normalised axial velocity of $\sim$0.71 at this point. For the no fairing wind tunnel contours in Figure 4.10(ii), the core of the vortex from the rear wing (labelled A) was at a position of $x = 0.32w_c$ and $y = 0.98h_c$. This represented a difference of 13.3% and 7.4% for the normalised x and y coordinates respectively. The low axial velocity column existed (labelled B), with a region of the lowest normalised value ($\sim$0.25) having a normalised height of 0.318. This represented a difference of 7.84% for the height of this low velocity region. While the vortex to the side of wheel (labelled C) began at $x = 0.6w_c$, the normalised axial velocity was considerably lower with a value of $\sim$0.25 at this point, a difference of 95.8%.

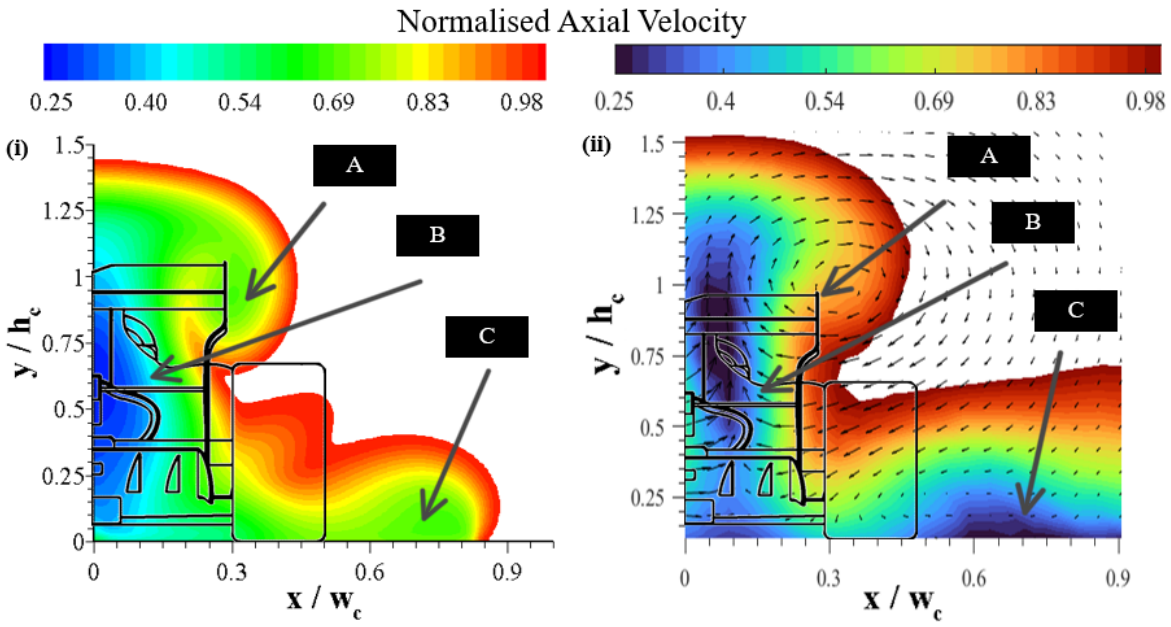


Figure 4.10: Scale model normalised axial velocity contours for no wheel fairings at $z = 0.5L$ for CFD (i) and wind tunnel (ii) tests

For the partial fairing numerical simulation contours seen in Figure 4.11(i), the core of the vortex from the rear wing (labelled A) had coordinates at $x = 0.28w_c$ and $y = 0.90h_c$. The centreline region of low axial velocity (labelled B) of ~0.25 had a normalised height of 0.541. The vortex to the side of the rear wheel (labelled C) began at a normalised distance of approximately $x = 0.6w_c$, with a core normalised velocity of ~0.67. For the partial fairing wind tunnel contours seen in Figure 4.11(ii), the core of the vortex that originated from the rear wing was located at $x = 0.32w_c$ and $y = 0.98h_c$, which correlated to a difference of 13.3% and 8.5% respectively in comparison to the numerical results. The centreline low axial velocity region had a normalised height of 0.476. This represented a percentage difference of 12.8%. The low-velocity core of the vortex to the side of the wheel began at a distance of approximately $x = 0.65w_c$, with a minimum normalised axial velocity of ~0.25. This was a 91.3% difference in comparison to the numerical results.

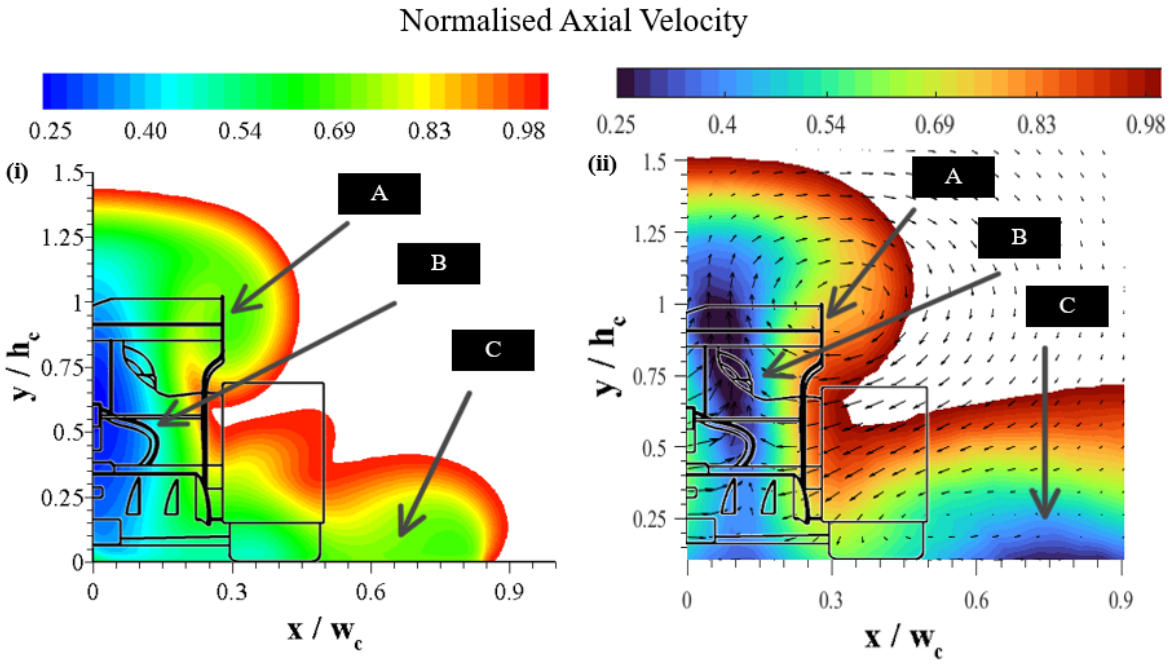


Figure 4.11: Scale model normalised axial velocity contours for partial wheel fairings at $z = 0.5L$ for CFD (i) and wind tunnel (ii) tests

For the full fairing numerical simulation contours seen in Figure 4.12(i), the vortex that originated from the rear wing (labelled A) had a core at $x = 0.3w_c$ and $y = 0.89h_c$. The centreline column of low axial velocity of ~0.29 (labelled B) had a normalised height of approximately 0.279. The lower axial velocity core of the vortex to the side of the wheel had a normalised value of ~0.66 and this vortex started at a normalised distance of approximately $x = 0.6w_c$. For the full fairing wind tunnel contours seen in Figure 4.12(ii), the vortex core from the rear wing (labelled A) was at a position of $x = 0.32w_c$ and $y = 0.98h_c$, a 6.45% and 9.62% difference respectively. The column of low axial velocity (labelled B) at the centreline had a normalised height of 0.317. This was a 12% difference in comparison to the numerical result. The low velocity core to the side of the wheel (labelled C) began at $x = 0.6w_c$ but had a lower normalised core of ~0.25. This correlated to a difference of 90.1%.

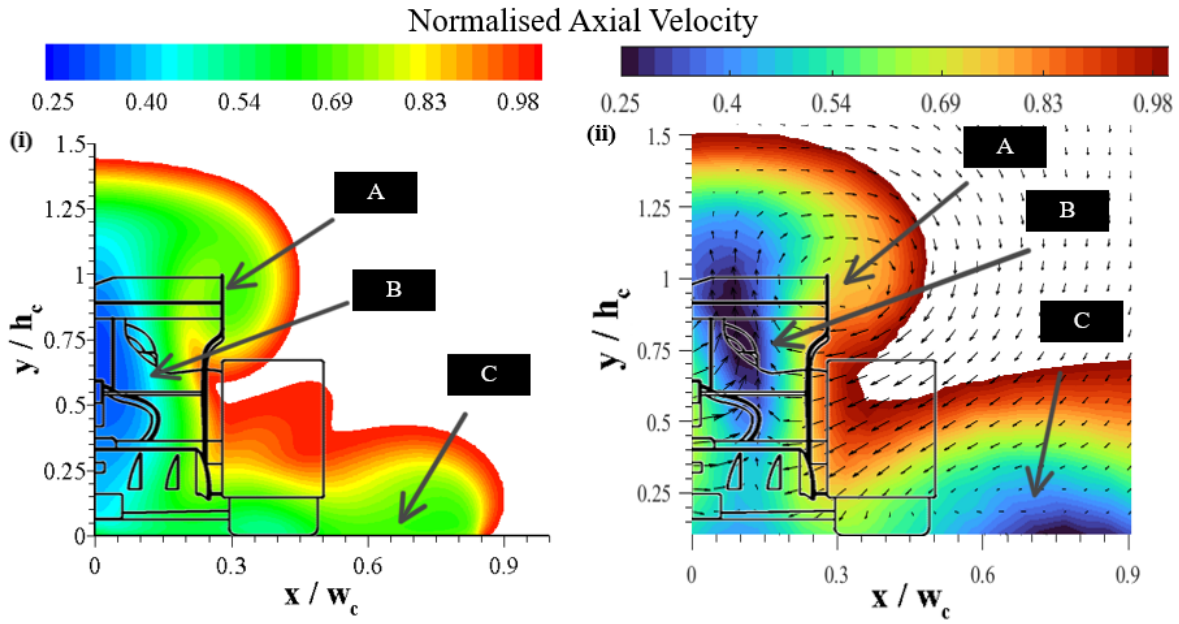


Figure 4.12: Scale model normalised axial velocity contours for full wheel fairings at $z = 0.5L$ for CFD (i) and wind tunnel (ii) tests

For all three fairing configurations, the numerical results were judged to correlate closely with the results of the wind tunnels tests. The prominent flow features that were seen in the numerical simulations were replicated in the wind tunnel, although discernable differences could not be seen easily in the wind tunnel tests. This was because the grid spacing traversed by the probe did not have a high enough resolution to pick up small scale differences. However, the purpose of the wind tunnel tests was to provide validation to the numerical model and not to examine the differences in flow features caused by the different wheel configurations. By replicating the general structure of the wake, the numerical model was assumed to be valid. The percentage differences between the features of the rear wing tip vortices and the centreline column of low axial velocity upwash were considered small and thus within an acceptable level to consider the numerical simulations as an accurate reflection of the experimental conditions. The vortex to the side of the rear wheel for all three configurations was considerably lower for the wind tunnel tests. This was due to the absence of an effective boundary layer removal device for the ground plane. The low-speed air of the ground plane boundary layer was lower than that of the vortex core, thus causing the discrepancy in this region.

The normalised axial velocity along the centreline have been plotted for the numerical and wind tunnel results. These correspond to Figures 4.13, 4.14, and 4.15 for the no fairing, partial fairing and full fairing configurations respectively. For the numerical results, the normalised axial velocity at the ground plane was slightly below 0.6 for all three configurations. This value decreased further up the centreline, reaching a minimum value at approximately $y = 0.6h_c$. The value then increased further up to maximum value close to 1.0 (equal to the free-stream velocity) at $y = 1.4h_c$. The points for the curve of the wind tunnel results exhibited similar behaviour. The minimum normalised axial velocity value for the wind tunnel tests of each configuration was slightly higher up the centreline than that of the numerical result. These values approached the free-stream velocity at the maximum height of the centreline. The considerable difference between the numerical and wind tunnel curves were the values towards the ground plane. The normalised axial velocity was below 0.4 for the wind tunnel test for all configurations. The axial velocity then increased up the centreline to approximately $y = 0.24h_c$. These values then decreased past this point and displayed the same behaviour as the numerical results. This initial increase in axial velocity was attributed to the increasing velocity gradient of the boundary layer of the ground plane. Because a moving ground plane could be implemented in the numerical model, no boundary layer would have formed and thus this effect was not seen here.

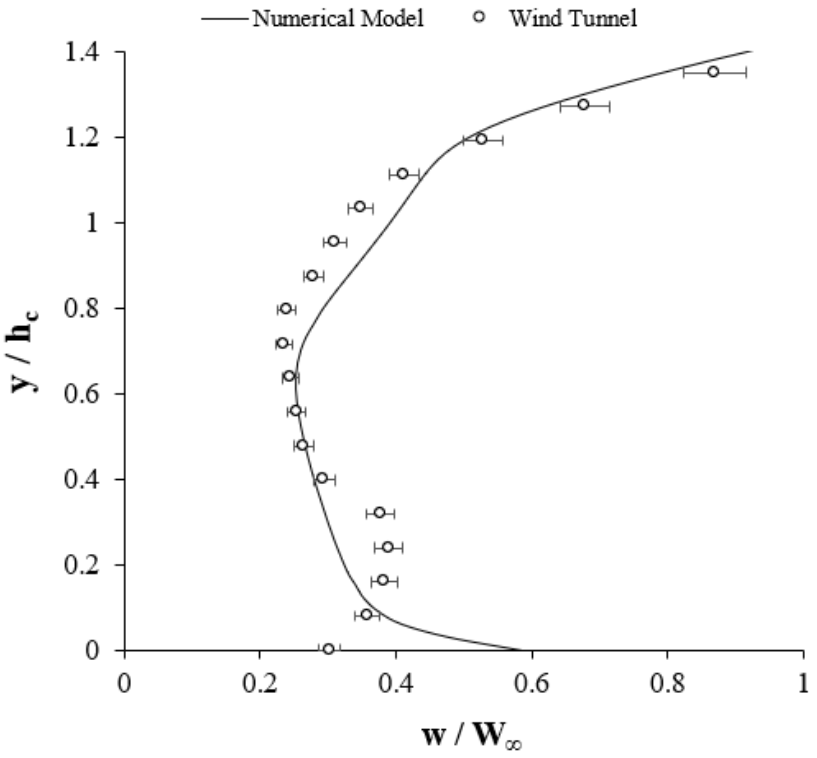


Figure 4.13: Numerical model and wind tunnel test normalised axial velocity distribution along height of car for no wheel fairing configuration

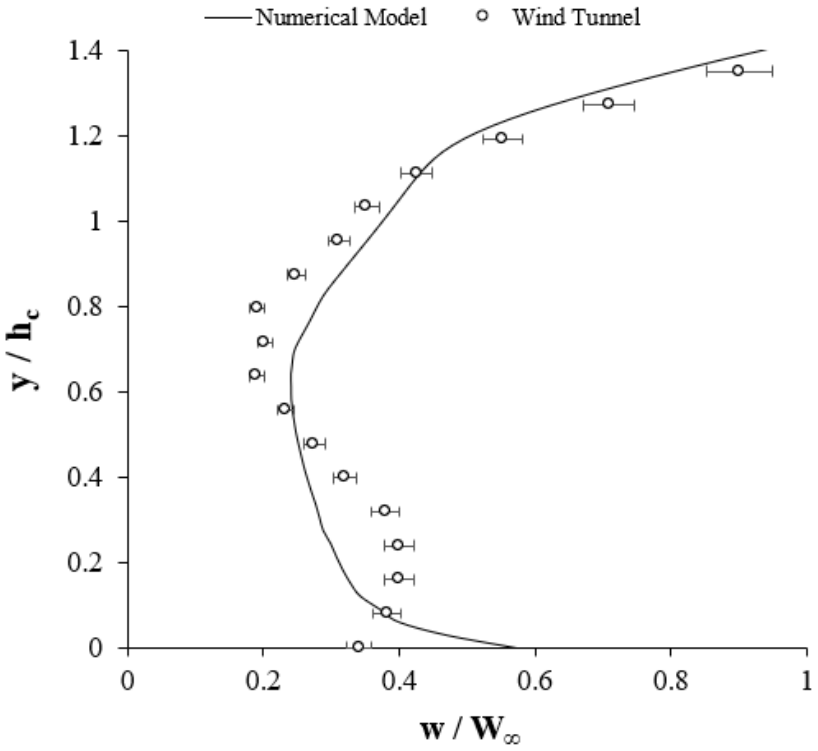


Figure 4.14: Numerical model and wind tunnel test normalised axial velocity distribution along height of car for partial wheel fairing configuration

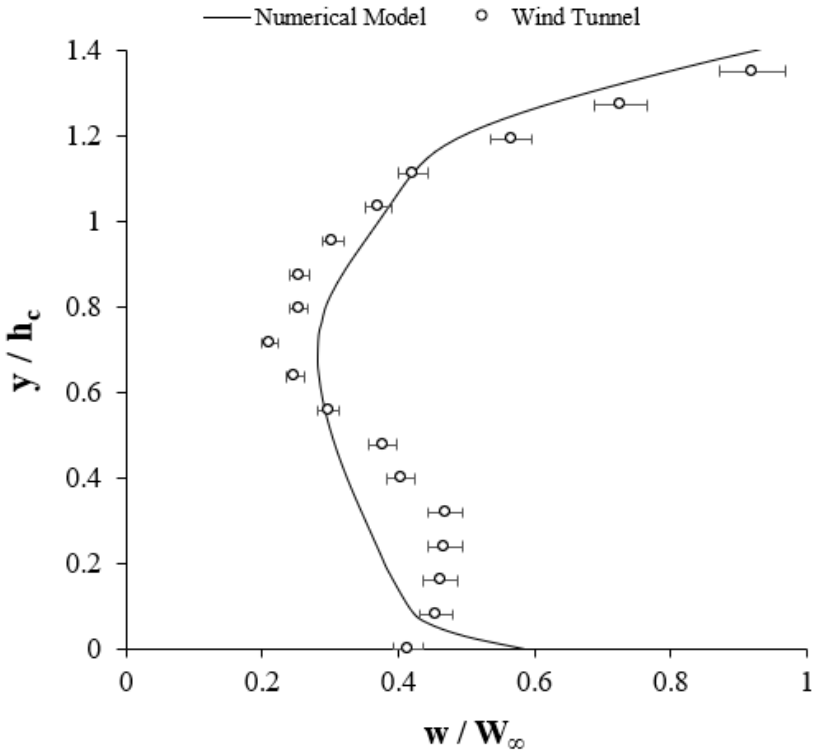


Figure 4.15: Numerical model and wind tunnel test normalised axial velocity distribution along height of car for full wheel fairing configuration

4.5.1 Uncertainty of Wind Tunnel Measurements

The three measurements of interest were the velocity components in the x, y and z directions (u, v and w respectively). The average uncertainties for these quantities (shown in Table 4.5), as calculated by the procedure shown in Appendix B, were considered to be within an acceptable range. The maximum uncertainty among all three quantities was 6.11%, which was sufficiently small to conclude that the measured velocity components displayed reasonable accuracy.

Table 4.5: Average uncertainty associated with measured wind tunnel velocity components

Rear Wheel Configuration	Half-plane (z)	% Uncertainty u	% Uncertainty v	% Uncertainty w
No wheel fairings	$0.5L$	5.60	5.34	5.56
	$1.0L$	6.03	5.16	5.27
Partial wheel fairings	$0.5L$	5.90	5.34	5.72
	$1.0L$	5.78	5.27	5.60
Full wheel fairings	$0.5L$	6.11	5.34	5.87
	$1.0L$	5.87	5.27	5.65

These uncertainty values could be expressed in terms of significant digits. For example, the maximum value for each velocity component for the no wheel fairing configuration at $z = 0.5L$ could be expressed within a range of the associated uncertainty values. In this plane, the maximum velocity component in the x direction was $u = 4.38 \pm 0.25$ m/s (5.60%). The maximum velocity component in the y direction was $v = 5.56 \pm 0.30$ m/s (5.34%). The maximum velocity component in the z direction was $w = 22.2 \pm 1.2$ m/s (5.56%).

4.6 Comparison of Scaled Numerical Models Utilising Stationary and Rotating Wheels

Two sets of the numerical simulations were run - one simulation with non-rotating (stationary) wheels (fully representative of the wind tunnel tests), and one simulation with rotating wheels. This was done in order to ascertain the difference in results caused by the effects of the rotating wheels. The differences are highlighted in the contours and streamtraces for the no wheel fairing configuration at the plane of normalised distance of $z = 0.0L$. Not all configurations are presented in section 4.6 as the purpose was only to highlight the presence of differences in the wake behind the car due to the rotation of the wheels.

For the no-fairing configuration with non-rotating wheels in Figure 4.16, there was seen to be an area of lower normalised axial velocity of ~ 0.73 to the outside of the rear wheels (labelled A). This lower-velocity region extended from the wheel to a normalised distance of $x = 0.86w_c$ from the centreline of the car. At a normalised height of $y = 0.5h_c$ (labelled B), the normalised axial velocity was ~ 0.48. This region is immediately aft of the rear wheels and was therefore part of the low-velocity wake of the wheel. There is a region of very low axial velocity (between 0.04 and ~0.18) at the rear wing of the vehicle (labelled C). However, at the tips of the rear wing, it was seen that the axial velocity begins to increase as the low-velocity air from the upper surface of the wing spilled over to the underside of the wing. This was the region in which the counter-rotating vortices began to develop. At the exit of the diffuser (labelled D), there existed a region of low axial velocity attributable to the high-speed airflow from underneath the car that expanded after exiting the diffuser [55].

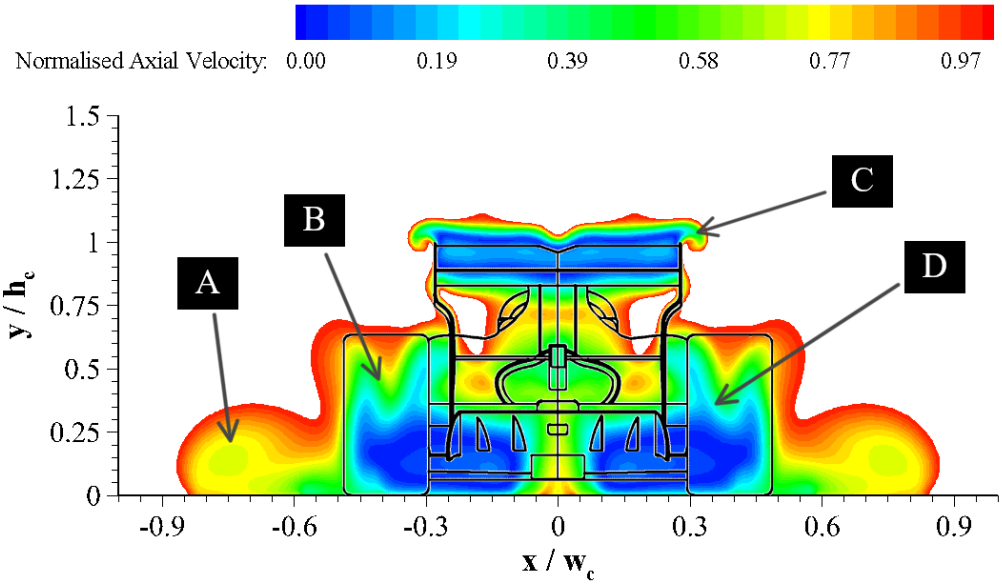


Figure 4.16: Scale model normalised axial velocity contours for no wheel fairings at $z = 0.0L$ for non-rotating wheels

For the no-fairing configuration with rotating wheels in Figure 4.17, the low-velocity region to the side of the rear wheels (labelled A) had moved slightly inwards, extending to a normalised distance of $x = 0.8w_c$ from the centreline of the car. The normalised axial velocity has remained at a value of ~ 0.73. In the wake region behind the wheel (labelled B), at $y = 0.5h_c$, the axial velocity had reduced considerably, to as low as a normalised value of 0.02. This is because the rotation of the wheels resulted in an earlier separation point along the circumference of the wheel. The regions around the rear wing (labelled C) and the exit of the diffuser (labelled D) was unaffected by the rotation of the wheels.

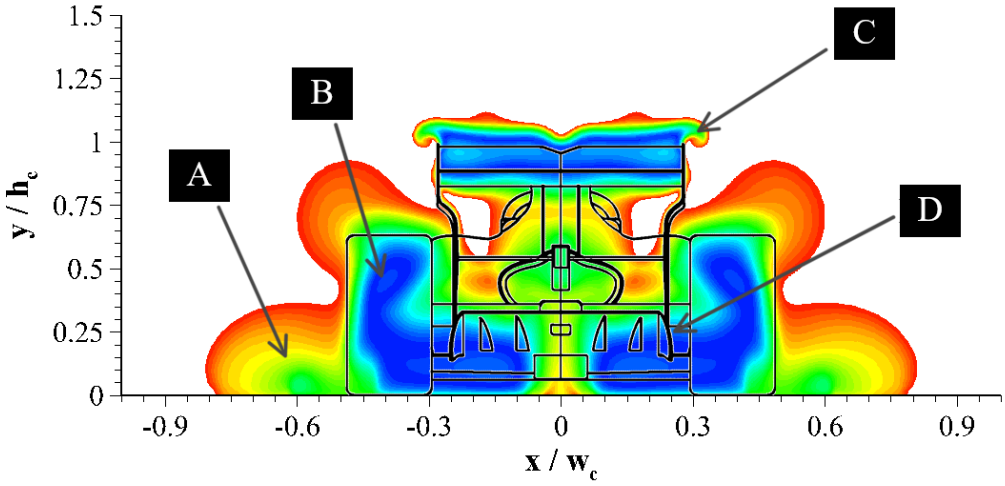


Figure 4.17: Scale model normalised axial velocity contours for no wheel fairings at $z = 0.0L$ rotating wheels

For the no-fairing configuration with non-rotating wheels in Figure 4.18, a vortex was seen to the side of the rear wheel (labelled A), with a centre at normalised coordinates of $x = 0.15w_c$ and $y = 0.725h_c$. This vortex combined with two vortices aft of the rear wheel in the highly turbulent wake (labelled B and E). The centre of the vortex labelled B is present at normalised coordinates of $x = 0.33w_c$ and $y = 0.2h_c$. The centre of the vortex labelled E is present at normalised coordinates of $x = 0.45w_c$ and $y = 0.34h_c$. There existed a column of centreline upwash (labelled C) originating from the ground plane. Counter-rotating vortices were seen to start originating from the tips of the rear wing (labelled D). The downwards component of these vortices combined with the vortex labelled E, along with inwash, increasing the intensity of the turbulent wake of the wheel.

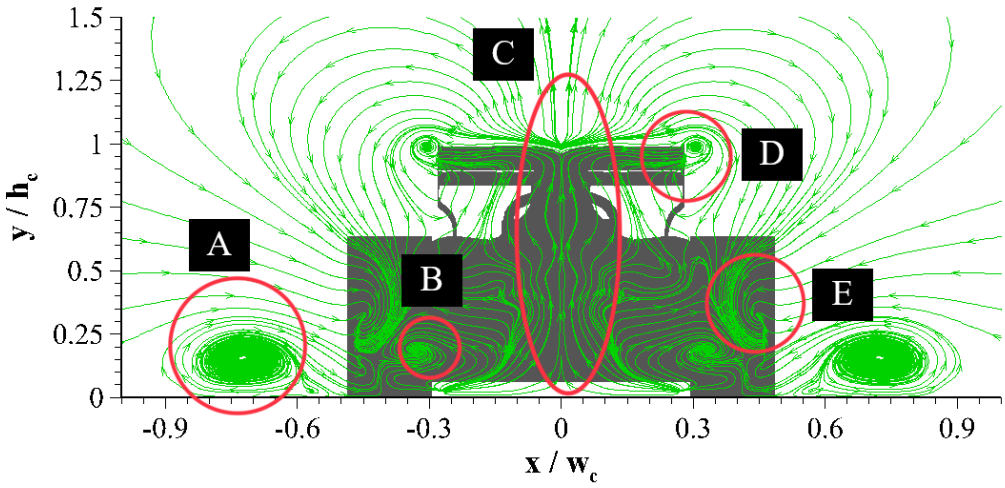


Figure 4.18: Scale model planar streamtraces for no wheel fairings at $z = 0.0L$ for non-rotating wheels

For the no-fairing configuration with rotating wheels in Figure 4.19, there existed two separate vortices to the sides of the rear wheel (labelled A). The vortex centres were at $x = 0.69w_c$, $y = 0.13h_c$ and $x = 0.57w_c$, $y = 0.05h_c$. The formation of two separate vortices was due to the higher levels of turbulence caused by the rotation of the wheel, causing an additional transfer of energy. These two vortices interacted with the vortices labelled B and E. The vortex labelled by B moved outwards to a value of $x = 0.46w_c$, with the vortex labelled by E having moved inwards to a value of $x = 0.39w_c$ and upwards to a value of $y = 0.49h_c$. The centreline column of upwash (labelled C) and the counter-rotating vortices (labelled D) remained unchanged by the rotation of the wheels. A noticeable change from the rotation of the wheels was the presence of a small vortex (labelled by F) at $x = 0.14w_c$ and $y = 0.46h_c$.

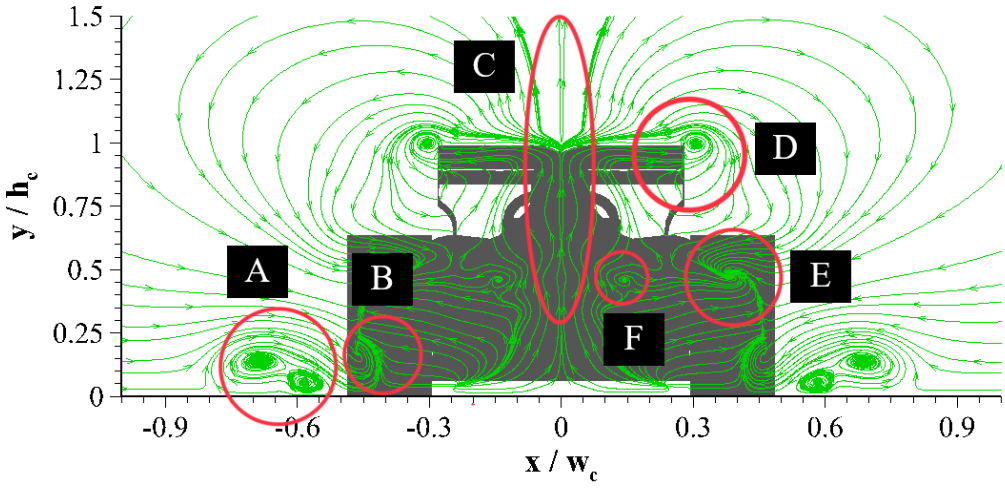


Figure 4.19: Scale model planar streamtraces for no wheel fairings at $z = 0.0L$ for rotating wheels

The rotation of the wheels thus altered the structure of the wake behind the vehicle for each fairing concept. The main difference seen is that the structure of the vortices changed due to the rotation of the wheels. The rotation of the wheels caused the vortices to the sides of the rear wheels to reduce in axial velocity, as well as having moved this vortex core inwards. The locations of the vortices aft of the wheels also moved due to this rotation. The flow at the rear wing and centreline remained unchanged. These differences highlighted the importance of the implementation of rotating wheels for numerical simulations. Results obtained from stationary-wheel simulations thus did not serve as a true replication of the flow structure of an operational full size car. These were used purely to validate the quality of the mesh and the numerical setup by having compared these results to those obtained from the wind tunnel tests.

4.7 Summary of Validation and Verification

The numerical model was verified by mesh independence studies as well as by testing the sensitivity of the solution to the domain size. The finer mesh for all three configurations (approximately 27 million cells each) was found to be the minimum level of refinement required for mesh independence. The effect of domain size on the drag and lift coefficients of each car was found to differ insignificantly and thus it was concluded that the domain was appropriately sized. The wall $y+$ values were within the desired log-law region of the turbulent boundary layer (i.e. $y+$ above 30). Values outside of this region were seen at separation points. However, this was acceptable as per the STAR-CCM+ User Guide [47]. Furthermore, the wake structure found for the no wheel fairing configuration was validated by the qualitative similarities to a previous study by Newbon et al. [10].

The wind tunnel wake survey was validated and the 'mushroom-like' wake structure previously seen by Watts and Watkins [9] was observed through five-hole probe tests and tuft grid flow visualisation. The three-dimensional velocity components (u, v, and w) of the wind tunnel were associated with adequately low uncertainty values. The calibration procedure outlined by Town and Camci [62] was closely followed and resulted in the expected calibration plots (Figure 4.5). The data from the wind tunnel wake surveys was compared to scale numerical models and satisfactory agreement existed between results for all three car configurations. Thus the numerical setup was deemed valid for full size car simulations with rotating wheels. Reynold's number independence was not achieved between the scale wind tunnel and full size numerical wake surveys. Though Reynolds number independence was not achieved, the scale wind tunnel data could still be adequately used to validate a particular numerical model setup. This setup could then be implemented at speeds more applicable to high speed automotive aerodynamics.

Chapter 5

Results and Discussion

5.1 Wake Survey of Full Size Numerical Results

These results are representative of the three rear wheel configurations, namely no wheel fairings, partial wheel fairings, and full wheel fairings. These results are presented for three different planes aft of the vehicle and the midplane of the car and the rear wheel (§3.2). All coordinates have been normalised by the characteristic dimensions of the car. The axial velocity (w) components in the z direction have been normalised by the freestream velocity. The upwash/downwash velocity components (v) were not normalised as the freestream air velocity did not have a velocity component in the y direction. Normalising these components would have resulted in division by zero. All percentage changes are between the no wheel fairing configuration and a corresponding fairing (partial or full) configuration unless otherwise stated.

5.1.1 Wake Immediately Aft of Car ($z = 0.0L$)

Figures 5.1, 5.2, and 5.3 show the normalised axial velocity colour flooded plots (contours) in a plane immediately aft of the car for no wheel fairings (NWF), partial wheel fairings (PWF), and full wheel fairings (FWF) respectively. The most obvious difference between these three configurations was the low-speed flow (normalised velocity of ∼0.2) immediately aft of the rear wheel (labelled A). The maximum height of this region was highest for the no wheel configuration, with a value of $y = 0.53h_c$. The addition of partial wheel fairings reduced this height by 103% to a value of $y = 0.17h_c$. The addition of full wheel fairings reduced this height by 143% to a value of $y = 0.089h_c$. There existed a separation point aft of the wheel. This separation point has been found to exist further upstream for a rotating wheel.

This earlier separation resulted in a larger region of low dynamic pressure aft of the wheel in comparison to the configurations with fairings. The flow over the cylindrical surface of the fairings behaved in the same way as flow over a stationary wheel, with a later separation point. Any separated flow from the rotating wheels was forced to flow along an enclosed path created by the fairing. The low velocity region close to the ground plane correlated with this flow expanding upon exiting the enclosed fairing space, causing a reduction in normalised velocity. A larger low-speed wheel wake here would result in a larger low-speed region in this same planar position further downstream. This is because the low-speed air flow would be associated with a more significant momentum loss, resulting in a more disturbed wake aft of the wheels. However, it is possible that the wheel fairings would only delay this loss of momentum further downstream rather than causing a reduction or elimination of this disturbed region.

At the tips of the rear wing, vortices began to form. This corresponded to a normalised axial velocity of 0.41 at this point (labelled B). The position and normalised velocity of this vortex core remained constant between the three different rear wheel configurations which indicated no effect on the axial component of this flow structure by the addition of fairings. These vortices began to form due to the interaction of the flow from the top and bottom surfaces of the rear wing, which generated downforce. However, this was not indicative of no change after the addition of wheel fairings. This is because vortex strength is directly proportional to the downforce produced by the rear wing and thus only affected the planar velocity components, and the velocity component w in the z axis was unaltered. This component is instead dominated by the shape of the car.

For all the rear wheel configurations, a low velocity region (normalised value of $\sim$0.8) at the height of the rear wing (and over the entire width) existed (labelled C). This low speed airflow originated from the upper surface of the rear wing and this region was unaltered by the addition of any wheel fairings. This low axial velocity was attributed to the upwash generated by the wing as downforce was produced. By deflecting the airflow upwards, the rear wing reduced the velocity component in the z direction while simultaneously increasing the velocity components in the x and y directions.

A low-velocity (normalised value of $\sim$0.0) region existed at the exit of the diffuser of the car for all three configurations (labelled D). The height of this low-velocity region differed slightly between the three configurations. With no wheel fairings, the height of this region was approximately equal to $y = 0.264h_c$. The addition of partial wheel fairings increased the height of this region by 11% to a value of $y = 0.293h_c$. The addition of full wheel fairings increased the height of this region by 13.3% to a value of $y = 0.299h_c$ [55]. The width of this region was constant between the three configurations with a value of approximately $x = 0.4w_c$. This low-speed airflow was caused by the expansion of air at the diffuser. This region

is of particular importance to a trailing car as the front wing will encounter this low-speed flow when operating in the slipstream of a leading car. An increase in size of this region would decrease the ground effect experienced by a trailing car due to low velocity air flowing over the underside of the trailing car. This reduces the pressure differential between the top surface and underside of the car, thereby reducing downforce towards the ground (§2.1). The drag force experienced by a trailing car would decrease with an increase in size of this low velocity region.

A region of low axial velocity airflow was also present to the sides of the rear wheels (labelled *E*). At the centre of this region, the normalised axial velocity was ∼0.49. The addition of partial wheel fairings reduced this value by 4.17% to a value of 0.47. The addition of full wheel fairings reduced this value by 13% to value of 0.43. The rotation of the wheels enables an additional transfer of energy thereby reducing the size of the low-speed region. With the wheels covered this energy transfer was hindered, thus not allowing for the transfer of kinetic energy here. This resulted in a lower axial speed vortex core. Partial fairings still allowed for the transfer of energy from the rotating side wall of the wheels which resulted in a higher axial velocity in comparison to the full wheel fairings. A trailing car attempting an overtake would need to move through this region of low velocity air. If the overtaking manoeuvre is being attempted in a corner, a reduction of downforce and on the front wing would be caused by the addition of wheel fairings, with full wheel fairings causing the most significant reduction, leading to understeer in corners.

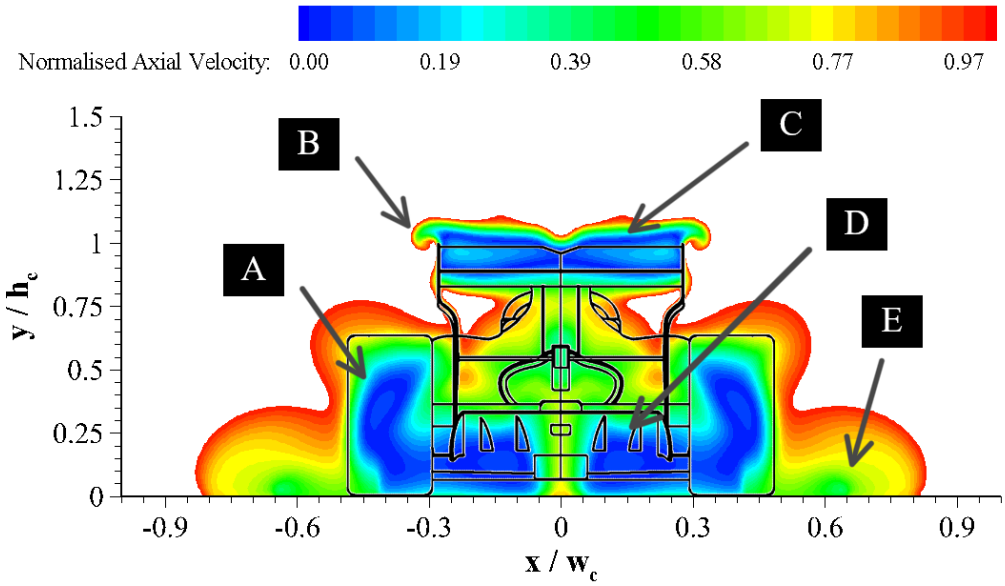


Figure 5.1: Full size normalised axial velocity contours for no wheel fairings at $z = 0.0L$

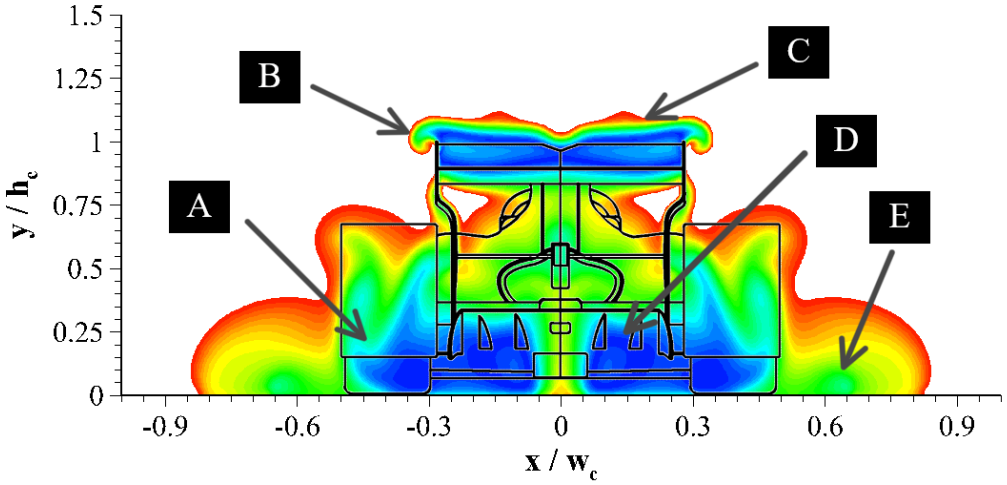


Figure 5.2: Full size normalised axial velocity contours for partial wheel fairings at $z = 0.0L$

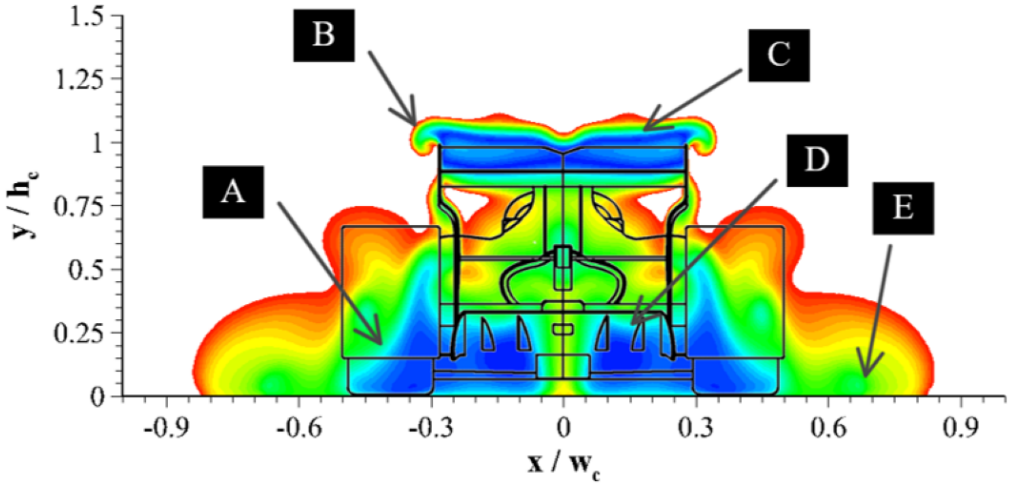


Figure 5.3: Full size normalised axial velocity contours for full wheel fairings at $z = 0.0L$

Two-dimensional planar streamtraces are shown in Figures 5.4, 5.5, and 5.6. These streamtraces are representative of the velocity components u and v, in the x and y directions respectively. The core of the rear wing tip vortex (labelled A) was seen to be at coordinates of $x = 0.31w_c$ and $y = 0.998h_c$ for all three configurations. The circulation of these vortices was seen to be opposite on either side of the rear wing (i.e. counter-rotating). This was consistent with a lifting surface generating downforce as the airflow at different speeds from the top and bottom surface of the wing interacted upon leaving the trailing edge.

A centreline column of upwash (labelled B) was present for all configurations. This originated upwards from the ground plane for the entire height of the car and was the net induced effect of the vortices on the wake flow structure. The upwards component of airflow exiting the diffuser of the car contributed significantly to this upwash. Upwash is undesirable for both the leading and trailing cars. This is because upwash changes the effective angle of attack of

a wing. For a leading car, this results in downforce not acting purely towards the ground, but rather with an angle backwards, thereby causing a force component opposing forward motion (or lift induced drag). For a leading car encountering upwash, the reduction of the effective angle of attack results in less downforce generation by the wings at the same orientation in comparison to purely horizontal incoming flow. However, a reduced effective oncoming angle of attack can reduce drag for a trailing car thereby enhancing slipstream effects.

The most significant differences in flow structure between the three configurations were seen in the region aft and to the side of the rear wheels (labelled C). For the no fairing configuration, the circulation and intensity of the vortices was lower in comparison to those present for partial wheel fairings. These vortices interacted with the wing tip vortices. The addition of wheel fairings causes an expansion of air at the exit of the fairings which enhanced the wheel disturbance and downwash component in this region. Partial wheel fairings caused this region of high circulation to be most prominent due to the interaction of the airflow escaping from the sidewalls of the wheel. The core of the vortex to the side of the rear wheel was at the same height for all three configurations. The width of this core from the car centreline decreased with the addition of wheel fairings. For the no wheel fairing configuration, this core was at a position of $x = 0.68w_c$. The addition of partial wheel fairings moved this core inwards by 7.5% to $x = 0.63w_c$. The addition of full wheel fairings moved this core inwards by 11.3% to $x = 0.60w_c$. Any trailing car attempting an overtake would be required to move through the vortices to the sides of the rear wheel. Thus any reduction in turbulence intensity and flow direction here could be advantageous for downforce generation. Strong upwash (labelled B) still remained with an increase in width away from these cores for all configurations. This would change the effective angle of attack of the front wing of a trailing car leading to a reduction of downforce.

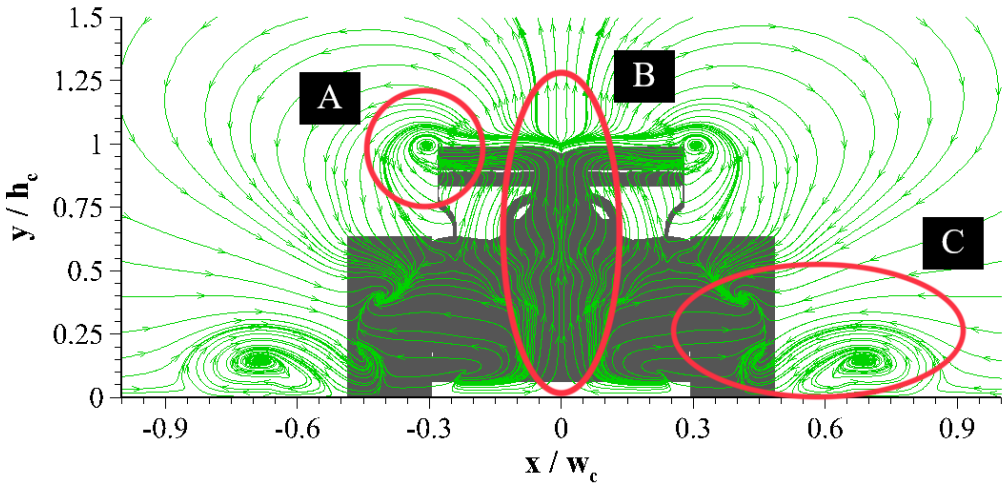


Figure 5.4: Full size planar streamtraces for no wheel fairings at $z = 0.0L$

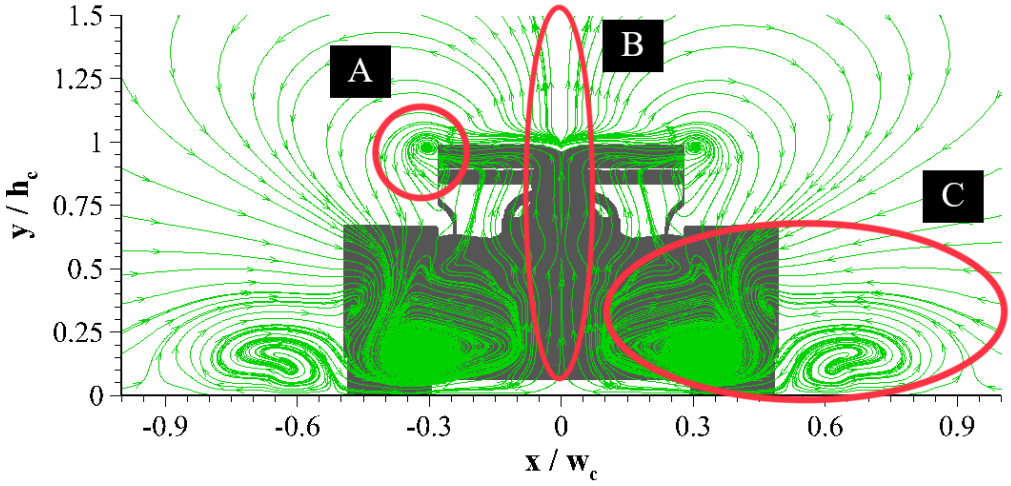


Figure 5.5: Full size planar streamtraces for partial wheel fairings at $z = 0.0L$

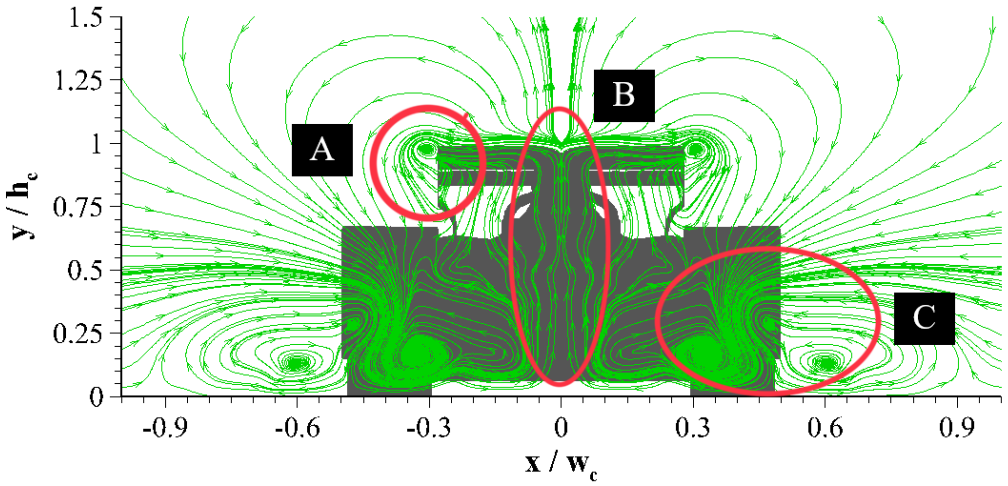


Figure 5.6: Full size planar streamtraces for full wheel fairings at $z = 0.0L$

As can be seen in Figure 5.7(i), the normalised axial velocity along the centreline of the car fluctuated with an increase in height from the ground plane. The same distribution and values of the normalised velocity was seen for all three rear wheel configurations. A maximum normalised axial velocity of approximately 1.10 was present at a height of $y = 1.07h_c$. This corresponded to immediately above the rear wing of the car which was indicative of a return to freestream conditions. This implied that the height of the wake did not extend considerably higher than the the height of the car immediately downstream. A minimum normalised axial velocity of approximately 0.035 was present at a height of $y = 0.92h_c$, the height of the rear wing. This correlated to normalised axial velocity distribution seen in the colour-flooded plots (§5.1.1).

The upwash velocity component along the car centreline (Figure 5.7(ii)) also displayed a fluctuating distribution with no discernable differences between the three rear wheel configurations. This suggested that immediately aft of the car, the main source of the upwash was the rear wing and the associated vortices, and the flow features at the wheels did not contribute significantly to the upwash component here. A maximum value of 19.2 m/s existed at a height of $y = 0.77h_c$ and a minimum value of 0.05 at the ground plane ($y = 0.0h_c$).

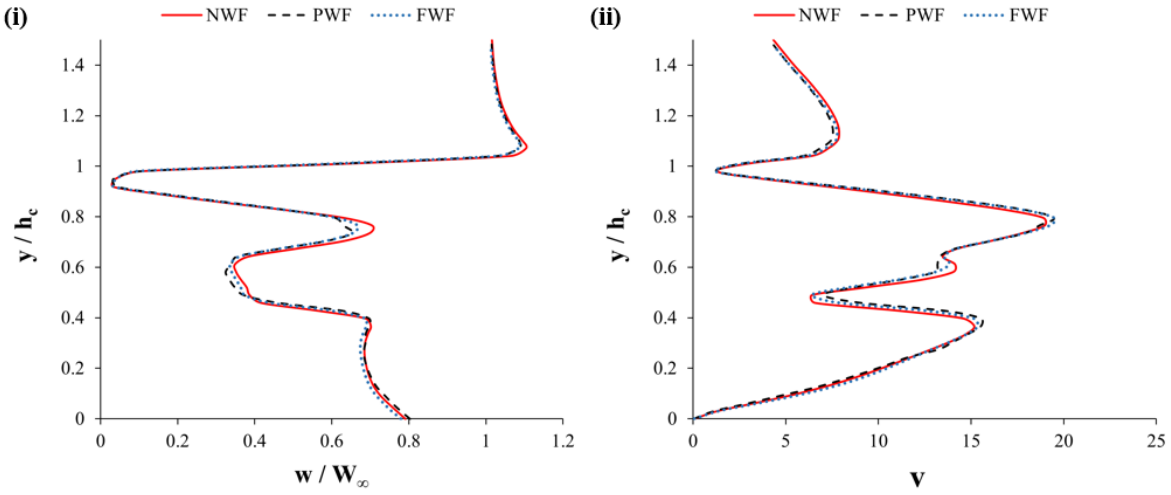


Figure 5.7: Normalised axial velocity (i) and upwash/downwash component (ii) at centreline of car in $z = 0.0L$ plane

At the wheel centreline (Figure 5.8(i)), the addition of wheel fairings (both partial and full) caused an increase in normalised axial velocity low down in comparison to a car with no wheel fairing. This was due to the separated flow along the rotating wheels being streamlined towards the exit of the fairing lower down along the trailing side of the wheel tread. A low axial velocity wake was prevented from forming by the fairings. At a height of ($y = 0.15h_c$) for the no wheel fairings configuration, the normalised axial velocity was at a minimum value of 0.0. This value then fluctuated up until a height of approximately ($y = 0.43h_c$), the approximate height of the separation point along the wheel tread, before increasing to a constant value of 1.02 (i.e. the freestream velocity and the maximum height of the wheel wake) at a height of ($y = 0.83h_c$). A minimum normalised axial velocity of 0.043 existed at a height of ($y = 0.053h_c$) for the partial wheel fairing configuration. This position was 64.7% lower than the height of the minimum axial velocity for no wheel fairings. A minimum normalised axial velocity of 0.065 existed at a height of ($y = 0.031h_c$) for the full wheel fairing configuration. This correlated to a 79.3% decrease in height position from the no fairing configuration. Thus the fairings reduced the height of the wheel wake. After these minimum values, the normalised axial velocity increased with height from the ground plane reaching a maximum of 1.02 at ($y = 0.8h_c$).

In Figure 5.8(ii), an upwash component at the wheel centreline of 2.54 existed at a height of $y = 0.09h_c$ for the no wheel fairing configuration. As the height above the ground plane increased, the direction of this component changed to a downwash one with a maximum magnitude of 8.72 m/s at a height of $y = 0.98h_c$, before increasing to a value of 0 m/s towards the freestream. As seen in the streamtraces in Figure 5.4, two separate vortices formed aft of the wheel and the fluctuating vertical component correlated to the circulation zones of these vortices. No upwash components existed for the partial and full fairing configurations, with only downwash being present. This was the downwash component of the circulation of the vortices here (seen in Figures 5.5 and 5.6). Air exiting the bottom of the fairings was at a lower speed than that exiting the adjacent diffuser. This lead to vortex formation. For the partial fairing configuration, the maximum downwash component magnitude was equal to approximately 26.7 m/s, with the maximum magnitude being approximately 31.8 m/s for the full fairing configuration. This represented a difference of 17.4% between the partial and full fairing configurations. These maximum downwash magnitudes were present at heights of $y = 0.4h_c$ and $y = 0.34h_c$ for the partial and full fairing configurations respectively, a difference of 16.2%.

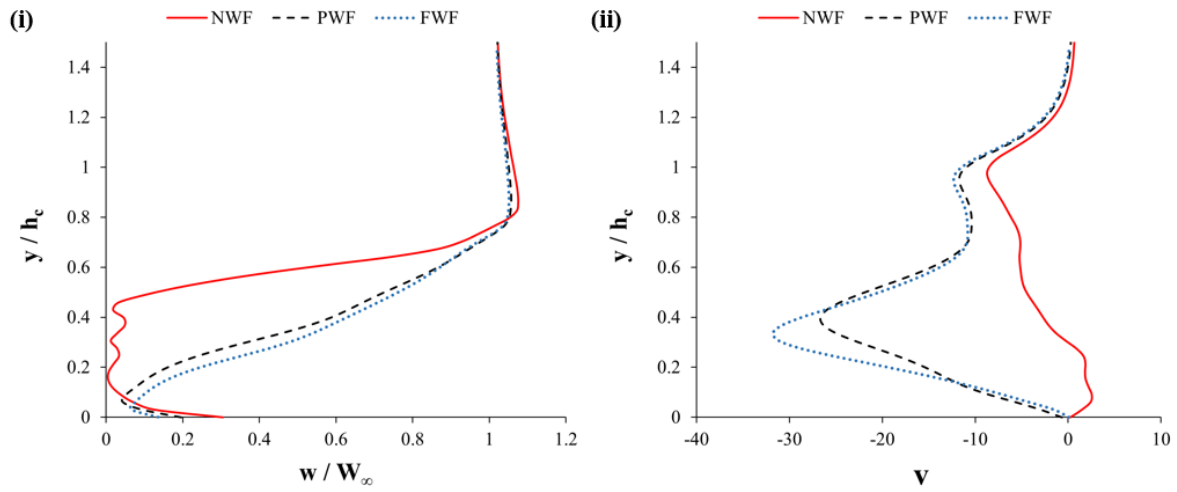


Figure 5.8: Normalised axial velocity (i) and upwash/downwash component (ii) at centreline of wheel in $z = 0.0L$ plane

5.1.2 Wake at Aft Distance of Half a Car Length ($z = 0.5L$)

At half a car length aft of the car, the previously observed 'mushroom-like' wake structure was seen and is shown in Figures 5.9, 5.10, and 5.11. The low velocity core of the vortex (labelled A) to the side of the wheel was seen to have grown in width for all three configurations. This was due to the growth of the vortex circulation region downstream. This increased the planar velocity components while decreasing the axial velocity component. The normalised

axial velocity at this core had the highest magnitude of 0.62. For the partial wheel fairing configuration, this value decreased by 4.83% to 0.59. For the partial wheel fairing configuration, this value decreased by 11.3% to the lowest value of 0.55.

The low axial speed core of the counter-rotating vortices at the rear wing tips (labelled B) had grown in diameter in comparison to the plane immediately aft of the car. The size of these vortices, along with the normalised magnitude of approximately 0.69, remained constant between the three configurations. This magnitude increased as the vortices dissipated further downstream from the car, returning to a value closer to the freestream velocity. The growth of the vortex core was attributed to the increased circulation here similarly to the vortices to the sides of the rear wheel.

A centreline column of low axial velocity (labelled C) airflow (normalised value of $\sim$0.25) formed at a distance of half a car length behind the car. This column was widest for the no wheel configuration, having extended by a normalised distance of $x = 0.17w_c$ from the car midplane. For the partial fairing configuration, the distance from the midplane was reduced by 25.9% to $x = 0.126w_c$. For the full fairing configuration, the distance from the midplane was reduced by 31.2% to $x = 0.117w_c$. The height of this column was also affected. The lowest point of this column was raised with the addition of wheel fairings. With no wheel fairings, this column extended from the ground plane to a height of $y = 1.06h_c$. With partial fairings added, this column extended from the ground plane to a height of $y = 1.11h_c$, an increase in height of 4.63%. The addition of wheel fairings raised the lowest point of this low velocity column upwards to a normalised distance of $y = 0.23h_c$, with a maximum height at $y = 1.12h_c$, an increase of 5.86%. This decrease in size of the low velocity column was attributed to the limited interaction created by the fairings of low speed flow from the wake of the rear wheels and the airflow that exited the diffuser. Without wheel fairings, the centreline region was more disturbed by the rotation of the wheels. Covering the wheels thereby limited the disturbance at the centreline by enclosing the highly turbulent and erratic flow surrounding the rotating wheels. This allowed for a greater axial velocity component.

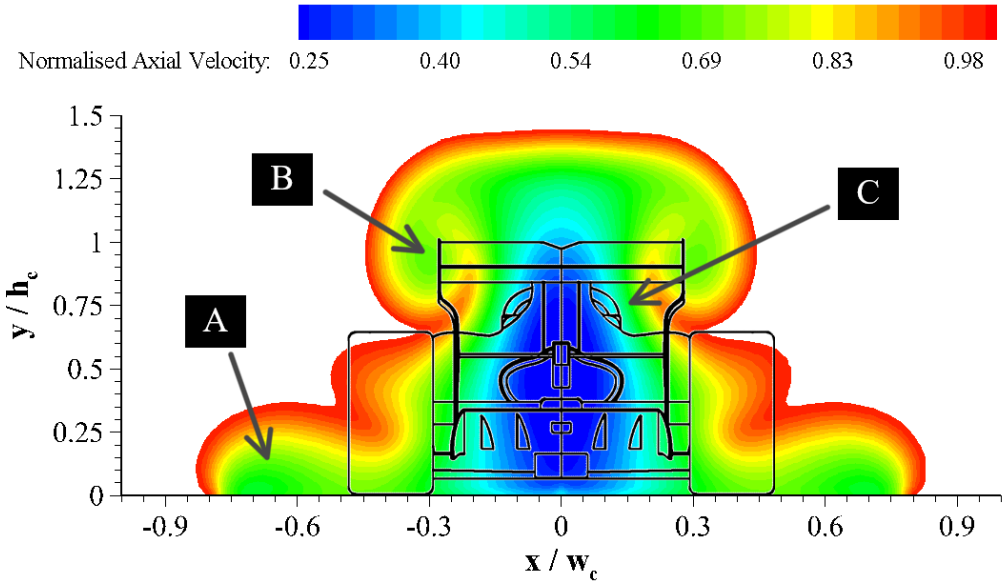


Figure 5.9: Full size normalised axial velocity contours for no wheel fairings at $z = 0.5L$

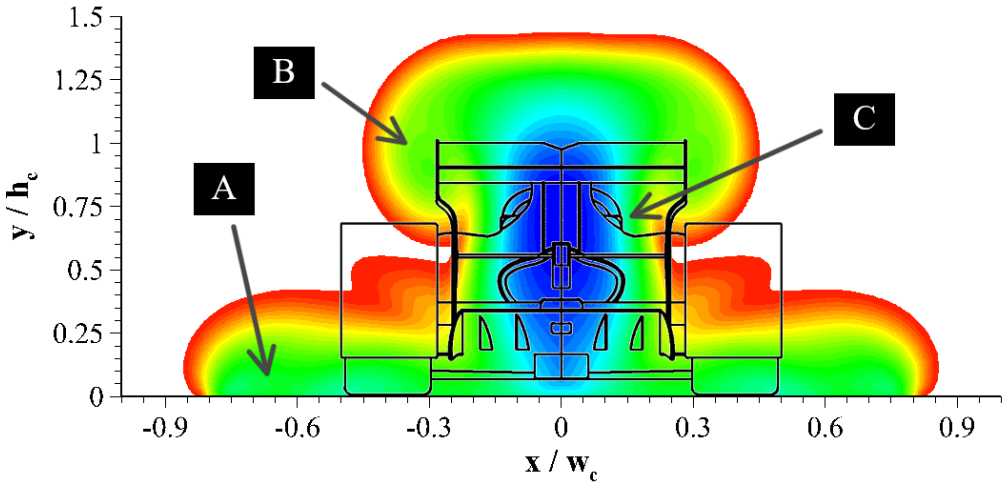


Figure 5.10: Full size normalised axial velocity contours for partial wheel fairings at $z = 0.5L$

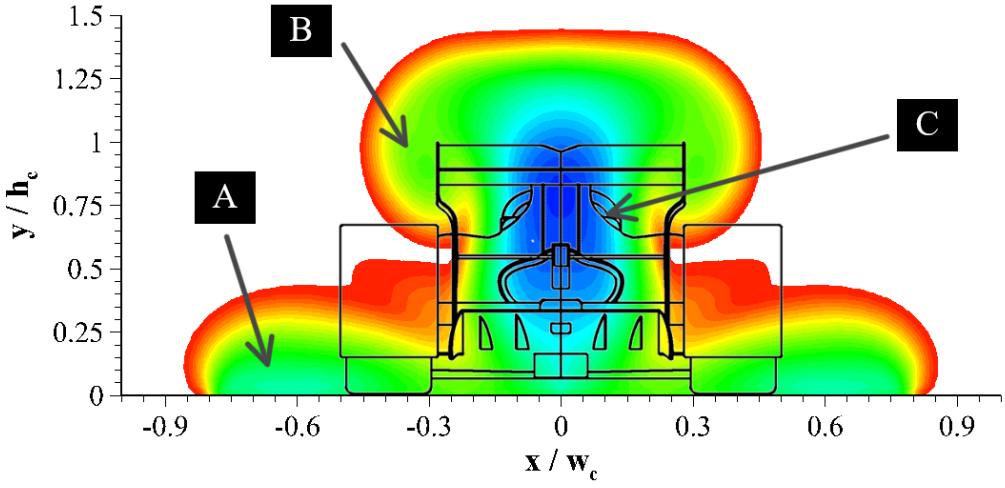


Figure 5.11: Full size normalised axial velocity contours for full wheel fairings at $z = 0.5L$

The streamtraces of the velocity components u and v in Figures 5.12, 5.13, and 5.14 show that the vortices grew in diameter at the rear wing tips (labelled A) which caused increased circulation here, with the highest vorticity seen for the no wheel fairing configuration. The downwash component of these counter-rotating vortices was seen to develop into inwash that moved towards the centreline of the car. Along the axial direction z, the upwash produced by the rear wing enhanced the vortex circulation, leading to growth of the vortices downstream.

The inwash developed into the centreline upwash (labelled B) still present at half a characteristic length behind the car. Beyond the height of the rear wing of the car, this upwash developed an outwards horizontal component contributing to the intensity of the vortices at the rear wing tips for all three configurations. An important factor in this region is the upwash flux, or the amount of upwash present in a given area. The upwash flux in the xy plane can be visualised qualitatively by the density of the planar streamtraces, with the an increased density signifying more prominent upwash. The streamtrace density for the partial and full fairings configurations could be seen to be higher at the middle of the car, as well as forming a wider column of upwash extending from the centreline to $x = 0.1w_c$. For the no fairing configuration, this upwash column extended to $x = 0.05w_c$ from the centreline. This increase in upwash column width was attributed to the larger vortices to the sides of the rear wheel created by the addition of fairings. These vortices created stronger inwash from the inwards component of the circulation which then deflected upwards towards the centre of the car.

The main difference in the plane at $z = 0.5L$ was seen in the structure of the vortices to the sides of the rear wheels (labelled C). With no wheel fairings, the vortex had largely dissipated at this distance behind the car. A small core could be seen at and $x = 0.66w_c$ and $y = 0.051h_c$. The region of circulation at this vortex was small, with this region being composed mostly of inwash towards the centreline. With the addition of partial fairings, this vortex increased in width, with the core remaining at the distance of $x = 0.66w_c$ from the midplane. The height of this vortex core moved upwards by 108% to $y = 0.106h_c$. The addition of full fairings did increase the size of this vortex but the core of the vortex moved inwards by 6% to $x = 0.62w_c$. The increase in the height position of this core was equal to 102%. This increase in vortex size at this point was attributable to the low speed flow that exited the fairings. This low-speed flow interacted with the surrounding flow of higher speed which resulted in increased turbulence here. Due to the low axial velocity, and the vertical components of the circulation here, a trailing car in this position would experience a reduction of downforce.

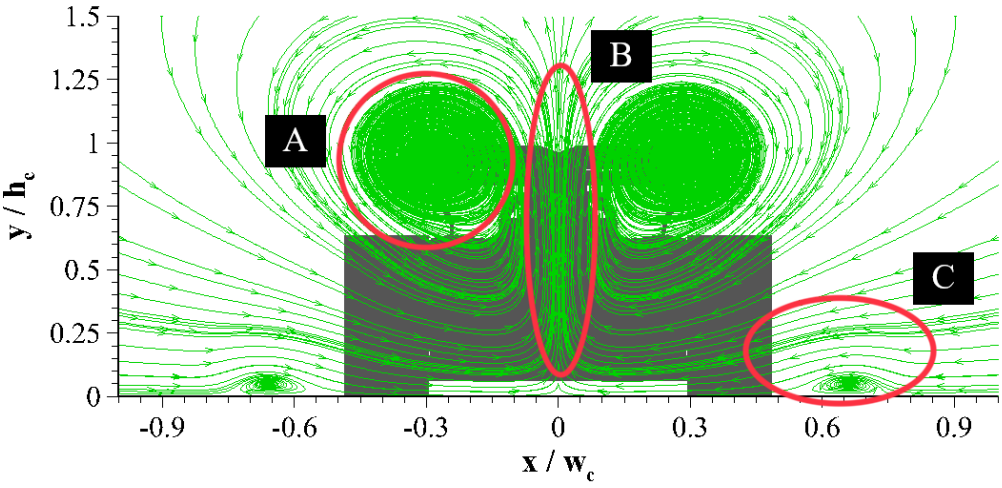


Figure 5.12: Full size planar streamtraces for no wheel fairings at $z = 0.5L$

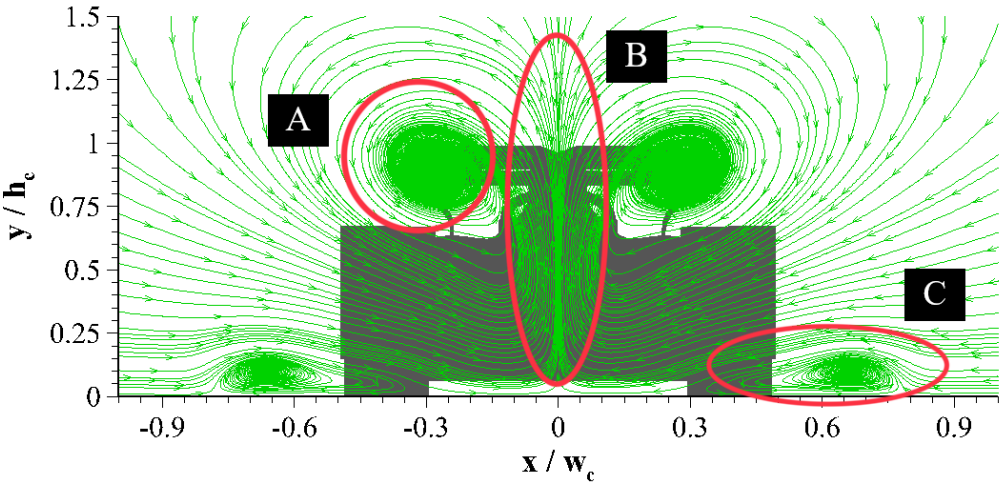


Figure 5.13: Full size planar streamtraces for partial wheel fairings at $z = 0.5L$

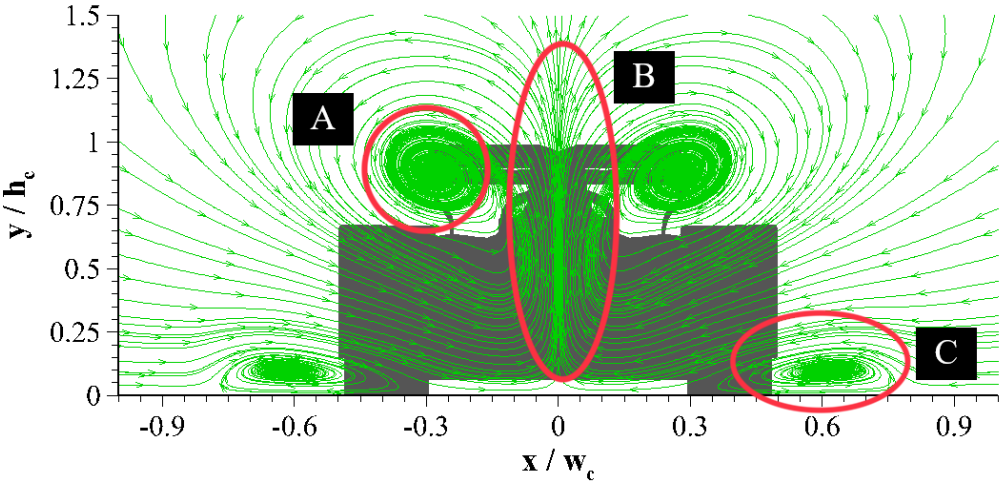


Figure 5.14: Full size planar streamtraces for full wheel fairings at $z = 0.5L$

In Figure 5.15(i), the normalised axial velocity at the ground plane was above 0.4 for all three configurations at the car centreline before decreasing. The minimum normalised axial velocity for no wheel fairings was equal to approximately 0.17 at a height of $y = 0.52h_c$. The minimum normalised axial velocity for partial wheel fairings was equal to approximately 0.21 at a height of $y = 0.73h_c$. This correlated to an increase of 23.5% in normalised axial velocity and a 40.4% increase in height position from the no wheel fairing configuration. The minimum normalised axial velocity for full wheel fairings was equal to approximately 0.27 at a height of $y = 0.83h_c$. This correlated to an increase of 58.8% in normalised axial velocity and a 59.6% increase in height position from the no wheel fairing configuration. The value of the normalised axial velocity then increased to a value of 1.0, which indicated the point of the maximum height of the wake.

The upwash components at the car centreline (shown in Figure 5.15(ii)) showed a minimum value ($\sim$0.3) of the upwash component at the ground plane for all three configurations. The upwash component then increased to a maximum value at a height of $y = 0.37h_c$ for all three configurations. This correlated roughly to the height of the diffuser exit. However the magnitude of the upwash component at this height varied between the configurations. The magnitude of the maximum upwash was equal to 8.41 m/s for the no fairing configuration. The magnitude of the maximum upwash was equal to 14.7 m/s and 17.1 m/s for the partial and full fairing configurations respectively. This correlated to an increase of 74.8% and 103% respectively from the value of the no wheel fairing configuration. The vortices formed upstream (§5.1.1) at the diffuser for the fairing configurations enhanced the upwash here. This was due to the circulation component of these vortices being upwards at the midplane. At a height of $y = 1.5h_c$, the upwash component was approximately 3.9 m/s for all three configurations. This value had not reduced to zero which indicated that the height of the wake and thus the centreline column of upwash, had grown at this axial distance behind the car.

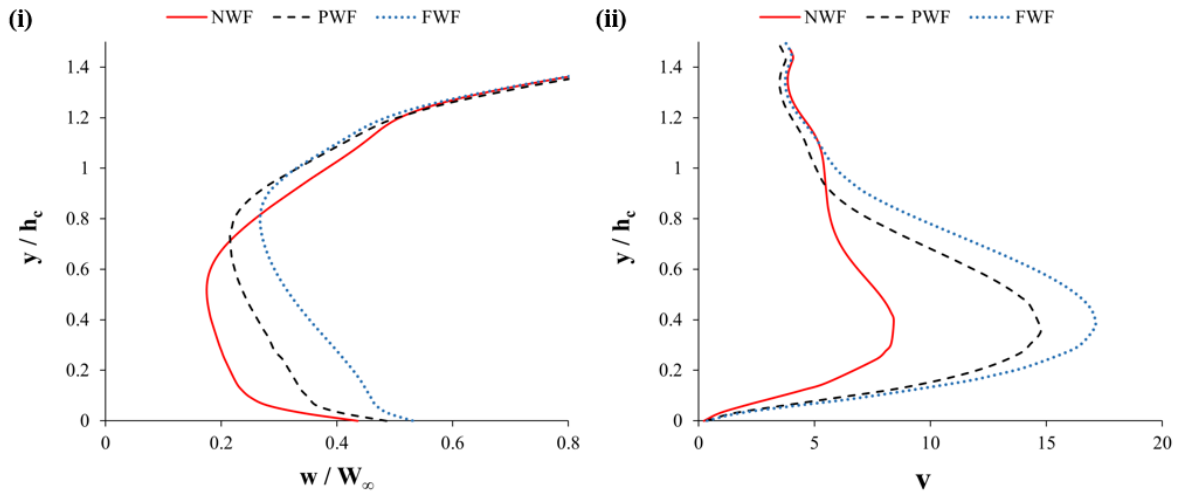


Figure 5.15: Normalised axial velocity (i) and upwash/downwash component (ii) at centreline of car in $z = 0.5L$ plane

At the wheel centreline, the normalised axial velocity (Figure 5.16(i)) increased from a minimum value at the ground plane for each configuration. At a height of $y = 0.4h_c$, the normalised axial velocity was equal to 0.86. The addition of partial wheel fairings increased this normalised axial velocity value by 11.6% from that of the no fairing configuration, to a value of 0.96. The addition of full wheel fairings increased this normalised axial velocity value by 14% from that of the no fairing configuration to a value of 0.98. A decrease in normalised axial velocity was seen at a height of approximately $y = 1.0h_c$ (i.e. the height of the car), with the highest value having corresponded to the no wheel fairing concept. This point corresponded to the position of the counter-rotating rear wing vortices. With a lower axial velocity at this point, the wheel fairings thus slightly increased the size of these low velocity vortices.

The downwash components along the wheel centreline are shown in Figure 5.16(ii). The magnitude of the downwash component was at a maximum value of 9.79 m/s at height of $y = 0.92h_c$ for the no wheel fairing configuration. The height of this maximum magnitude decreased by 9.6% to a height of $y = 0.83h_c$ for both the partial and full fairing configurations. The partial fairings resulted in a slightly higher value of 10.6 m/s, an increase of 8.37% compared to the value of the no fairing configuration. For the full fairings configuration, the downwash magnitude was approximately 10.9 m/s, an increase of 11.2% compared to the value of the no fairing configuration. The inwash to the centreline was not parallel to the ground, but rather with a downwards component. This downwash component correlated to this inwash that was enhanced by the fairings due to the stronger circulation of the vortices created to the sides of the rear wheels.

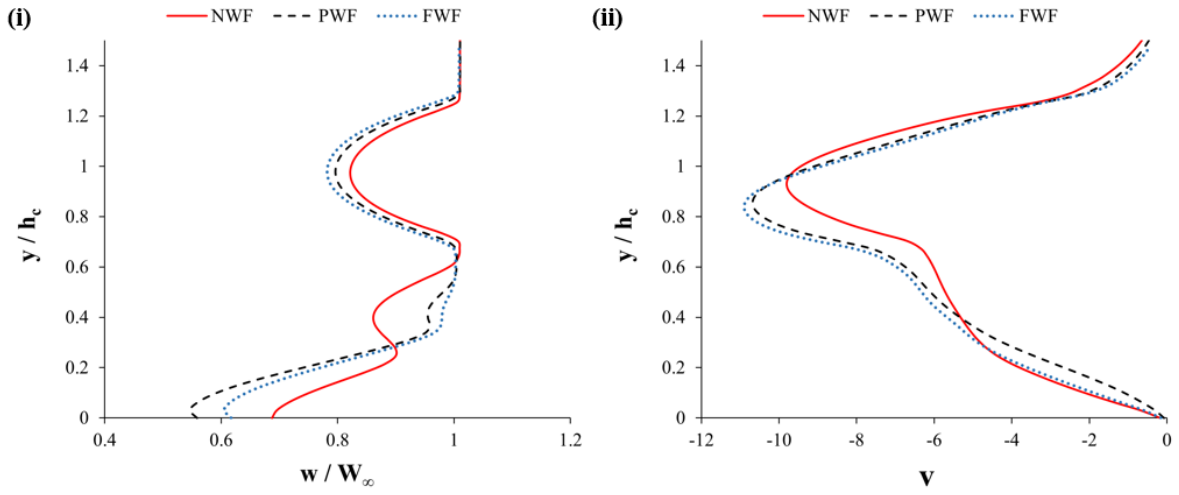


Figure 5.16: Normalised axial velocity (i) and upwash/downwash component (ii) at centreline of wheel in $z = 0.5L$ plane

5.1.3 Wake at Aft Distance of a Full Car Length ($z = 1.0L$)

In Figures 5.17, 5.18, and 5.19, the low axial velocity core of the vortices to the side of the rear wheel (labelled A) were still present for all three configurations. No discernable difference in size was seen for this region. The magnitude of the axial velocity here was highest for the no fairing configuration and lowest for the full fairing configuration. For no wheel fairings, this normalised value was equal to appropriately 0.7. For the partial fairing configuration, this normalised value decreased by 5.71% to ∼0.66. For the full fairing configuration, this normalised value decreased by 10% to ∼0.63. For all three configurations, this normalised axial velocity had increased in comparison to the plane at $z = 0.5L$, which indicated that these vortices had dissipated up until this plane. However, a lower value at this region indicated that the addition of wheel fairings adversely affected downforce generation here. The addition of wheel fairings did not prevent or reduce the vortices to the sides of the rear wheels but rather only delayed the formation and growth. The circulation of the vortices had thus not significantly dissipated at this distance downstream in comparison to the no fairing configuration. The lower axial core caused by the wheel fairings, coupled with vortex circulation, would reduce downforce generation by the front wing of a trailing car.

At the midplane of the car, the low axial velocity region (labelled B) with an approximate normalised value of 0.45 was still present in the wake structure for each configuration. For the no wheel fairing configuration, this region extended upwards from the ground plane to a height of $y = 1.39h_c$. This same maximum height was also seen for the partial and full fairing configurations. However, the addition of wheel fairings removed the centreline column

of low velocity for the entire height of the car. This low region had a minimum height at $y = 0.92h_c$ and $y = 1.01h_c$ for the partial and full fairings configurations respectively. The wheel fairings thus reduced the loss of momentum here by deflecting the turbulent flow created by rotating wheels away from the centreline.

The low velocity cores of the wing tip vortices (labelled C) has further grown in diameter at this downstream distance (i.e. vortex size is directly proportional to the downstream distance). Thus the vortices increased in diameter as axial distance downstream of the car increased due to circulation enhancement provided by the rear wheel vortices and the centreline upwash.

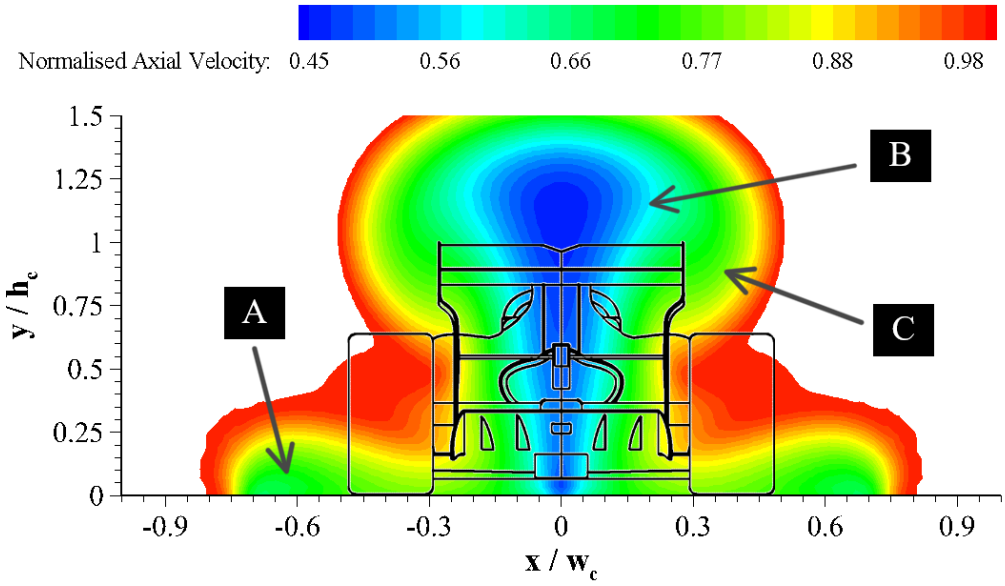


Figure 5.17: Full size normalised axial velocity contours for no wheel fairings at $z = 1.0L$

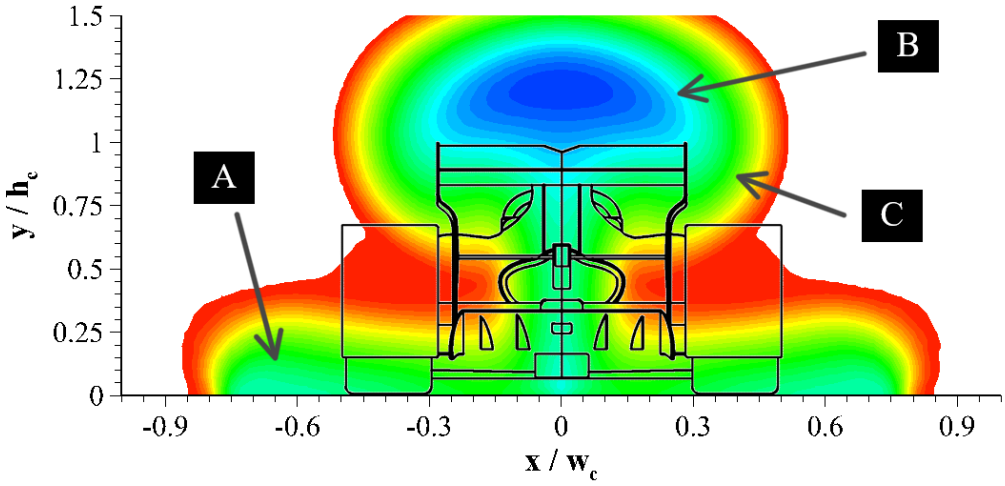


Figure 5.18: Full size normalised axial velocity contours for partial wheel fairings at $z = 1.0L$

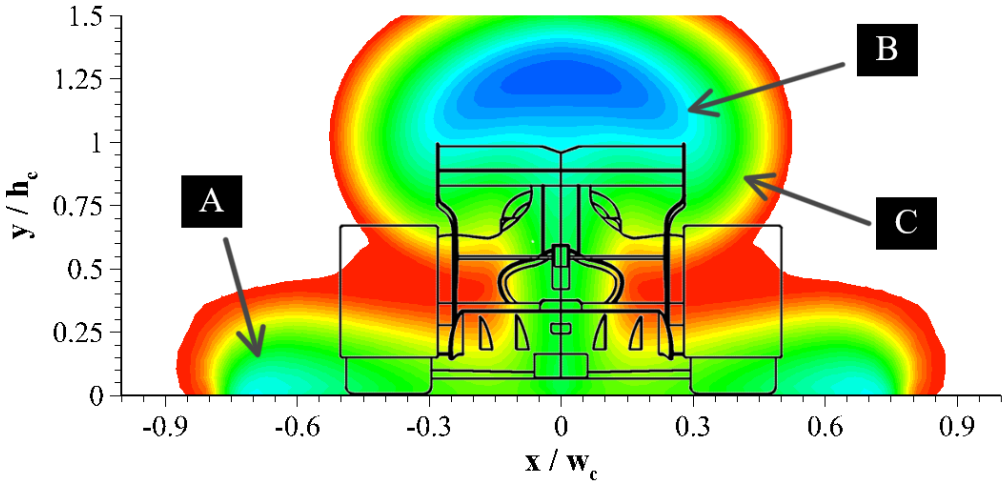


Figure 5.19: Full size normalised axial velocity contours for full wheel fairings at $z = 1.0L$

The planar streamtraces of the velocity components u and v in Figures 5.20, 5.21, and 5.22, showed the presence of the counter-rotating vortices (labelled A) and centreline upwash (labelled B). The size of the counter-rotating rear wing tip vortices was larger for the partial and full fairing configurations, indicated by the increased circulation at this point. For no wheel fairings, the vortices had begun to dissipate and reduce in size as a result of the lower upwash components at this downstream distance. This behaviour was in contrast to that at a distance of $z = 0.5L$ behind the car. This indicated that the growth of these vortices was delayed with the addition of wheel fairings. The addition of partial and full wheel fairings resulted in no discernable difference in the centreline upwash of the wake at a distance of $z = 1.0L$ behind the car. The upwash flux was still greater for the fairing configurations as was the case at $z = 0.5L$ (§5.1.2). This greater flux would result in more prominent upwash along the span of the front and rear wings of a trailing car. This would decrease the effective angle of attack more significantly.

The vortices to side of the rear wheels (labelled C) had diminished in size for all three configurations as a result of no upwash component enhancing the circulation of the vortices. This vortex was smallest for the no wheel configuration, with the core at coordinates of $x = 0.619w_c$ and $y = 0.029h_c$. The vortices present for both fairing configurations were both at a height of $y = 0.089h_c$. The core of vortex for the partial fairings configuration was at a distance of $x = 0.64w_c$ from the car midplane which correlated to an increase of 3.4%. The core of vortex for the full fairings configuration was at a distance of $x = 0.62w_c$ from the car midplane which correlated to an increase of 0.16%. For both fairing configurations, the vorticity in this region was still prominent in comparison to the no fairing configuration. Any trailing car attempting an overtake would have to move through these higher intensity vortices formed due to the addition of wheel fairings and would thus lose the necessary downforce for a successful overtake.

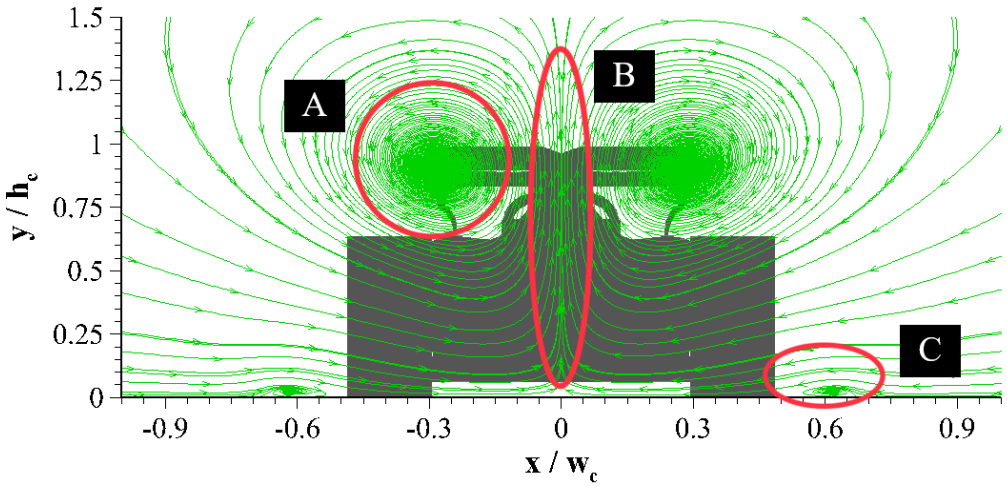


Figure 5.20: Full size planar streamtraces for no wheel fairings at $z = 1.0L$

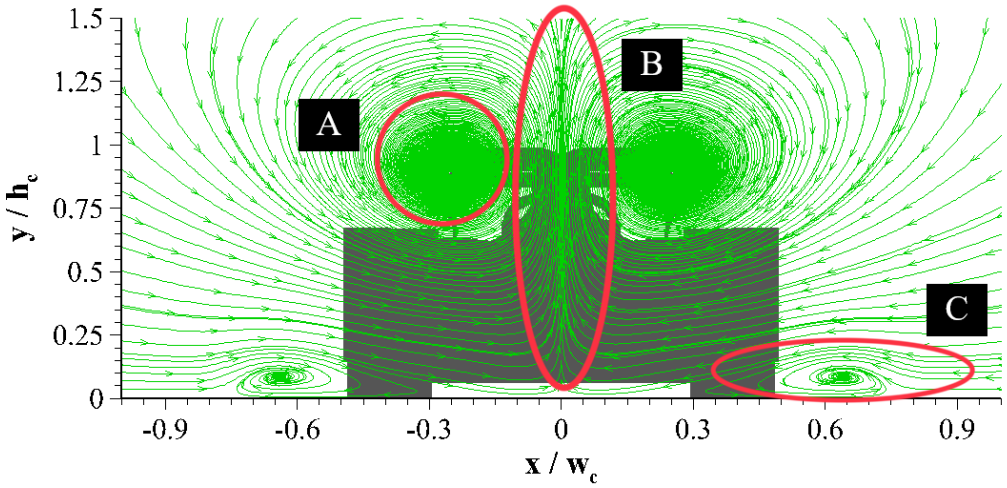


Figure 5.21: Full size planar streamtraces for partial wheel fairings at $z = 1.0L$

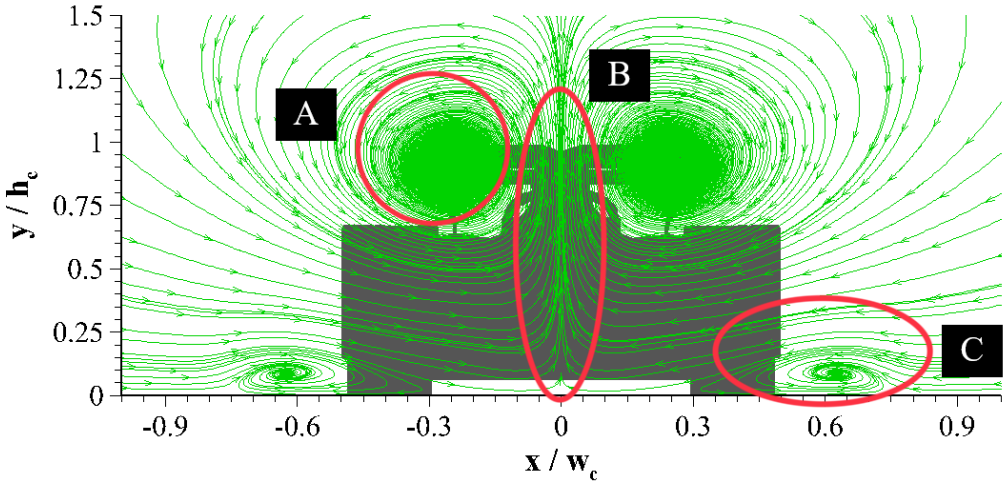


Figure 5.22: Full size planar streamtraces for full wheel fairings at $z = 1.0L$

The normalised axial velocity along the centreline in Figure 5.23(i) was lowest with an increase in height for the fairing configuration. This corresponded to the centreline line column of low velocity air specific to this configuration. A minimum value normalised value of 0.45 was present at a height of $y = 1.13h_c$ above the rear wing of the car. The minimum axial velocity of 0.47 for the partial fairing configuration was present at a height of $y = 1.19h_c$, a 4.4% increase in axial velocity, and a 5.3% increase in height. The minimum axial velocity of 0.49 for the full fairing configuration was present at a height of $y = 1.22h_c$, a 8.9% increase in axial velocity, and an 8% increase in height. At this downstream distance, the normalised axial velocity being less than 1 above the rear wing implied that the wake had grown in height and thus extended beyond the height of a trailing car.

A maximum upwash component magnitude of 9.47 m/s at the wheel centreline in Figure 5.23(ii) was at an approximate height of $y = 0.7h_c$ (just above the height of the wheel) for the no wheel configuration. With the addition of partial wheel fairings, this maximum upwash value increased by 29.9% to a value of 12.3 m/s. The height position of this maximum value increased by 14.3% to a value of $y = 0.8h_c$. With the addition of full wheel fairings, this maximum upwash value increased by 48% to a value of 14.02 m/s. The height position of this maximum value was at the same height of $y = 0.8h_c$ as the partial fairing configuration. The maximum upwash was located higher up in comparison to that at $z = 0.5L$ (§5.1.2) and this correlated with the height of the rear wing. This would alter downforce generation by the trailing car. The stronger upwash for the fairing configurations was caused by the stronger circulation of the wing tip vortices.

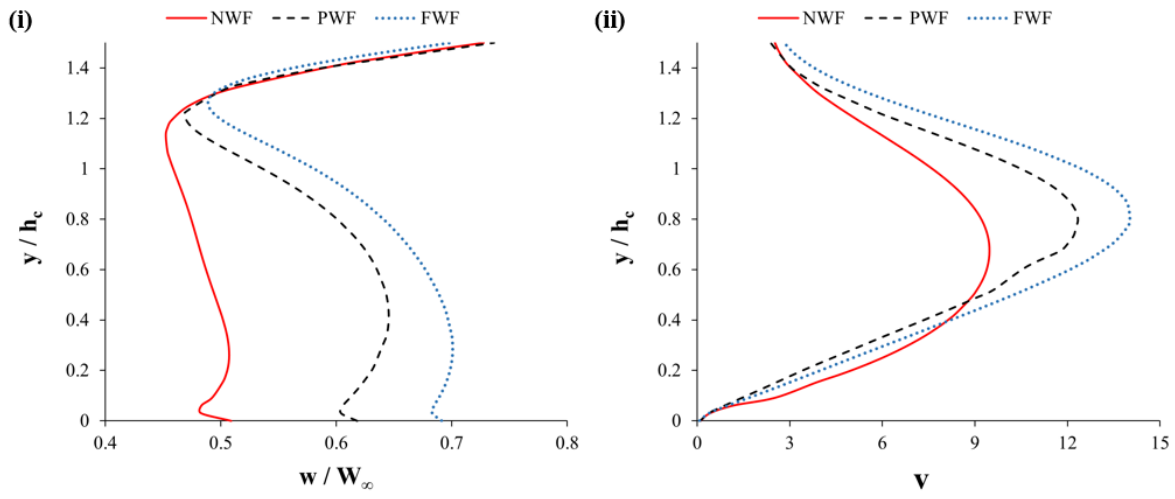


Figure 5.23: Normalised axial velocity (i) and upwash/downwash component (ii) at centreline of car in $z = 1.0L$ plane

Figure 5.24(i) shows the normalised axial velocity distribution at the wheel centreline. It was seen that between $y = 0.4h_c$ and $y = 0.58h_c$ (i.e. the top half of the wheel), that the normalised axial velocity was at an approximately constant value of 1.0 (i.e. equal to the free

stream velocity). Here the centreline column of low axial velocity air had shrunk inwards as the wake began to dissipate. The addition of wheel fairings caused the velocity to be lower up until this height, in comparison to no wheel fairings. At the height of the rear wing (y = $1.0h_c$), the normalised axial velocity decreased. This normalised value was equal to 0.76 for no wheel fairings. For partial wheel fairings, the value was equal to approximately 0.72, a decrease of 5.3%. For full wheel fairings, the value was equal to approximately 0.71, a decrease of 6.6%. Aft of the wheel, the wheel fairings decreased the downwash, adversely affecting downforce generation here.

At the wheel centreline in Figure 5.24(ii) showed that at a height of $y = 0.8h_c$, a maximum downwash component magnitude of 6.04 m/s was present for the no wheel fairing configuration. At this height, the width of the 'mushroom-like' wake is at a maximum. The downwash component of the wing-tip vortices is present here, being stronger after the addition of fairings. The distribution of the the downwash components was almost identical for the partial and full wheel fairing configuration. The maximum magnitude was equal to 5.76 m/s, a decrease of 4.75%. This was at a height of $y = 0.73h_c$, which represented a decrease in height position of 9.15%

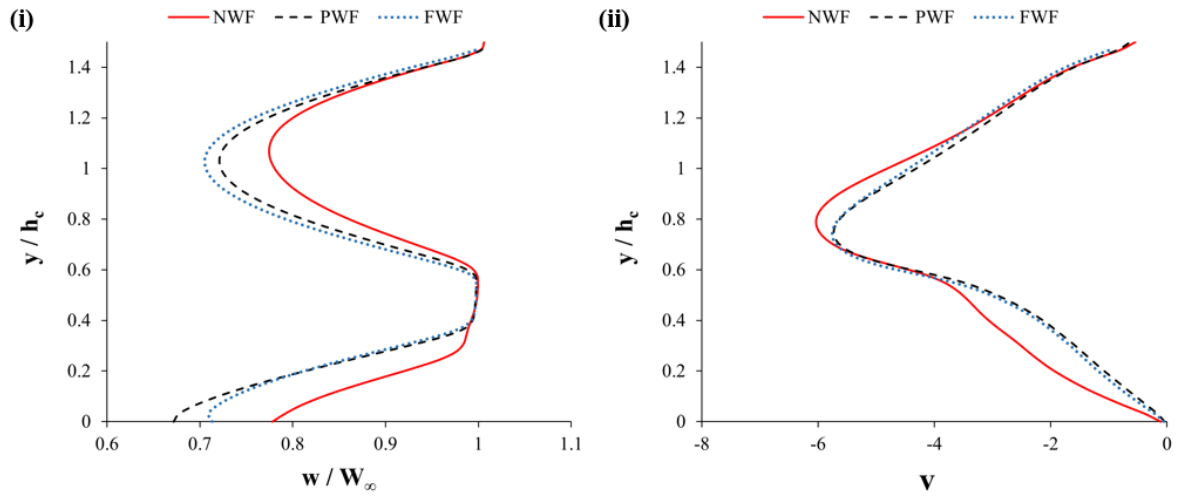


Figure 5.24: Normalised axial velocity (i) and upwash/downwash component (ii) at centreline of wheel in $z = 1.0L$ plane

5.1.4 Wake at Car Symmetry Plane

The wake structures at the symmetry plane/car midplane for each rear wheel configuration are shown in In Figures 5.25, 5.26, and 5.27. The wake structure at the rear wing of the car was directed diagonally upwards which represented the centreline upwash already noted. A substantial portion of the wake behind the car had normalised values of axial velocity in the z direction between 0.1 and 0.5 (i.e. no larger than half the value of the freestream

velocity). This was attributed to the strong upwash component here. With the air being strongly deflected upwards by the rear wing, the axial component backwards was small.

For all three configurations, there existed a core of lowest axial velocity (labelled A) in this wake portion. This core had a normalised axial velocity of ∼0.1 for the no wheel configuration. This region extended from a normalised distance of $z = 0.28L$ to $z = 0.52L$ (i.e. a normalised length of $z = 0.24L$). The height of this region extended from $y = 0.125h_c$ to $y = 0.67h_c$ (i.e. a normalised height of $y = 0.545h_c$). The addition of partial wheel fairings increased the lowest normalised axial velocity at this point by 76% to ∼0.176. The normalised length of this region was reduced by 20.8% to $z = 0.19L$, and the normalised height was reduced by 43.1% to $y = 0.31h_c$. The addition of full wheel fairings increased the lowest normalised axial velocity at this point by 110% to ∼0.21. The normalised length of this region was reduced by 58.3% to $z = 0.1L$, and the normalised height was reduced by 41.3% to $y = 0.32h_c$. The difference in height of this region between the two fairing configurations was only 3.2% and small enough to be considered insignificant. The addition of full wheel fairings increased the normalised velocity most significantly at this point. This would come at the expense of increased drag, reducing the benefits of the slipstream effect. The fairing configurations produced higher axial velocity components here due to limiting the interaction of turbulent flow from the rotating wheels (as noted at $z = 0.5L$, §5.1.2).

The distance behind the car where the axial velocity had returned to at least half of the freestream value (labelled B) was also altered by the addition of wheel fairings. The region below this value extended past a distance of one characteristic length ($z = 1.0L$) behind the car with no wheel fairings. By adding partial wheel fairings, this normalised distance was reduced to a value of $z = 0.77L$, a decrease of 11.5%, With the addition of partial wheel fairings, this value decreased by 14.5% to a value of $z = 0.71L$. This was once again attributable to the lower centreline disturbance created by the fairings.

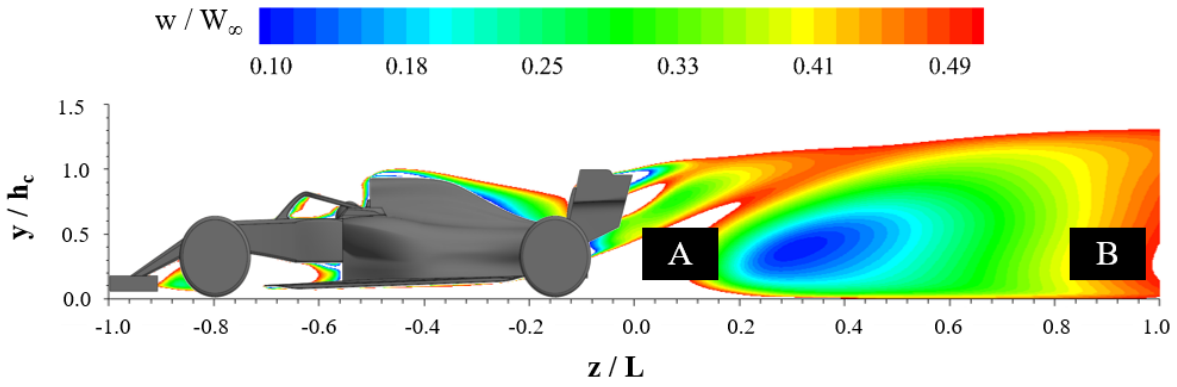


Figure 5.25: Normalised axial velocity contours in car symmetry plane for no wheel fairings

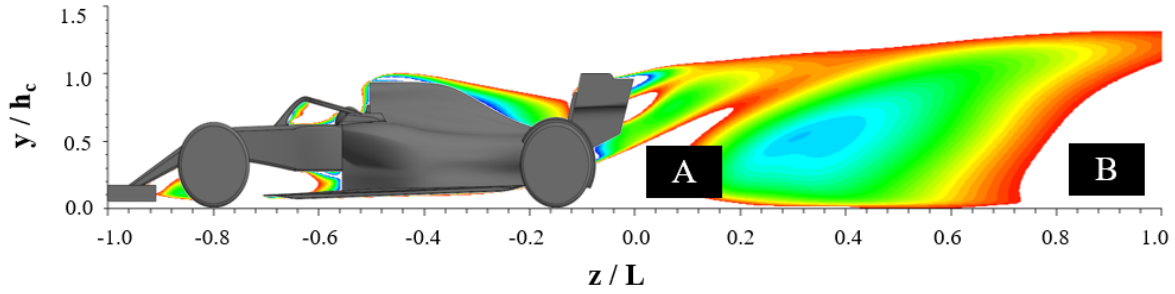


Figure 5.26: Normalised axial velocity contours in car symmetry plane for partial wheel fairings

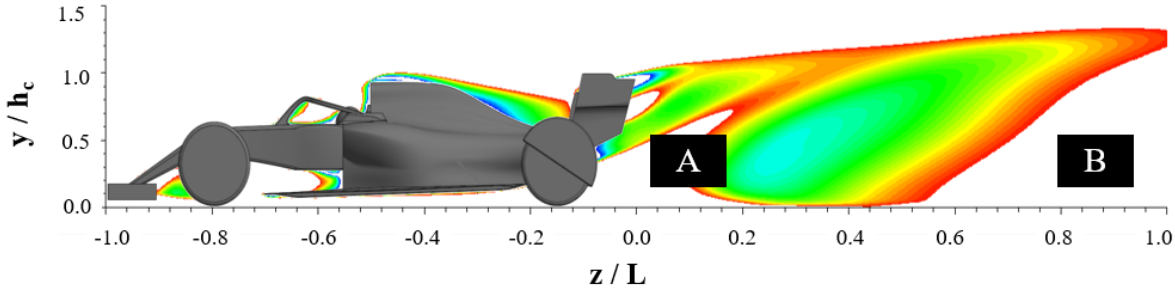


Figure 5.27: Normalised axial velocity contours in car symmetry plane for full wheel fairings

Figure 5.28 show the normalised axial velocity and upwash velocity component distribution behind the car at the height of the front wing. The front wing of a trailing car is the first downforce generating component exposed to the turbulent wake of a leading car. The forces generated here would therefore have a significant impact on the aerodynamic balance of the trailing car.

The normalised axial velocity distribution in Figure 5.28(i) showed that all three configurations had a similar normalised axial velocity of ∼0.7 immediately aft of the car in the symmetry plane. The normalised axial velocity then dropped significantly further away from the car until reaching a minimum point. The no wheel configuration had the lowest value of these minimum points (a normalised value of 0.21), at a normalised distance of $z = 0.34L$ aft of the car. With partial wheel fairings, this minimum normalised axial velocity changed by 33.3% to 0.28. The distance of this point aft of the car slightly increased by 8.82% to $z = 0.37L$. With full wheel fairings, this minimum normalised axial velocity changed by 28.6% to 0.27. The distance of this point aft of the car slightly decreased by 26.5% to $z = 0.25L$. This low axial velocity correlated to the formation of the centreline column of low speed air with the higher disturbance from the exposed wheels causing the more significant low speed column (as noted at $z = 0.5L$, §5.1.2) . After this minimum value, the normalised axial velocity once again increased up until one characteristic length behind the car. At this distance, the no wheel fairing configuration had the lowest normalised value of ∼0.49. For partial fairings, this value increased by 24.5% to ∼0.61. Full wheel fairings resulted in the

highest normalised value at this distance aft of the car with a value of ∼0.69, an increase of 40.8%. Full fairings thus caused a return to freestream conditions further upstream as the axial wheel disturbance was reduced.

The upwash components in Figure 5.28(ii) showed an initial decline for all three configurations up until a distance of $z = 0.33L$. At this point, the magnitude of the upwash peaked with a maximum value having occurred for the partial and full wheel fairing configurations. The upwash component at this point was equal to approximately 4.6 m/s for the no wheel fairing configuration. The addition of partial fairings increased this component to 8.8 m/s, an increase of 9.13%. The full fairings resulted in an increase of 144% to a value of 11.2 m/s. These were substantial increases that would greatly reduce the effective angle of attack of the front wing, thus reducing downforce here. This stronger upwash was caused by the larger side wheel vortices associated with the addition of fairings, along with the upwards circulation of the vortices formed at the exit of the diffuser (§5.1.1). The stronger inwash component of the circulation of these vortices thus manifested as stronger centreline upwash upon reaching the midplane of the car. This peak was followed by a decrease in upwash up until a distance of $z = 1.0L$ (i.e. one car length downstream). Here, the upwash was highest for the no fairing configuration, with an approximate value of 2.54 m/s. This value was approximately 1.71 m/s for the partial fairing configuration and 1.99 m/s for the full fairing configuration. This correlated to a decrease of 32.7% and 21.7% respectively.

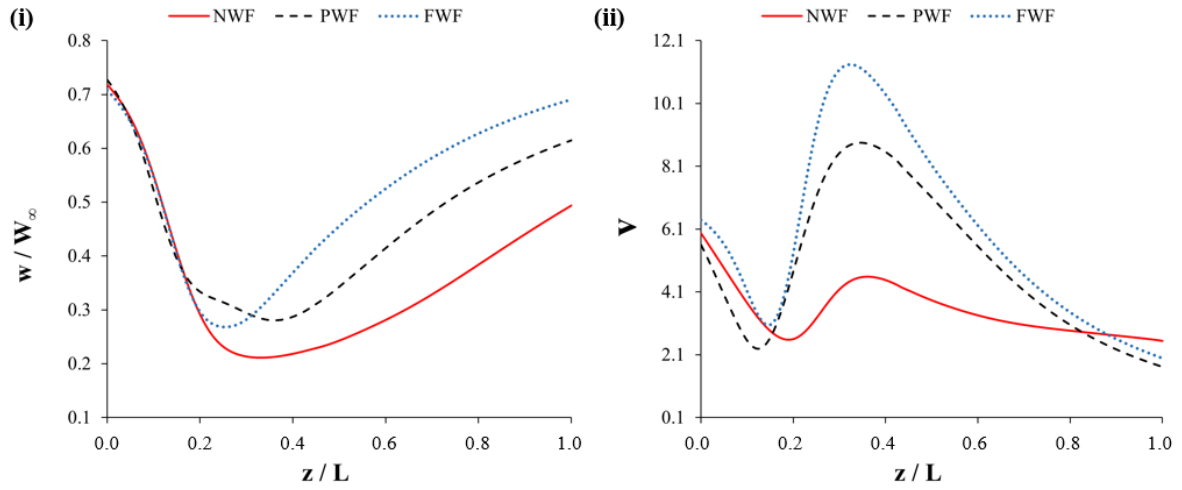


Figure 5.28: Normalised axial velocity (i) and upwash/downwash component (ii) in car symmetry plane

5.1.5 Wake at Wheel Midplane

The normalised axial velocity at the wheel midplane in Figures 5.29, 5.30, and 5.31 showed different wake structures aft of the wheel between the three configurations. A low velocity region existed aft of the wheel (labelled A) which was consistent with a cylindrical object in cross-flow. For the no wheel fairing configuration, the separation point along the circumference of the wheel existed at the top surface of the wheel. This separation point existed further upstream due to the increased velocity gradient caused by the rotation of the wheels. This earlier separation point caused a larger wake behind the wheel which extended back to a normalised distance of $z = 0.0421L$ behind the car. This wake was prominent for the entire height of the rotating wheel. With the addition of both fairing configurations, this separation point was delayed to the back surface of the wheel further downstream, which resulted in a smaller low velocity wake. The fairings resulted in a stationary cylinder surface in the cross-flow, with the associated delayed separation, due to the reduced velocity gradient. Both the partial and full wheel fairings resulted in the low velocity region of this wake extending to a length of $z = 0.013L$ behind the car, a decrease of 69.1%. The wake for these configurations was only prominent half of the wheel height. While the fairings decreased the size of this low velocity wake, this would not have any practical implications on the downforce generation for the trailing car. This is because a trailing car is unlikely to follow a leading car at a distance close enough to this low velocity region as this would result in a high likelihood of a collision should a leading car decrease its speed.

The distance downstream of the car in the wheel midplane where the normalised velocity had returned to half of the value of the freestream velocity is labelled B. Downstream and above these contours, the normalised axial velocity was above half the freestream value. For no wheel fairings, this normalised axial velocity of 0.5 began at $z = 0.25L$ downstream of the car. The addition of partial fairings increased the distance of this point downstream of the car by 32% to $z = 0.33L$. While this point extended further downstream, the region of normalised velocity below 0.5 had decreased in height above the ground plane. Full wheel fairings resulted in the axial velocity returning to half the freestream value at a distance of 0.203, a decrease of 18.8%. The full wheel fairings thus caused the effects of the wake at the wheel midplane to dissipate furthest upstream as a result of the smaller wake aft of the wheel (§5.1.1).

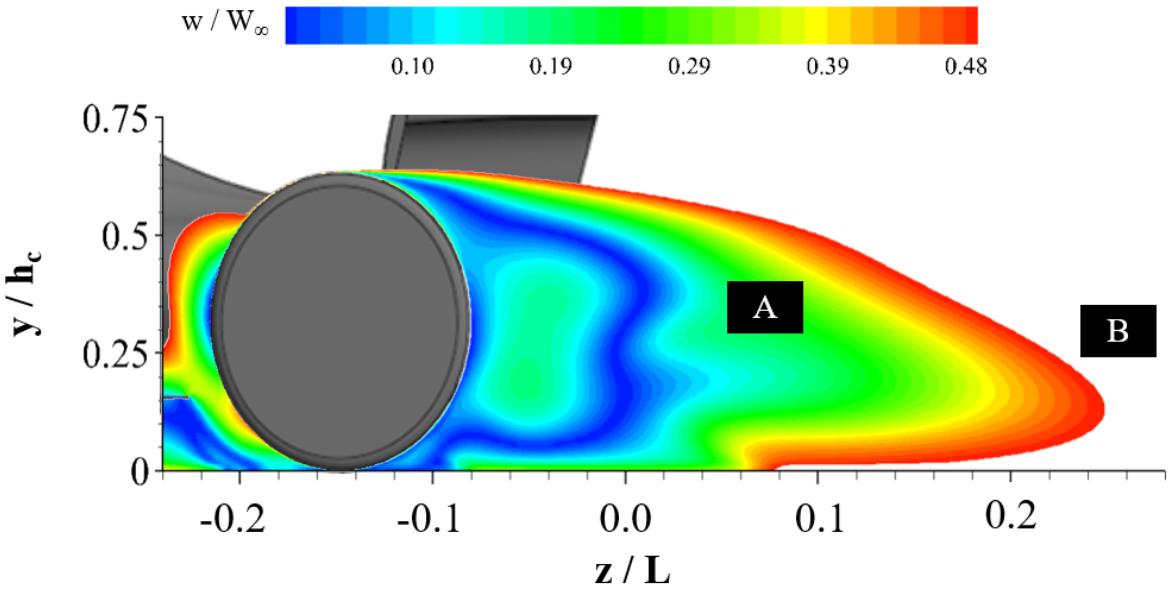


Figure 5.29: Normalised axial velocity contours in wheel midplane for no wheel fairings

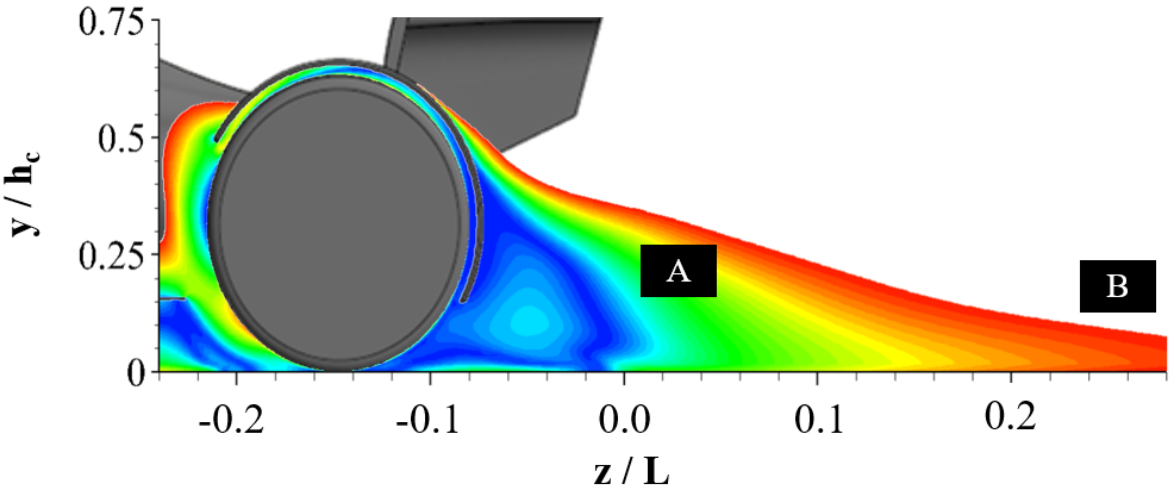


Figure 5.30: Normalised axial velocity contours in wheel midplane for partial wheel fairings

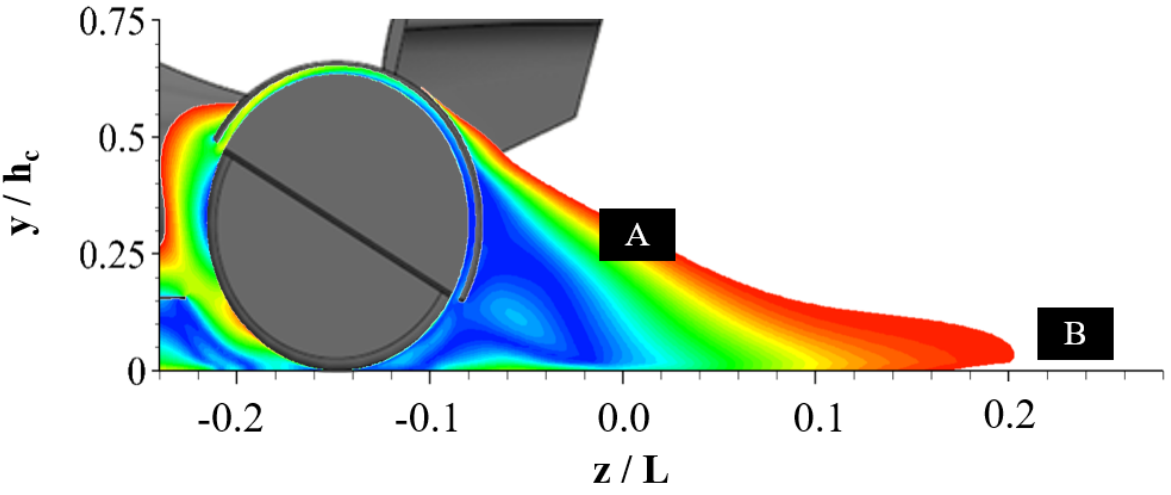


Figure 5.31: Normalised axial velocity contours in wheel midplane for full wheel fairings

The normalised velocity in the wheel midplane from the back of the rear wheel (shown in Figure 5.32(i)), at a height of the front wing, showed a point of 0.0 normalised axial velocity at different locations for each configuration. This was due to vortex shedding in yz plane, along with the expansion of air exiting the enclosed fairings. For no fairings, this point was located at a distance of 0.01 upstream from the plane immediately aft of the car ($z = 0.0L$). With partial wheel fairings, this point moved upstream by a normalised distance of 0.02, and for full wheel fairings, upstream by a distance of 0.03. This difference in position was not significant as this point existed too close to the leading car to allow for a safe following distance for the trailing car, and thus the no downforce advantage would be experienced. The normalised axial velocity increased downstream as the wheel wake dissipated, reaching the previously discussed positions where a return to half the freestream velocity was seen.

The downwash velocity components at the height of the front wing (shown in Figure 5.32(ii)) increased in magnitude with the addition of wheel fairings. A stronger upwash component was seen for the no wheel configuration. The addition of fairings reversed the vertical flow direction by creating a downwards enclosed path to the bottom of the fairing. This caused downwash components to become prominent. The maximum upwash component magnitude for the no fairing configuration was equal to 5.94 m/s. For partial and full fairings, this maximum magnitude increased to 12.4 m/s and 16.6 m/s respectively. The maximum upwash component for no wheel fairings occurred upstream of the plane immediately aft of the car, where no trailing car could operate. By changing the vertical component from upwash to downwash, the effective angle of attack for a trailing car increased which could result in higher levels of downforce. Full fairings would be most effective here as the highest magnitude of downwash was produced. Further downstream, the downwash transitioned to upwash components as the air exiting the fairings interacted with that which separated along the circumference of the fairing, which gave rise to the wheel wake.

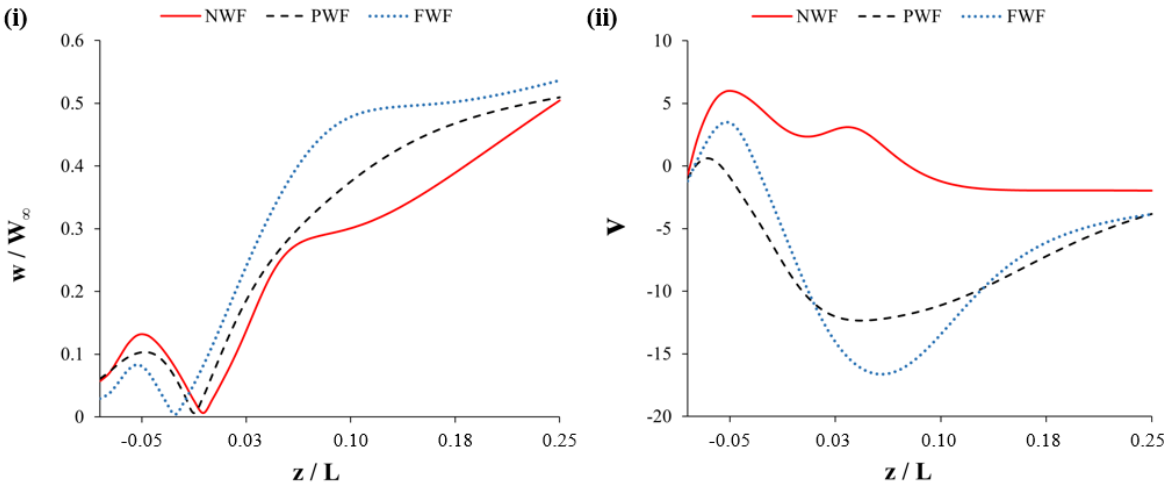


Figure 5.32: Normalised axial velocity (i) and upwash/downwash component (ii) in wheel midplane

5.1.6 Streamlines at Rear Wheel

The streamlines for the no fairing configuration in Figure 5.33 show that the flow separated at the point labelled A towards the top of the wheel, slightly downstream of the vertical midplane of the wheel. This led to the formation of the large turbulent wake aft of the wheel (indicated by the erratic streamlines and backflow labelled as B). These streamlines were also of low normalised axial velocity (between 0.0 and 0.25) which indicated a dynamic pressure deficit aft of the wheel. This large turbulence, with a high variation of upwash and downwash magnitude, would result in inconsistent levels of downforce of a car positioned in this wake. Air was also forced outwards to the side of the wheel (labelled C) by the rotation of the wheels which contributed to the vortices to the sides of the wheel.

The streamlines for the partial fairing configuration in Figure 5.34 show that the air flow in the enclosed space between the wheel tread and fairing surface escaped at the sidewall of the wheel (labelled A). These streamlines indicated an acceleration of this escaped flow. The addition of fairings resulted in low velocity air in the the enclosed space shrouding the wheels. This caused a high static pressure to build up in this space. With the sidewalls of the wheels uncovered, the pressure differential between the enclosed air and that flowing past the car was large, resulting in this air flowing out from the enclosed fairing space. This static pressure would also alter the drag and downforce experienced by the car itself. Air also escaped from the bottom of the fairing (labelled B). This resulted in expansion at this point which slowed the air down and caused the formation of the low velocity (and turbulent) wake aft of the wheel. These streamlines moved towards the centreline due to the pressure differential caused by the low speed air at the exit of the diffuser. The air forced outwards from the bottom of the rotating wheels (labelled C) was seen to remain unaltered by the addition of the partial fairings.

The streamlines for the full fairing configuration in Figure 5.35 showed that the air flow in the enclosed fairing space also escaped from underneath the sidewall covers (labelled A) due to the static pressure build-up. This escaped air was drawn in towards the low velocity wake aft of the wheel caused by expansion. This wake was smaller than the other two configurations, with the region of high turbulence being localised to a region aft of the wheel (labelled B). Once again, air was pushed out from the bottom of the wheels (labelled C), which formed the vortices at the sides.

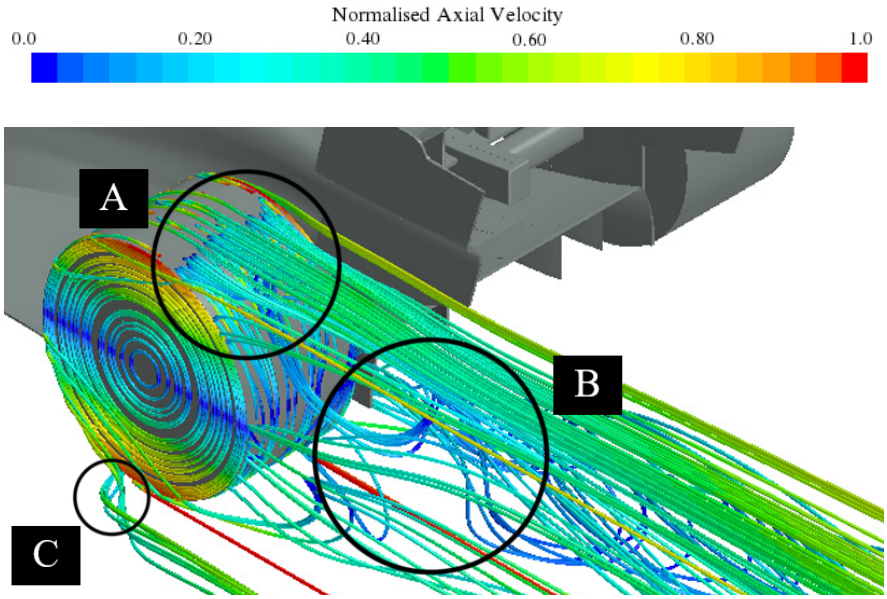


Figure 5.33: Streamlines at rear wheel for no wheel fairings

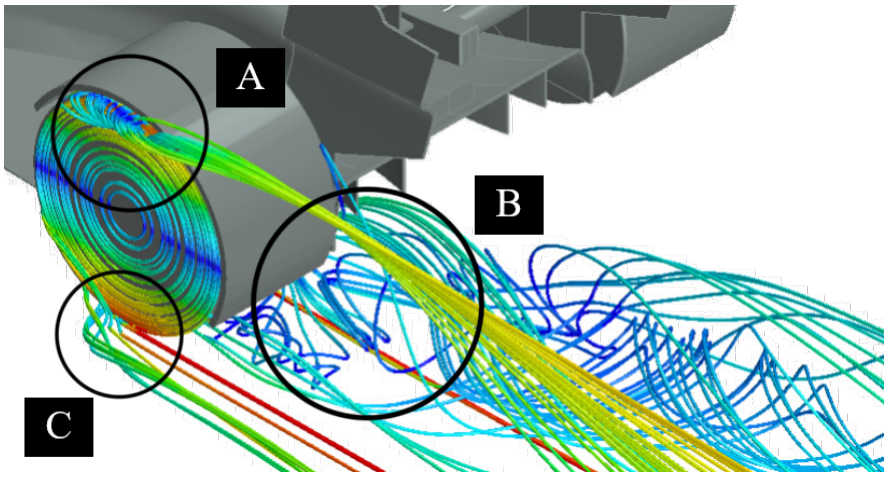


Figure 5.34: Streamlines at rear wheel for partial wheel fairings

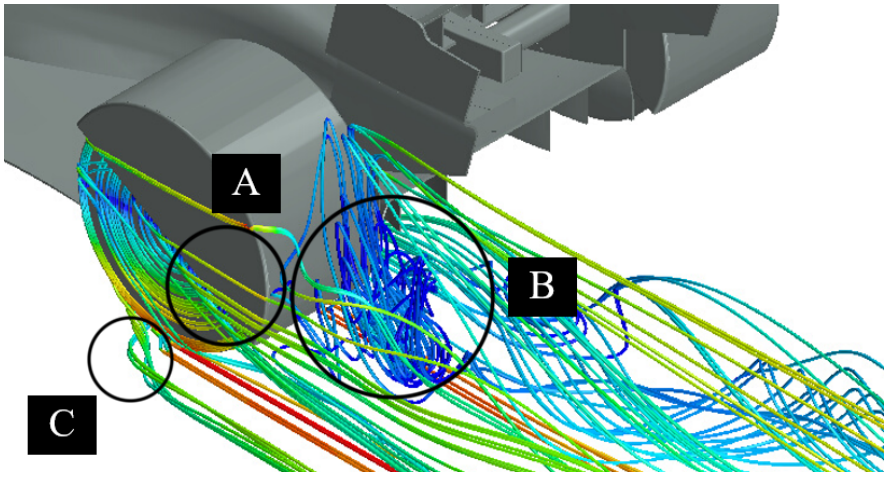


Figure 5.35: Streamlines at rear wheel for full wheel fairings

Wheel fairings resulted in the separation point over the wheel being further downstream than the no fairing configuration. This was because the earlier separation point along the wheel tread was covered by the fairings, with the wake being heavily influenced by the flow over the stationary fairing. This altered the turbulence aft of the wheel, with the full fairings having localised this wake closer to the aft portion of the wheel and fairing.

5.1.7 Summary of Numerical Wake Survey

The most significant changes in the wake structure of a leading car by the addition of wheel fairings (partial and full) are the changes in the vortices of the wake, along with the changes in upwash. These flow structures are of primary importance to a trailing car operating in a leading car's wake as both factors influence the drag and downforce experienced by the trailing car.

The upwash flux towards the midplane of the car (i.e. slipstream) was increased by the addition of fairings. Thus it was expected that the addition of both partial and full fairings would decrease the downforce of a trailing vehicle operating in the wake, by reducing the effective angle of attack for the wings of a trailing car. Due to the increase in axial velocity at the centreline, drag of the trailing car would also increase in the slipstream.

The addition of wheel fairings increased the size of the vortices to the sides of the rear wheels downstream of a leading car. This resulted in higher circulation here, along with larger cores of low speed axial velocity. A trailing car attempting an overtaking manoeuvre would be exposed to these vortices. This would cause a resultant loss of downforce. However, drag would be expected to decrease here due to the oncoming axial flow having a lower magnitude.

5.2 Aerodynamic Performance of Trailing Car

To further interrogate the effect of the two different wheel fairing configurations, numerical simulations were conducted to determine the change in drag and lift forces experienced by a trailing car. These have been presented as dimensionless drag and lift coefficients for a trailing car. However, the non-dimensional nature of these coefficients did not allow for the simulations to be validated with scaled models due to the lack of Reynolds number independence for these force coefficients between the full size and scale results (§4.2). Thus, in the absence of such validation, these results should only be considered an initial indication of any potential aerodynamic changes. The four considered trailing positions, A – D, have been defined previously in Figure 3.6 (§3.4.2). For each trailing (downstream) position, the force coefficients for a trailing car with partial and full fairings were compared to the

coefficients for a trailing car with no fairings, at the same downstream position. For each configuration, the drag and lift coefficients for a single car in undisturbed air were used as a baseline for comparison purposes. Differences between the baseline force coefficients and the force coefficients of a trailing car of each configuration represented the aerodynamic effect on a trailing car, caused by the presence of an upstream car. The different fairing configurations were applied simultaneously to both the leading and trailing cars such that the rear wheel configurations were the same for both the leading and trailing car for a given simulation. The mean converged force coefficients are presented in the form of bar graphs. Solid coloured bars of the graphs represent the force coefficients of a trailing car of a particular configuration at the stipulated trailing distance downstream. Bars with hatch patterns are representative of the baseline force coefficients of a single car in undisturbed air with a particular rear wheel configuration. The calculated force coefficients are expressed with three significant figures. This was a conservative representation as this level of precision is lower than the associated machine round-off precision. All converged force coefficient values were assumed to lie within three standard deviations above and below the mean. This correlated to small error bars that are not visible on a plot. For example, a drag coefficient of 0.250 was associated with a maximum uncertainty of ± 0.0002 and therefore would not alter the quoted value with the associated number of significant figures. The error for these force coefficients was thus considered small. An adequate level of accuracy was achieved as meaningful comparisons could still be made between force coefficients.

In Figure 5.36(i), the drag coefficients of a trailing car for each configuration are shown for position A. At this position, a trailing car with no fairings had the lowest drag coefficient of 0.50. The addition of partial wheel fairings increased the drag coefficient of the trailing car by 14.1% in comparison to a trailing car with no fairings at the same downstream position. The addition of full wheel fairings increased the drag coefficient of the trailing car by 17.8% in comparison to a trailing car with no fairings at the same downstream position. This drag increased as a result of the increased axial velocity caused by the wheel fairings, along with a higher momentum loss associated with the larger vortices to the sides of the rear wheels. The lift coefficients of a trailing car at position A are shown in 5.36(ii). At this position, a trailing car with no fairings had the highest lift coefficient of 0.11. The addition of partial and full wheel fairings decreased the lift coefficient of the trailing car by 25.9% and 23.6% respectively, in comparison to that of a trailing car with no wheel fairings at the same downstream position. The decrease in lift coefficient was due to the increased upwash flux caused by the addition of the fairings.

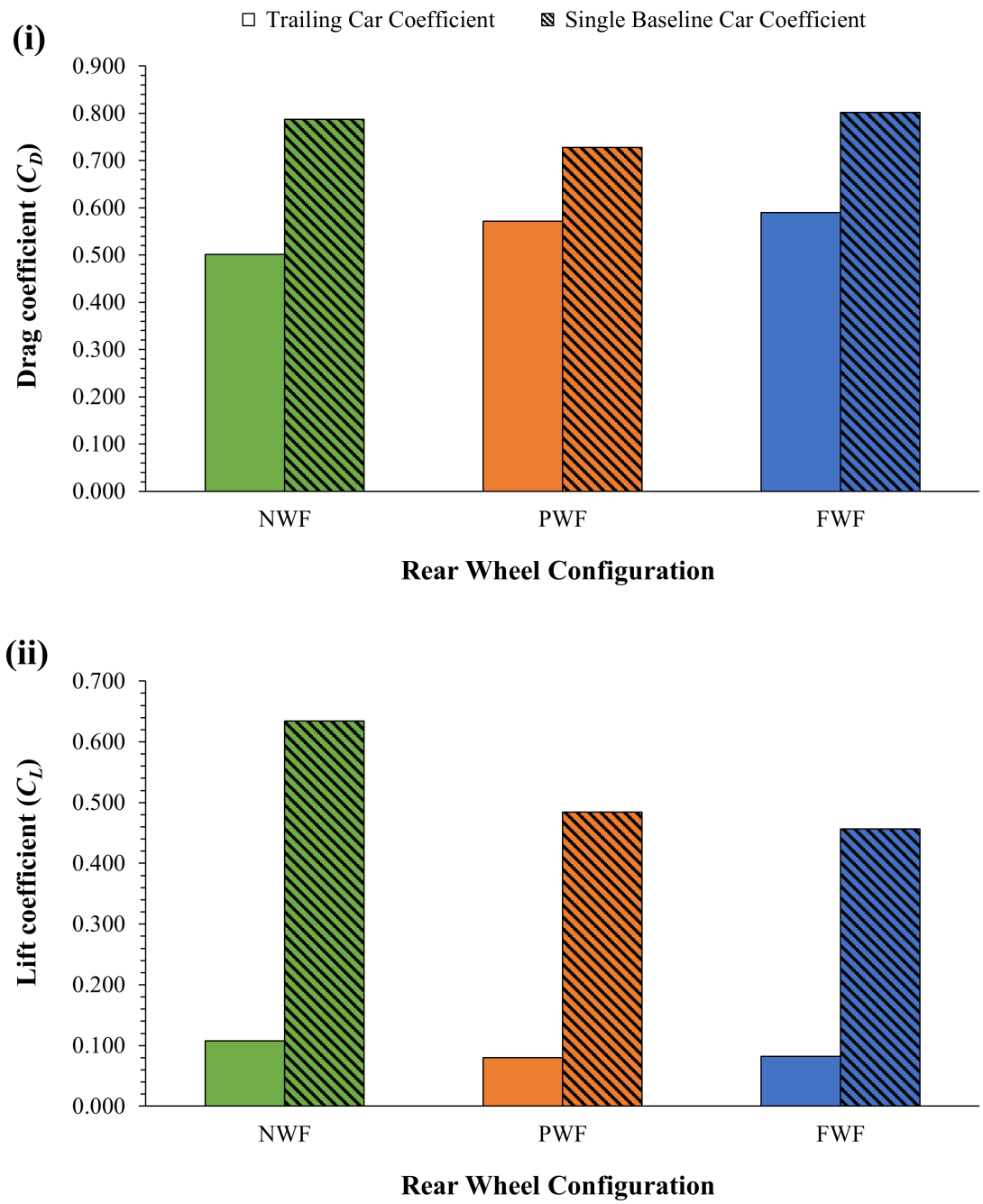


Figure 5.36: Comparison of (i) drag coefficients and (ii) lift coefficients for all configurations at trailing position A

The drag coefficients of a trailing car at position B are shown in Figure 5.37(i). At this position, a trailing car with no fairings produced the lowest drag coefficient of 0.570. In comparison to a trailing car with no fairings at this downstream position, the addition of partial wheel fairings increased the drag coefficient by 6.67%, and the addition of full fairings increased the drag coefficient by 7.44%. The lift coefficient of a trailing car for each configuration at position B is shown in Figure 5.37(ii). This value was highest for a trailing car without any wheel fairings attached, with a value of 0.210. At this position, the addition

of partial and full fairings reduced the lift coefficient of a trailing car by 13.1% and 16.5% respectively, in comparison to a trailing car with no wheel fairings. An increase and drag coefficient and a decrease in lift coefficient was observed at position B due to the same previously described phenomena at position A. However these differences in force coefficients between the fairing and no fairing configurations were lower at position B. This indicated the effects of the slipstream were less prominent further downstream from the leading car.

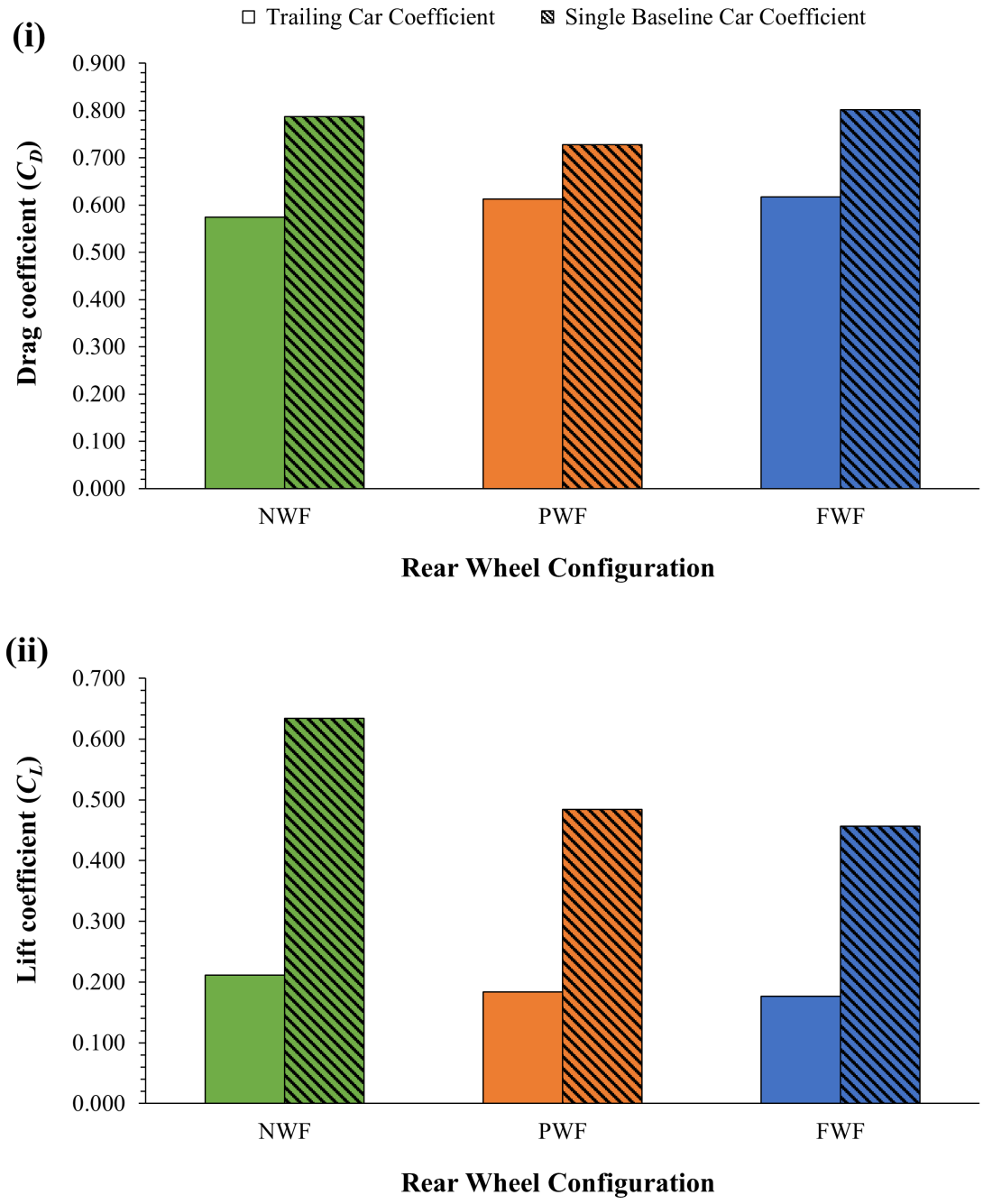


Figure 5.37: Comparison of (i) drag coefficients and (ii) lift coefficients for all configurations at trailing position B

Trailing positions A and B correlate directly to the slipstream behind a leading car. The slipstream effect was seen due to the decrease in the trailing car drag coefficient in comparison to the baseline for all configurations. For all three configurations, a decrease in lift coefficient from the baseline values was observed. This indicated the previously noted phenomenon of a trailing car losing downforce due to the turbulent wake (dirty air) of a leading car. The main aerodynamic benefit for a trailing car operating in a slipstream is a reduction of drag. The addition of wheel fairings has increased the drag coefficients for a trailing car at both downstream positions in the slipstream. This was attributed to the higher normalised axial velocity at the wake centreline caused by the addition of wheel fairings, as the drag force was directly proportional to the magnitude of the axial velocity. The addition of wheel fairings also increased the momentum loss of the car, with increased momentum transfer to the larger wheel vortices caused by the fairings. These larger rear wheel vortices induced larger turbulent wakes by enhancing the upwash and counter-rotating rear wing vortices. By moving through these larger turbulent wakes, a trailing car would experience an increase in drag. The increase in drag caused by the addition of wheel fairings would result in a trailing car not being able to follow a leading car as closely thus diminishing overtaking opportunities. The addition of partial and full wheel fairings caused a reduction in lift coefficient for a trailing car due to the associated alteration of the centreline upwash component. The full wheel fairing configuration caused the greatest loss of downforce due to the creation of the strongest upwash component. These observations correlated with the previously made predictions (§5.1.7).

In Figure 5.38(i), the drag coefficients for a trailing car are shown for position C for all three configurations. At this position, the trailing car drag coefficient for the no fairing configuration was lowest with a value of 0.78. With partial wheel fairings, the drag coefficient increased by 2.67% in comparison to a no fairing configuration at the same position. With the addition of full wheel fairings, the drag coefficient increased by 0.92% in comparison to a no fairing configuration at the same position. This increase in drag coefficients between the fairing and no fairing configurations was attributable to the larger rear wheel vortices associated with the increased car momentum loss by the addition of fairings. However, these changes were too small to be considered significant. The lift coefficients are shown in Figure 5.38(ii). The lift coefficient of a trailing car was highest for the no fairing configuration, with a value of 0.65. Partial and full wheel fairings caused a decrease in lift coefficient by 23.8% and 26.7% respectively, in comparison to the no fairing configuration at the same downstream position. This reduction of lift coefficient was due to the increased upwards circulation component of the vortices to the sides of rear wheels of the lead car.

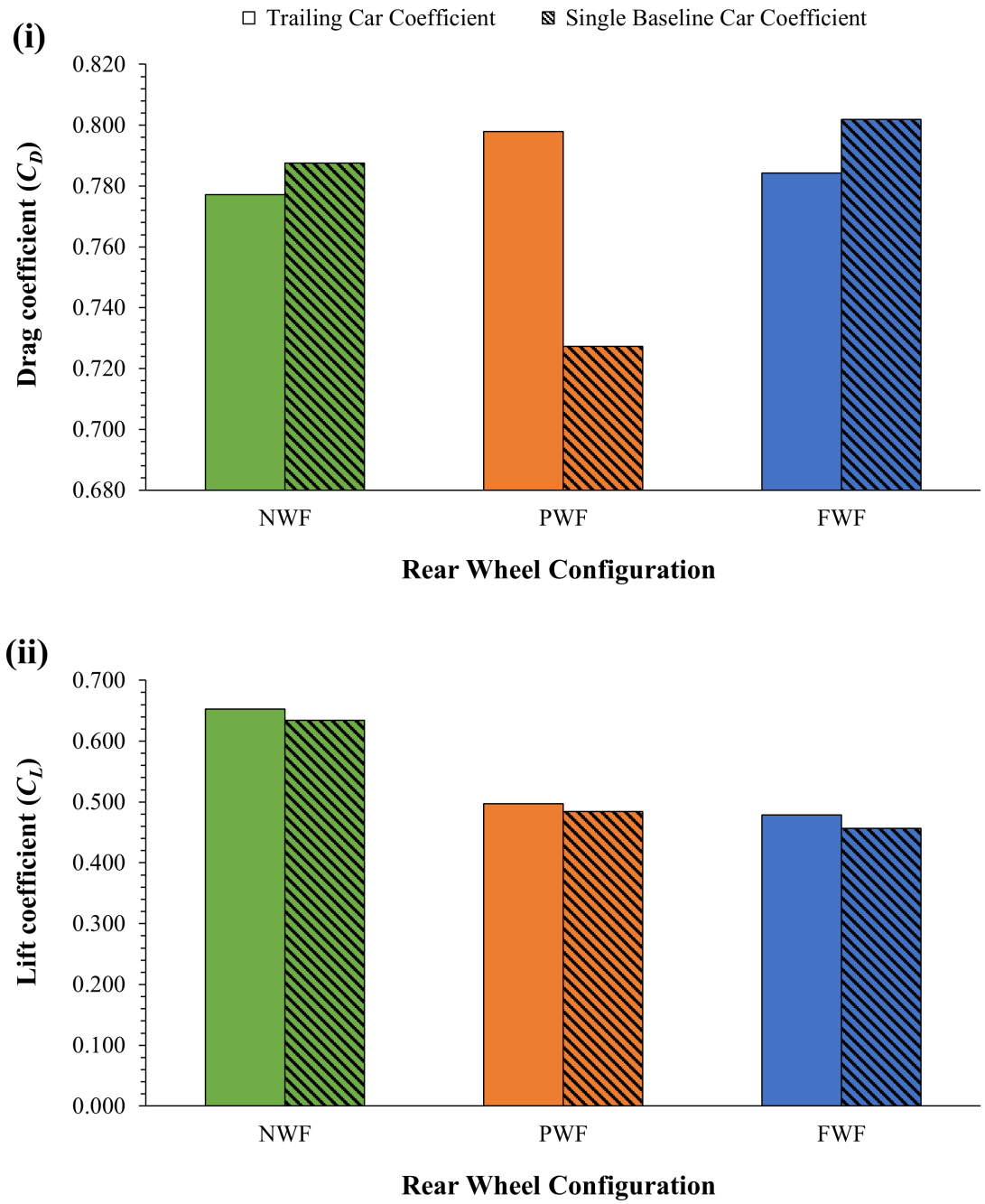


Figure 5.38: Comparison of (i) drag coefficients and (ii) lift coefficients for all configurations at trailing position C

The drag coefficients for a trailing car at position D, for all three configurations, are shown in Figure 5.39(i). The trailing car with a no fairing configuration resulted in the lowest drag coefficient, with a value of 0.78. The addition of partial fairings resulted in an increase in drag coefficient of a trailing car by 1.09% in comparison to a no fairing configuration at the same position. The addition of full fairings to a trailing car resulted in an increase in drag coefficient by 0.35% in comparison to a no fairing configuration at the same position.

The lift coefficients of the trailing car at position D are shown in Figure 5.39(ii). With no wheel fairings attached, the lift coefficient was at a maximum value of 0.66 for a trailing car. By adding partial fairings, the lift coefficient of the trailing car was reduced by 25.5% in comparison to the no fairing configuration. By adding full fairings, the lift coefficient of the trailing car was reduced by 25.8% in comparison to the no fairing configuration. The changes in force coefficients was attributable to the same flow phenomena described at position C.

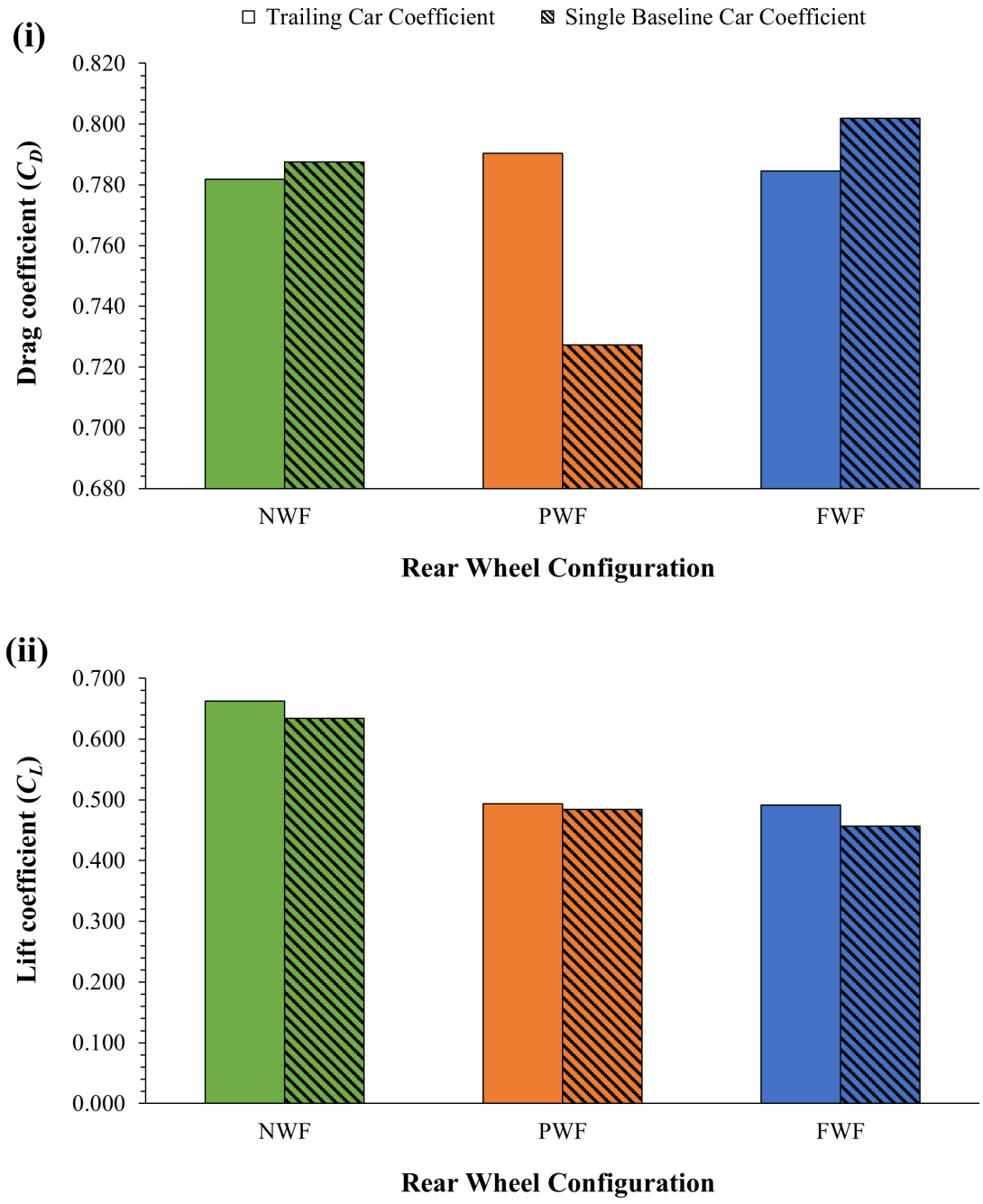


Figure 5.39: Comparison of (i) drag coefficients and (ii) lift coefficients for all configurations at trailing position D

Positions C and D correlate to the sides of a lead car. This is a region that a trailing car would be forced to operate in when attempting an overtaking manoeuvre. In comparison to the single baseline cars operating in undisturbed flow, the drag coefficients of a trailing car were seen to decrease for the no wheel fairing and full fairing configurations. In contrast, the drag coefficient of a trailing car with partial fairings increased above the single car baseline value. This was due to the spillage of air from the sidewalls of the wheels of a lead car with partial fairings. No such spillage occurred for a lead car with no fairings and the spillage was minimised by the sidewall cover of the full fairing configuration. This spillage of highly turbulent flow from the wheels moved to the side of the lead car thereby increasing the drag experienced by a trailing car positioned here. In comparison to the single baseline cars, the trailing cars for all configurations experienced a slight increase in lift coefficient. This contradicted the expected result of a decrease in lift coefficient for a trailing car positioned in the wake of a leading car. This was due to the simplification of the wings of the car models. Flow separation over these wings was more prominent than the wings of an actual Formula One car, leading to lower levels of downforce. This indicated that the single car baseline lift coefficients were not truly representative of an actual car with complex wing geometry. However, by comparing the lift coefficients between trailing cars of the various configurations at the same downstream positions, the most favourable rear wheel configuration could still be evaluated. The addition of partial and full wheel fairings increased the drag coefficients of a trailing car at both locations in this region in comparison to a trailing car with no wheel fairings at the same position. The partial fairings resulted in the largest increase. However, these changes in drag coefficient are small in this region (with a maximum change of 2.66%). The increase in drag coefficient was the result of the increased momentum loss caused by the addition of rear wheel fairings. This resulted in the larger rear wheel vortices that increased the drag of a trailing car. The normalised axial velocity of the vortex core to the side of a leading car was slightly higher for partial fairings, which resulted in a slightly higher drag coefficient here for a trailing car. The change in lift coefficients for a trailing car were significant with the addition of fairings. Both fairing configurations caused a reduction in lift coefficient in comparison to a trailing car with no fairings. The full fairings resulted in the largest decrease of 26.7%. These decreased lift coefficients, and thus reduced downforce experienced by a trailing car, was attributed to the creation of the higher intensity vortices to the sides of the rear wheels of a lead car. These vortices were intensified by the addition of fairings which resulted in higher turbulence in this region. The upwash component associated with the circulation of these vortices reduced the downforce generation by the front wing of a trailing car. This would thus cause increased understeer into corners by a trailing car. The previously made prediction (§5.1.7) of the drag coefficient of a trailing car decreasing to the side of a leading car was found to be incorrect as drag increased for both fairing configuration, although only slightly. This was because the vortices here were of low height and thus the majority of a trailing car positioned here would be exposed to freestream velocity axial flow

(including the rear wings). The previously made prediction of the lift coefficient of a trailing car with fairings decreasing in comparison to that of a trailing car with no fairings was found to be valid.

5.2.1 Summary of Aerodynamic Performance of Trailing Car

The fairings have thus shown to be ineffective in improving the aerodynamic conditions for a trailing car. This is because the fairings increased the turbulence of the wake structure, as well as having increased upwash components in critical areas, aft of a leading car. Both partial and full rear wheel fairings resulted in a trailing car experiencing higher drag when operating in the slipstream of a leading car. This would not allow for close following during racing conditions. To the sides of a lead vehicle, a trailing car experienced reduced downforce when fairings were implemented, which would result into significant understeer in to corners. If rear wheel fairings were applied to a full size car with complex wing geometry, the same changes in drag and lift coefficient would be expected, albeit not necessarily with the exact same magnitudes. This is because the qualitative flow structure would be similar for both the simplified car model and the more complex car model, as the overall aerodynamic shape of the cars is very similar. These factors would thus hinder overtaking opportunities and thus neither partial nor full fairings are recommended for implementation in Formula One racing as a means to increase overtaking.

Chapter 6

Conclusion

The aerodynamic wake behind a generic Formula One car was extensively examined. This was done for three different rear wheel configurations. A baseline configuration with no wheel fairings was initially tested. Thereafter, two distinct wheel fairings (partial and full) were evaluated and any differences in wake structure, in comparison to the baseline model, were investigated.

The method employed consisted of full size numerical car simulations for each rear wheel configuration. From these simulations, colour-flooded contours of normalised axial velocity along with two-dimensional planar streamtraces of the velocity components in the xy plane were created. These were created for three downstream distances behind a car. These downstream distances corresponded to a full car length, a half car length, and a plane immediately aft of the car. In addition, contours in the midplane of the car and rear wheel were also created. In addition, the drag and lift coefficients of a trailing car for each configuration, at various locations downstream of a leading car, were conducted. This was done to ascertain any changes in aerodynamic performance of a trailing car and evaluate if covering the rear wheels of a car could improve overtaking opportunities during races. Scale wind tunnel testing for each rear wheel configuration was conducted in order to validate the setup of the full size numerical model. The same two-dimensional velocity contours were extracted by wake surveys using a five-hole probe. These were compared to scale numerical simulations and were found to correlate closely to these results. This validated that the numerical model was set up correctly and could be applied appropriately to a full size car geometry. The flow structures found for these wake survey contours were confirmed through the use of tuft grid flow visualisation. The numerical models were verified by evaluating the wall $y+$ distribution, assessing sensitivity to the domain size, and performing mesh independence studies.

As per the objectives, the most significant findings of the research were as follows:

- The wake structure was altered by the addition of partial and full wheel fairings. These increased the size of the wheel vortices and the upwash flux in the wake of a car.

  At a distance immediately aft of the car, the addition of wheel fairings most significantly changed the wake structure aft and to the side of the rear wheels. The height of the low velocity region aft of the wheel was reduced by 103% and 143% for the partial and full fairing configurations respectively. The axial velocity above the ground to the side of the rear wheels was reduced by 4.17% and 13% for the partial and full fairing configuration respectively. The addition of both fairing configurations contributed significantly to an increase of vorticity and circulation aft of the car. The downwash velocity components aft of the wheel were increased most significantly by the full wheel fairings, with a maximum increase of 114%

  At a distance of half a characteristic length behind the car, the wheel fairings caused an increase in the size of the vortices to the sides of the rear wheels, with a reduction of axial velocity up to 4.83% and 11.3% at this location for the partial and full fairing configurations respectively. The centreline column of low velocity flow was reduced by up to 25.9% and 31.2% for the partial and full fairing configurations respectively. The addition of both fairings also raised this point higher up above the ground plane. The addition of partial fairings increased the upwash at the centreline and downwash magnitude at the wheel midplane by a maximum of 74.8% and 8.37% respectively. The full fairing configuration increased the upwash at the centreline and downwash magnitude at the wheel midplane by a maximum of 103% and 11.2% respectively.

  At a full characteristic length downstream of the car, the addition of wheel fairings eliminated a centreline column of low axial velocity flow. With both fairing configurations present, this low velocity region was localised to above the height of the rear wing of the car. The axial velocity of the vortex cores to the side of the wheel were lowest with full fairings attached. The upwash was increased by 29.9% and 48% respectively for the partial and full fairing configurations respectively at the car midplane. Both wheel fairing configurations reduced the downwash magnitude at the wheel midplane by 4.75%. The streamtraces showed an increase in upwash flux caused by the addition of both partial and full wheel fairings towards the midplane of the car.

  In planes through the car and wheel centrelines, the wheel fairings reduced the size of the low axial velocity regions. The fairings also altered the distance downstream at which the axial velocity had returned to at least half of the freestream velocity.

- In the wake of a leading car, the drag and lift experienced by a trailing car changed with the addition of wheel fairings. The drag and lift coefficients for a no wheel fairing configuration served as a baseline to evaluate the increase or decrease in these coefficients by the addition of partial and full wheel fairings. The addition of both fairings increased the drag and reduced the downforce of a trailing car, both in the slipstream and to the side of a leading car, at downstream distances of a half and full car length from the leading car.

  In the slipstream of the car, at a downstream distance of half a car length, the drag coefficient of a trailing car increased by 14.1% and 17.8% for the partial and full fairing configurations respectively. At this downstream distance, the lift coefficient of a trailing car decreased by 25.9% and 23.6% for the partial and full fairing configurations respectively. At a downstream distance of a full car length, the drag coefficient of a trailing car increased by 6.67% and 7.44% for the partial and full fairing configurations respectively. At this downstream distance, the lift coefficient of a trailing car decreased by 13.1% and 16.5% for the partial and full fairing configurations respectively.

  To the side of a leading car, at a downstream distance of half a car length, the drag coefficient of a trailing car increased by 2.67% and 0.92% for the partial and full fairing configurations respectively. At this downstream distance, the lift coefficient of a trailing car decreased by 23.8% and 26.7% for the partial and full fairing configurations respectively. At a downstream distance of a full car length, the drag coefficient of a trailing car increased by 1.09% and 0.35% for the partial and full fairing configurations respectively. At this downstream distance, the lift coefficient of a trailing car decreased by 25.5% and 25.8% for the partial and full fairing configurations respectively.

- Full wheel fairings were seen to have the most significant impact on the wake structure aft of the car. The full fairings most significantly reduced the size of the low axial velocity regions immediately aft of the car, but also lowered the axial velocity of the side wheel vortices most significantly. The full wheel fairings also resulted in the largest maximum downwash and upwash magnitudes at the car and wheel midplane in comparison to the no wheel fairing configuration. This would have significant impacts on the drag and downforce experienced by a trailing car, depending on where the trailing car is positioned downstream of the leading car.

  Full fairings increased the drag coefficient of a trailing car operating in a slipstream most significantly whereas partial fairings increased the drag coefficient most significantly for a trailing car positioned to the side of a leading car. Full wheel fairings decreased the lift coefficient most significantly at a full car length downstream in the slipstream and at half a car length to the side of a leading car. Partial wheel fairings decreased the lift coefficient most significantly at half a car length downstream in the slipstream and at a full car length to the side of a leading car.

The increase in drag and decrease in downforce for a trailing car operating in a leading car's wake would make it difficult to follow a leading car closely as well as losing downforce in corners resulting in a loss of control margins. Thus, this would not help improve overtaking opportunities during races.

6.1 Recommendations

It is recommended that neither partial or full rear wheel fairings be applied to Formula One cars in an attempt to improve the aerodynamics of a trailing car positioned in a leading car's wake. The addition of these fairings was found to have adverse effects for the performance of a trailing car and thus the traditional open-wheel configuration for the rear wheels should be kept. The findings from the presented research suggest a possible explanation as to why only front wheel fairings have been implemented for the 2022 Formula One season.

This research served as a starting point for the understanding of the aerodynamic effects of covering the rear wheels of a generic Formula One car. Further work is recommended to more comprehensively understand the effects of the addition of these fairings. This includes:

- Representing the complete geometry of the car, with no simplifications made to the downforce generating elements and the wheels. These simplified models served only as a baseline and the true effects cannot be concluded without applying the fairings to the exact geometry.
- The geometry of these fairings should be varied further, with more configurations and sizes tested. This would enable an optimised design of these fairings to be achieved which would enhance the aerodynamic conditions for a trailing car, while minimising any unwanted effects.
- The effects of a bumper bar attached to the rear wheels of a car should be investigated. While this may not result in any significant aerodynamic benefit or penalty, possible safety enhancements that prevent wheel contact between cars may be realised.
- Future research should utilise the new regulation cars for 2022, combining the rear wheel fairings with the already included partial front wheel fairings.
- Testing should be done at a variety of freestream velocities in order to correctly replicate the variation in speeds during a race.
- The boundary layers was seen to impact the wake structure close to the ground plane for the wind tunnel results. Wind tunnel tests should make use of more adequate boundary

layer removal devices, such that these effects are minimised. The use of a rolling road is recommended for future work as this includes the effects of wheel rotation.

- Higher quality wind tunnel models should be utilised as imperfectly constructed ones do not possess true consistency such as exact symmetry about the car midplane and an even surface finish at all locations along the car. These discrepancies can alter the results and need to be eliminated as full size Formula One cars are professionally and carefully constructed without such imperfections.

- More sophisticated wind tunnel measurement techniques, such as CTA, should be used in conjunction with five-hole probe testing. Wake surveys that utilise a finer grid spacing should also be employed. These techniques would allow for better spatial resolution, as well as temporal sensitivity in the results to be determined. In addition, more sophisticated flow visualisation techniques, such as LDA and PIV, should be used in favour of simple methods such as tuft or smoke visualisation.

- Wind tunnel tests should be conducted to ascertain the force distribution along a trailing car at various positions in order to validate the numerical results, and better understand the effects of fairings on the aerodynamic balance of a car.

- Numerical simulations should make use of a variety of the available RANS turbulence models available, along with modelling techniques such as Detached Eddy Simulation (DES). Unsteady simulations should be employed to correctly capture the time dependent flow features of the wake. A more comprehensive y^+ treatment should be included such that not only the log-law region is modelled. However, the implementation of these changes would be associated with a very high computational cost that may not be readily available.

- Numerical wake surveys should be conducted for both a leading and trailing car in close proximity in order to ascertain any qualitative differences in wake structure for each car caused by the presence/blockage effects of the other car.

- Numerical simulations should be performed that evaluate the changes in aerodynamic forces on a lead car due to the presence of a trailing car in close proximity.

References

[1] James, N. *Why the Return of Refuelling Would Be Bad for Formula 1*. 2016. URL: https://bit.ly/3ajeg1l. *(Last accessed: 16 September 2021)*.

[2] Scarborough, C. *F1: Why No Overtaking and Are Bigger Wings the Answer?* 2017. URL: https://bit.ly/3BnL6dy. *(Last accessed: 4 April 2021)*.

[3] Noble, J. *FIA unveils radical rear wing concept*. 2005. URL: https://bit.ly/3DCjL8f. *(Last accessed: 16 September 2021)*.

[4] van Wingerden, J. *F1 Explained: What is DRS? Why does it help overtaking?* 2018. URL: https://bit.ly/3BqN9gK. *(Last accessed: 16 September 2021)*.

[5] *Adjustable rear wing - Drag Reduction System (DRS)*. URL: https://bit.ly/3aiP5vM. *(Last accessed: 16 September 2021)*.

[6] Noble, J. *The key questions raised by Formula 1's 2021 car concepts*. 2018. URL: https://bit.ly/3ankVI1. *(Last accessed: 4 April 2021)*.

[7] Cooper, A. and Khorounzhiy, V. *2021 Formula 1 concept claimed to produce five-times less dirty air*. 2019. URL: https://bit.ly/3Aq2qwW. *(Last accessed: 4 April 2021)*.

[8] Stuart, G. *10 things you need to know about the all-new 2022 F1 car*. 2021. URL: https://f1.com/3FlSqbQ. *(Last accessed: 16 September 2021)*.

[9] Watts, M. and Watkins, S. 'Aerodynamic Structure and Development of Formula 1 Racing Car Wakes'. In: *SAE International Journal of Passenger Cars - Mechanical Systems* (2014). ISSN: 1946-4002. DOI: 10.4271/2014-01-0600.

[10] Newbon, J., Sims-Williams, D. and Dominy, R. 'Aerodynamic Analysis of Grand Prix Cars Operating in Wake Flows'. In: *SAE International Journal of Passenger Cars - Mechanical Systems* (2017). ISSN: 1946-4002. DOI: 10.4271/2017-01-1546.

[11] Knowles, R. D., Saddington, A. J. and Knowles, K. 'On the near wake of a Formula One front wheel'. In: *Proceedings of the Institution of Mechanical Engineers, Part D: Journal of Automobile Engineering* (2013). ISSN: 09544070. DOI: 10.1177/0954407013491903.

[12] Barnard, R. H. *Road Vehicle Aerodynamic Design*. 2nd ed. MechAero Publishing: Hertfordshire, 2001. ISBN: 0954073401.

[13] Dominy, R. G. 'The influence of slipstreaming on the performance of a Grand Prix racing car'. In: *Proceedings of the Institution of Mechanical Engineers. Part D, Transport engineering* (1990). ISSN: 02651904. DOI: 10.1243/pime_proc_1990_204_130_02.

[14] Džijan, I. et al. 'Aerodynamic characteristics of two slipstreaming race cars'. In: *Journal of Mechanical Science and Technology* (2021). ISSN: 19763824. DOI: 10.1007/s12206-020-1217-x.

[15] Rodrigues, R. *Ferrari SF71H*. 2018. URL: https://bit.ly/3mzInaB. *(Last accessed: 20 May 2020)*.

[16] Katz, J. *Race Car Aerodynamics: Designing for Speed*. 2nd ed. Bentley Publishers: Cambridge, MA, 2006. ISBN: 978037601427.

[17] Jenkins, M. 'Technological Discontinuities and Competitive Advantage: A Historical Perspective on Formula 1 Motor Racing 1950-2006'. In: *Journal of Management Studies* (2010). ISSN: 00222380. DOI: 10.1111/j.1467-6486.2010.00928.x.

[18] Wickern, G., Zwicker, K. and Pfadenhauer, M. 'Rotating wheels - Their impact on wind tunnel test techniques and on vehicle drag results'. In: *SAE Technical Papers*. 1997. DOI: 10.4271/970133.

[19] Cavusoglu, Ö. F. 'Aerodynamics Around Wheels and Wheelhouses'. Master's thesis in Applied Mechanics. Department of Applied Mechanics, Chalmers University of Technology, 2017.

[20] Wäschle, A. 'The Influence of Rotating Wheels on Vehicle Aerodynamics - Numerical and Experimental Investigations'. In: *SAE Technical Paper Series*. 2010. DOI: 10.4271/2007-01-0107.

[21] Bearman, P. W. et al. 'The effect of a moving floor on wind-tunnel simulation of road vehicles'. In: *SAE Technical Papers*. 1988. DOI: 10.4271/880245.

[22] Barlow, J. B., Rae, W. H. and Pope, A. *Low-Speed Wind Tunnel Testing*. 3rd ed. John Wiley and Sons, Inc.: Hoboken, NJ, 1999. ISBN: 0471557749.

[23] Sutherland, W. ' LII. The viscosity of gases and molecular force '. In: *The London, Edinburgh, and Dublin Philosophical Magazine and Journal of Science* (1893). ISSN: 1941-5982. DOI: 10.1080/14786449308620508.

[24] Potter, M. C., Wiggert, D. C. and Ramadan, B. H. *Mechanics of Fluids*. 5th ed. Cengage Learning: Boston, MA, 2015. ISBN: 9781305637610.

[25] Kim, J.-H. et al. 'Surface Flow and Wake Structure of a Rear View Mirror of the Passenger Car'. In: *BBAA VI International Colloquium on: Bluff Bodies Aerodynamics & Applications*. Milano, Italy: 20-24 July, 2008.

[26] Nakagawa, M. et al. 'Typical Velocity Fields and Vortical Structures around a Formula One Car, based on Experimental Investigations using Particle Image Velocimetry'. In: *SAE International Journal of Passenger Cars - Mechanical Systems* (2016). ISSN: 19464002. DOI: 10.4271/2016-01-1611.

[27] Ruchała, P. et al. 'Use and calibration of 5-hole pressure probes to measurement of airflow velocity'. In: *Journal of KONES* (2018). ISSN: 1231-4005. DOI: 10.5604/01.3001.0012.2850.

[28] Paul, A., Upadhyay, R. and Jain, A. 'A novel calibration algorithm for five-hole pressure probe'. In: *International Journal of Engineering, Science and Technology* (2011). ISSN: 2141-2820. DOI: 10.4314/ijest.v3i2.68136.

[29] Axon, L. 'The Aerodynamic Characteristics of Automobile Wheels - CFD Prediction and Wind Tunnel Experiment'. PhD Thesis. College of Aeronautics, Cranfield University, 1999.

[30] Lutz, T. and Sayers, A. 'Wind tunnel boundary layer effects on the aerodynamic drag of model trucks'. In: *R&D Journal* (1999).

[31] Stevenson, T. J. 'Simulation of Ground Vehicle Aerodynamics Applied to a Generic Le Mans Prototype'. Master of Science in Engineering. School of Mechanical, Industrial and Aeronautical Engineering. University of the Witwatersrand: Johannesburg, South Africa, 2012.

[32] Doig, G. 'Compressible Ground Effect Aerodynamics'. PhD thesis. University of New South Wales: Sydney, Australia, 2009.

[33] Cooper, K. R. et al. 'The aerodynamic performance of automotive underbody diffusers'. In: *SAE Technical Papers*. 1998. DOI: 10.4271/980030.

[34] Pagliarella, R. M. 'On the Aerodynamic Performance of Automotive Vehicle Platoons Featuring Pre and Post-Critical Leading Forms'. Doctor of Philosophy Thesis. School of Aerospace, Mechanical and Manufacturing Engineering, RMIT University, 2009.

[35] Ahmed, S. R., Ramm, G. and Faltin, G. 'Some salient features of the time-averaged ground vehicle wake'. In: *SAE Technical Papers*. 1984. DOI: 10.4271/840300.

[36] Cogotti, A. 'Evolution of performance of an automotive wind tunnel'. In: *Journal of Wind Engineering and Industrial Aerodynamics* (2008). ISSN: 01676105. DOI: 10.1016/j.jweia.2007.06.007.

[37] Hennig, A. et al. 'Numerical comparison of rolling road systems'. In: *SAE International Journal of Engines* (2011). ISSN: 19463936. DOI: 10.4271/2011-37-0017.

[38] Axon, L., Garry, K. and Howell, J. 'An evaluation of cfd for modelling the flow around stationary and rotating isolated wheels'. In: *SAE Technical Papers*. 1998. DOI: 10.4271/980032.

[39] McBeath, S. *Competition Car Aerodynamics*. 3rd ed. Veloce Publishing Limited: Dorchester, 2017. ISBN: 9781787111028.

[40] Bird, J. D. 'Tuft-Grid Surveys at Low Speeds for Delta Wings'. In: *NASA Technical Note* (1969).

[41] Mercker, E. 'A blockage correction for automotive testing in a wind tunnel with closed test section'. In: *Journal of Wind Engineering and Industrial Aerodynamics* (1986). ISSN: 01676105. DOI: 10.1016/0167-6105(86)90080-2.

[42] Lock, C. N. H. *The Interference of a Wind Tunnel on a Symmetrical Body*. Aeronautical Research Council. Reports and Memoranda No. 1275, 1929.

[43] Cooper, K. 'Bluff-body Blockage Corrections in Closed- and Open-Test-Section Wind Tunnels'. In: *Agard Ag-336* (1998).

[44] Young, A. D. and Squire, H. B. *Blockage Corrections in a Closed Rectangular Tunnel*. Aeronautical Research Council. Reports and Memoranda No. 1984, 1945.

[45] Maskell, E. C. *A Theory of the Blockage Effects on Bluff Bodies and Stalled Wings in a Closed Wind Tunnel*. Aeronautical Research Council. Reports and Memoranda No. 3400, 1963.

[46] Bayındırlı, C., Akansu, Y. E. and Salman, M. S. 'The Determination Of Aerodynamic Drag Coefficient Of Truck and Trailer Model By Wind Tunnel Tests'. In: *International Journal of Automotive Engineering and Technologies* (2016). DOI: 10.18245/ijaet.11754.

[47] Siemens. *Simcenter STAR-CCM+ User Guide*. 2019. URL: https://sie.ag/3lpPyD3. *(Last accessed: 10 September 2019)*.

[48] Krastev, V. K. and Bella, G. 'On the steady and unsteady turbulence modeling in ground vehicle aerodynamic design and optimization'. In: *SAE Technical Papers*. 2011. DOI: 10.4271/2011-24-0163.

[49] Reynolds, O. 'IV. On the dynamical theory of incompressible viscous fluids and the determination of the criterion'. In: *Philosophical Transactions of the Royal Society of London. (A.)* (1895). ISSN: 0264-3820. DOI: 10.1098/rsta.1895.0004.

[50] Wilcox, D. C. *Turbulence Modelling for CFD*. 2nd ed. DCW Industries: La Canada, CA, 1998. ISBN: 192872910X.

[51] Versteeg, H. K. and Malalasekera, W. *An Introduction to Computational Fluid Dynamics: The Finite Volume Method*. 2nd ed. Pearson Education Limited: Harlow, 2007. ISBN: 978-0-13-127498-3.

[52] Igali, D. et al. 'Comparative Analysis of Turbulence Models for Automotive Aerodynamic Simulation and Design'. In: *International Journal of Automotive Technology* (2019). ISSN: 19763832. DOI: 10.1007/s12239-019-0107-7.

[53] Schlichting, H. and Gersten, K. *Boundary-Layer Theory*. 9th ed. Springer: Berlin, 2000. ISBN: 9783662529195. DOI: 10.1007/978-3-662-52919-5.

[54] Roache, P. J. *Verification and Validation in Computational Science and Engineering*. Hermosa Publishers: Albuquerque, NM, 1998. ISBN: 0913478083.

[55] Davkin, L. and Law, C. 'Aerodynamic Effect of Wheel Fairings on the Wake of a Formula One Car'. In: *MATEC Web of Conferences* 347 (2021), p. 00008. DOI: 10.1051/matecconf/202134700008.

[56] Siemens. *Best Practices for Vehicle Aerodynamics*. 2021. URL: https://sie.ag/3CrHszs. *(Last accessed: 19 September 2021)*.

[57] Evans, S., Lardeau, S. and Pettinelli, C. 'Validation of a turbulence methodology using the SST k-ω model for adjoint calculation'. In: *54th AIAA Aerospace Sciences Meeting*. 2016. ISBN: 9781624103933. DOI: 10.2514/6.2016-0585.

[58] Cobb, H. *The fastest F1 tracks on the calendar*. 2020. URL: https://bit.ly/3lHA5gf. *(Last accessed: 5 May 2020)*.

[59] Celik, I. B. et al. 'Procedure for estimation and reporting of uncertainty due to discretization in CFD applications'. In: *Journal of Fluids Engineering, Transactions of the ASME* 130.7 (2008), pp. 0780011–0780014. ISSN: 00982202. DOI: 10.1115/1.2960953.

[60] Atherfold, J. 'Flow Over a Dakar Car'. Bachelor of Science in Engineering. School of Mechanical, Industrial and Aeronautical Engineering. University of the Witwatersrand: Johannesburg, South Africa, 2016.

[61] Cooper, K. R. 'The wind-tunnel simulation of surface vehicles'. In: *Journal of Wind Engineering and Industrial Aerodynamics* (1984). ISSN: 01676105. DOI: 10.1016/0167-6105(84)90055-2.

[62] Town, J. and Camci, C. 'Sub-miniature five-hole probe calibration using a time efficient pitch and yaw mechanism and accuracy improvements'. In: *Proceedings of the ASME Turbo Expo*. 2011. ISBN: 9780791854631. DOI: 10.1115/GT2011-46391.

[63] *Fluke 922 Airflow Meter Users Manual*. PN 2683880. Rev.1, 12/07. Fluke Corporation: Taiwan, 2006.

[64] Holman, J. P. *Experimental methods for engineers*. 8th ed. McGraw-Hill: New York, NY., 2012.

[65] Mo, Q. et al. 'Guidelines for the computational domain size on an urban-scale VAWT'. In: *Journal of Physics: Conference Series*. 2021. DOI: 10.1088/1742-6596/1820/1/012177.

Appendix A

Wind Tunnel Wake Survey Additional Figures

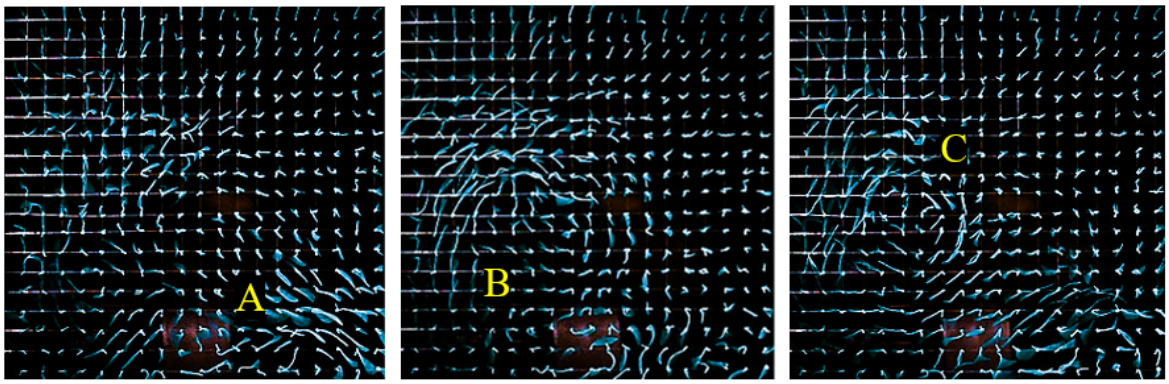


Figure A.1: Flow visualisation for partial wheel fairings at $z = 0.5L$

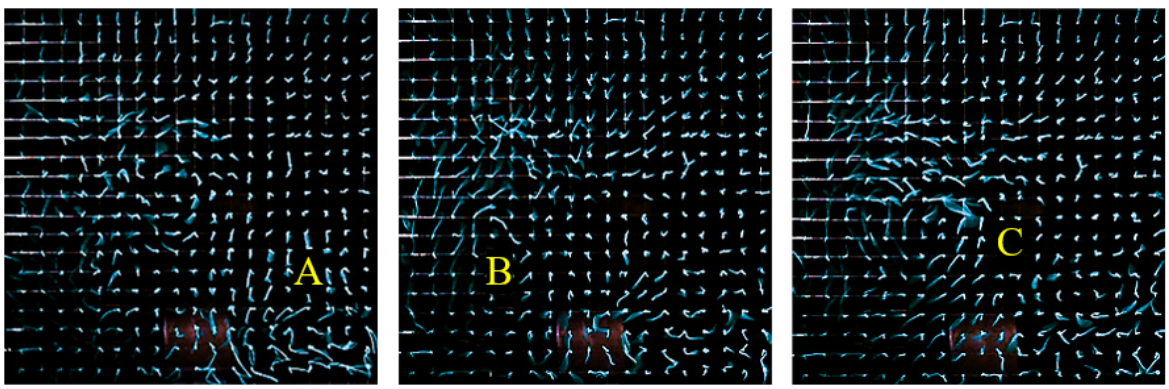


Figure A.2: Flow visualisation for full wheel fairings at $z = 0.5L$

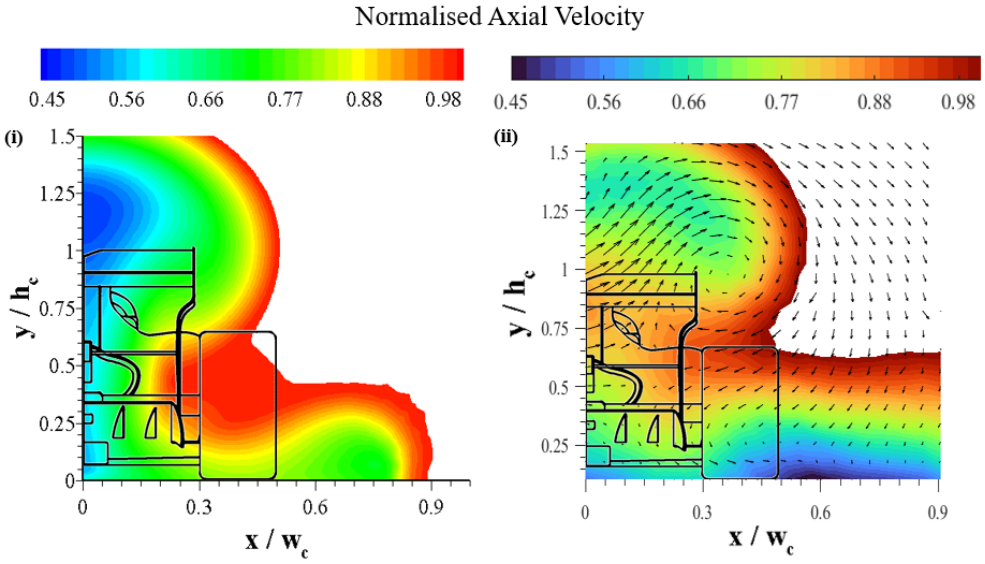


Figure A.3: Scale model normalised axial velocity contours for no wheel fairings at $z = 1.0L$ for CFD (i) and wind tunnel (ii) tests

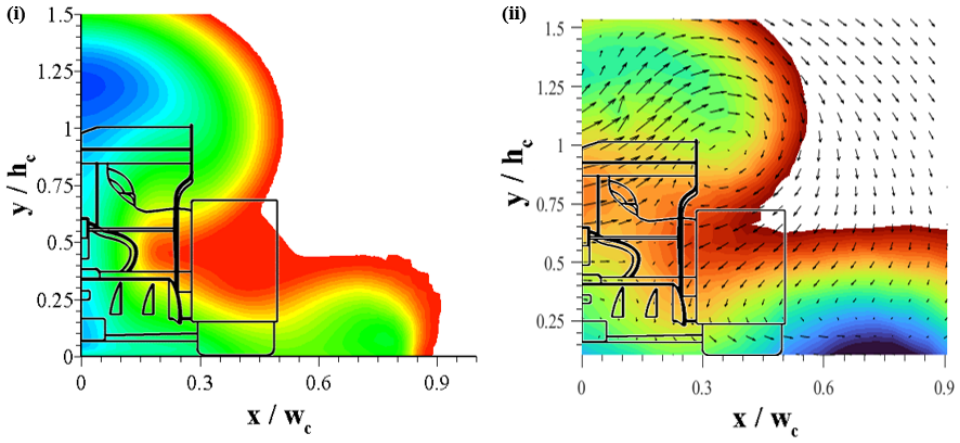


Figure A.4: Scale model normalised axial velocity contours for partial wheel fairings at $z = 1.0L$ for CFD (i) and wind tunnel (ii) tests

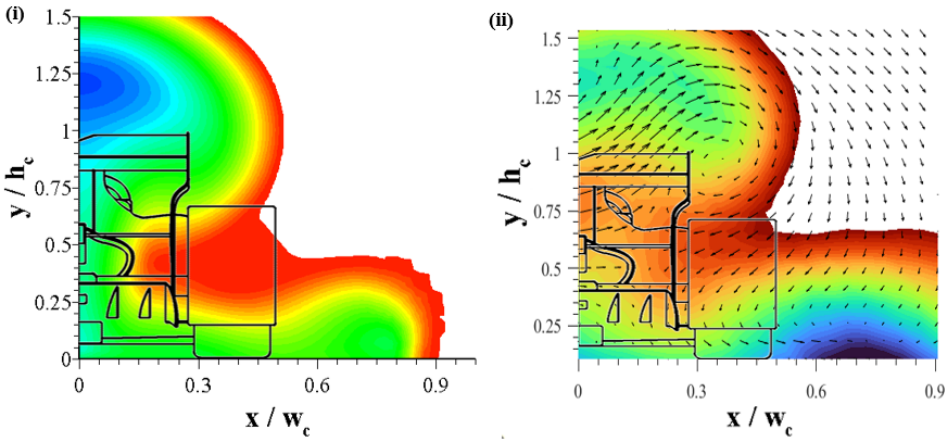


Figure A.5: Scale model normalised axial velocity contours for full wheel fairings at $z = 1.0L$ for CFD (i) and wind tunnel (ii) tests

Appendix B

Wind Tunnel Measurement Uncertainty

The following uncertainty analysis pertains to the error propagation for the obtaining and data processing related to the wind tunnel wake surveys. The uncertainty of the air density value was calculated using the smallest increments of the measurement devices for temperature, atmospheric pressure and relative humidity, along with the uncertainty in the calculated value for the saturation vapour pressure of air.

$$\delta\rho_a = \sqrt{\left(\frac{\partial\rho_a}{\partial T}\delta T\right)^2 + \left(\frac{\partial\rho_a}{\partial P}\delta P\right)^2 + \left(\frac{\partial\rho_a}{\partial R_H}\delta R_H\right)^2 + \left(\frac{\partial\rho_a}{\partial e_s}\delta e_s\right)^2} \tag{B.1}$$

The uncertainty in the calculated value for the saturation vapour pressure of air is as follows:

$$\delta e_s = \sqrt{\left(\frac{\partial e_s}{\partial T}\delta T\right)^2} \tag{B.2}$$

The uncertainty associated with the total pressure coefficient is given by:

$$\delta C_{P_{total}} = \sqrt{\sum_{i=1}^{5}\left(\frac{\partial C_{P_{total}}}{\partial P_i}\delta P_i\right)^2 + \left(\frac{\partial C_{P_{total}}}{\partial P_{total}}\delta P_{total}\right)^2} \tag{B.3}$$

Similarly, the uncertainty associated with the static pressure coefficient is given by:

$$\delta C_{P_{static}} = \sqrt{\sum_{i=1}^{5}\left(\frac{\partial C_{P_{static}}}{\partial P_i}\delta P_i\right)^2 + \left(\frac{\partial C_{P_{static}}}{\partial P_{static}}\delta P_{static}\right)^2} \tag{B.4}$$

The uncertainty in total pressure is given as:

$$\delta P_{total} = \sqrt{\sum_{i=1}^{5} \left(\frac{\partial P_{total}}{\partial P_i} \delta P_i \right)^2 + \left(\frac{\partial P_{total}}{\partial C_{P_{total}}} \delta C_{P_{total}} \right)^2} \tag{B.5}$$

Similarly, the uncertainty in static pressure is given as:

$$\delta P_{static} = \sqrt{\sum_{i=1}^{5} \left(\frac{\partial P_{static}}{\partial P_i} \delta P_i \right)^2 + \left(\frac{\partial P_{static}}{\partial C_{P_{static}}} \delta C_{P_{static}} \right)^2} \tag{B.6}$$

The uncertainty associated with the velocity magnitude was as follows:

$$\delta V = \sqrt{\left(\frac{\partial V}{\partial P_{total}} \delta P_{total} \right)^2 + \left(\frac{\partial V}{\partial P_{static}} \delta P_{static} \right)^2 + \left(\frac{\partial V}{\partial \rho_a} \delta \rho_a \right)^2} \tag{B.7}$$

Assuming the uncertainty to be equal to the smallest resolution of the utilised digital inclinometer, the uncertainties in the three-dimensional velocity components was found as follows:

$$\delta u = \sqrt{\left(\frac{\partial u}{\partial V} \delta V \right)^2 + \left(\frac{\partial u}{\partial \alpha} \delta \alpha \right)^2} \tag{B.8}$$

$$\delta w = \sqrt{\left(\frac{\partial v}{\partial V} \delta V \right)^2 + \left(\frac{\partial v}{\partial \alpha} \delta \alpha \right)^2 + \left(\frac{\partial v}{\partial \beta} \delta \beta \right)^2} \tag{B.9}$$

$$\delta v = \sqrt{\left(\frac{\partial w}{\partial V} \delta V \right)^2 + \left(\frac{\partial w}{\partial \alpha} \delta \alpha \right)^2 + \left(\frac{\partial w}{\partial \beta} \delta \beta \right)^2} \tag{B.10}$$

The percentage uncertainties in u, v and w are then found by dividing by the magnitude of these components.

Appendix C

MATLAB Function for Wind Tunnel Wake Survey Data Processing

The MATLAB Function presented on the subsequent pages was used to create the colour-flooded plots/contours for the scale wind tunnel wake survey. This function used calibration data to determine the three-dimensional velocity components at each probing location, and then create the contours according to the previously defined grid (§3.5.1, Figure 3.18) the resultant figures consisted of normalised axial velocity components (w), with arrows representing the planar velocity components (u and v).

```
function [] = TestColourContours(Configuration,Distance)
close all
warning('off','all');
clc
ExcelFile = strcat(Configuration,'-');
ExcelFile = strcat(ExcelFile,Distance);
ExcelFile = strcat(ExcelFile,'L.xlsx');
AirConditionsMatrix = readtable(ExcelFile,'Sheet','Average Air Conditions');
Density = table2array(AirConditionsMatrix(1,2));
Viscosity = table2array(AirConditionsMatrix(2,2));
Speed = table2array(AirConditionsMatrix(3,2));
DataMatrix = readtable('ProbeCalibration.xlsx');
DataMatrix = DataMatrix(1:343,1:28);
PotentiometerSettingMatrix = DataMatrix(1:343,7);
YawAngleMatrix = DataMatrix(1:343,8);
PitchAngleMatrix = DataMatrix(1:343,9);
PitotVelocityMatrix = DataMatrix(1:343,20);
CpYawMatrix = DataMatrix(1:343,25);
CpPitchMatrix = DataMatrix(1:343,26);
CpTotalMatrix = DataMatrix(1:343,27);
CpStaticMatrix = DataMatrix(1:343,28);
PlottingDataMatrix =
[YawAngleMatrix,PitchAngleMatrix,PotentiometerSettingMatrix,PitotVelocityMatr
ix,CpYawMatrix,CpPitchMatrix,CpTotalMatrix,CpStaticMatrix];
Length = size(PlottingDataMatrix);
NumberOfRows = Length(1);
CpYawAndCpPitchMatrix = [];
CpYawAndCpPitchMatrixCount = 1;
CalibrationAngles00Yaw = [00 0; 00 10; 00 20; 00 30; 00 -10; 00 -20; 00 -30];
CalibrationAngles10Yaw = [10 0; 10 10; 10 20; 10 30; 10 -10; 10 -20; 10 -30];
CalibrationAngles20Yaw = [20 0; 20 10; 20 20; 20 30; 20 -10; 20 -20; 20 -30];
CalibrationAngles30Yaw = [30 0; 30 10; 30 20; 30 30; 30 -10; 30 -20; 30 -30];
CalibrationAnglesMinus10Yaw = [-10 0; -10 10; -10 20; -10 30; -10 -10; -10 -
20; -10 -30];
CalibrationAnglesMinus20Yaw = [-20 0; -20 10; -20 20; -20 30; -20 -10; -20 -
20; -20 -30];
CalibrationAnglesMinus30Yaw = [-30 0; -30 10; -30 20; -30 30; -30 -10; -30 -
20; -30 -30];
AllCalibrationAngles =
[CalibrationAngles00Yaw;CalibrationAngles10Yaw;CalibrationAngles20Yaw;Calibra
tionAngles30Yaw;CalibrationAnglesMinus10Yaw;CalibrationAnglesMinus20Yaw;Calib
rationAnglesMinus30Yaw];
for count = 1:7:NumberOfRows-6
    X = PlottingDataMatrix{count:count+6,5};
    Y = PlottingDataMatrix{count:count+6,6};
    Z = PlottingDataMatrix{count:count+6,4};
    YawBestFitLineCoefficients = polyfit(Z,X,3);
    xFitYaw = linspace(min(Z), max(Z), 1000);
    yFitYaw = polyval(YawBestFitLineCoefficients , xFitYaw);
    CpYawAndCpPitchMatrix(CpYawAndCpPitchMatrixCount,1) =
polyval(YawBestFitLineCoefficients,Speed);
    PitchBestFitLineCoefficients = polyfit(Z,Y,3);
    xFitPitch = linspace(min(Z), max(Z), 1000);
    yFitPitch = polyval(PitchBestFitLineCoefficients , xFitPitch);
    CpYawAndCpPitchMatrix(CpYawAndCpPitchMatrixCount,2) =
polyval(PitchBestFitLineCoefficients,Speed);
    CpYawAndCpPitchMatrixCount = CpYawAndCpPitchMatrixCount + 1;
```

```
end
CpValuesWithAngles = [AllCalibrationAngles, CpYawAndCpPitchMatrix];
Yaw = CpYawAndCpPitchMatrix(:,1);
Pitch = CpYawAndCpPitchMatrix(:,2);
scatter(Yaw,Pitch,10,'filled','black');
xlabel('Cp Yaw');
ylabel('Cp Pitch');
grid on;
grid minor;
yline(0);
xline(0);
hold on
xlim([-10 10])
ylim([-10 10])
ConstantYawEquations = [];
for count = 1:7:49
    ConstantYaw = CpValuesWithAngles(count:count+6,:);
    B = ConstantYaw(:,3);
    A = ConstantYaw(:,4);
    Plotting = polyfit(A,B,2);
    ConstantYawEquations = [ConstantYawEquations; Plotting];
    AFit = min(A):0.1:max(A);
    BFit = polyval(Plotting , AFit);
    plot(BFit,AFit);
    AngleNumber = ConstantYaw(1,1);
    AngleString = num2str(AngleNumber);
    Label = text(ConstantYaw(4,3),ConstantYaw(4,4)+0.5,strcat('Yaw = ',{'
'},AngleString));
    set(Label,'Rotation',60);
end
ConstantPitchEquations = [];
for count = -30:10:30
    ConstantPitch = [];
    ConstantPitchCount = 1;
    for SecondCount = 1:1:49
        if CpValuesWithAngles(SecondCount,2) == count
            ConstantPitch(ConstantPitchCount,:) =
CpValuesWithAngles(SecondCount,2:4);
            ConstantPitchCount = ConstantPitchCount + 1;
        end
    end
    B = ConstantPitch(:,2);
    A = ConstantPitch(:,3);
    Plotting = polyfit(B,A,2);
    ConstantPitchEquations = [ConstantPitchEquations; Plotting];
    AFit = min(B):0.1:max(B);
    BFit = polyval(Plotting , AFit);
    plot(AFit,BFit);
    AngleNumber = ConstantPitch(1,1);
    AngleString = num2str(AngleNumber);
    Label = text(ConstantPitch(7,2)+0.5,ConstantPitch(7,3),strcat('Pitch = ',
{' '},AngleString));
    set(Label,'Rotation',0);
end
YawAngleFit = -30:0.1:30;
YawAngles = [0; 10; 20; 30; -10; -20; -30];
ConstantYawEquations = [YawAngles ConstantYawEquations];
```

```
ALineOfBestFit =
polyfit(ConstantYawEquations(:,1),ConstantYawEquations(:,2),2);
BLineOfBestFit =
polyfit(ConstantYawEquations(:,1),ConstantYawEquations(:,3),2);
CLineOfBestFit =
polyfit(ConstantYawEquations(:,1),ConstantYawEquations(:,4),2);
YawExtrapolationFit = -15:0.1:15;
YawAnglesToExtrapolate = [-60; -50; -40; 40; 50; 60];
YawAnglesExtrapolationMatrix = [];
for count = 1:1:length(YawAnglesToExtrapolate)
    YawAnglesExtractA =
polyval(ALineOfBestFit,YawAnglesToExtrapolate(count));
    YawAnglesExtractB =
polyval(BLineOfBestFit,YawAnglesToExtrapolate(count));
    YawAnglesExtractC =
polyval(CLineOfBestFit,YawAnglesToExtrapolate(count));
    YawAnglesExtractCoeff = [YawAnglesExtractA, YawAnglesExtractB,
YawAnglesExtractC];
    YawAnglesExtrapolationMatrix = [YawAnglesExtrapolationMatrix;
YawAnglesExtractCoeff];
    plot(polyval(YawAnglesExtractCoeff,YawExtrapolationFit),
YawExtrapolationFit);
end
YawAnglesExtrapolationMatrix = [YawAnglesToExtrapolate
YawAnglesExtrapolationMatrix];
ConstantYawEquations = [ConstantYawEquations; YawAnglesExtrapolationMatrix];
PitchAngles = [-30; -20; -10; 0; 10; 20; 30];
ConstantPitchEquations = [PitchAngles ConstantPitchEquations];
PitchAngleFit = -30:0.1:30;
ALineOfBestFit =
polyfit(ConstantPitchEquations(:,1),ConstantPitchEquations(:,2),2);
BLineOfBestFit =
polyfit(ConstantPitchEquations(:,1),ConstantPitchEquations(:,3),2);
CLineOfBestFit =
polyfit(ConstantPitchEquations(:,1),ConstantPitchEquations(:,4),2);
PitchExtrapolationFit = -15:0.1:15;
PitchAnglesToExtrapolate = [-60; -50; -40; 40; 50; 60];
PitchAnglesExtrapolationMatrix = [];
for count = 1:1:length(PitchAnglesToExtrapolate)
    PitchAnglesExtractA =
polyval(ALineOfBestFit,PitchAnglesToExtrapolate(count));
    PitchAnglesExtractB =
polyval(BLineOfBestFit,PitchAnglesToExtrapolate(count));
    PitchAnglesExtractC =
polyval(CLineOfBestFit,PitchAnglesToExtrapolate(count));
    PitchAnglesExtractCoeff = [PitchAnglesExtractA, PitchAnglesExtractB,
PitchAnglesExtractC];
    PitchAnglesExtrapolationMatrix = [PitchAnglesExtrapolationMatrix;
PitchAnglesExtractCoeff];
    plot(PitchExtrapolationFit,
polyval(PitchAnglesExtractCoeff,PitchExtrapolationFit));
end
PitchAnglesExtrapolationMatrix = [PitchAnglesToExtrapolate
PitchAnglesExtrapolationMatrix];
ConstantPitchEquations = [ConstantPitchEquations;
PitchAnglesExtrapolationMatrix];
CpTotalAndCpStaticMatrix = [];
```

```
CpTotalAndCpStaticMatrixCount = 1;
for count = 1:7:NumberOfRows-6
    X = PlottingDataMatrix{count:count+6,7};
    Y = PlottingDataMatrix{count:count+6,8};
    Z = PlottingDataMatrix{count:count+6,4};
    CpTotalBestFitLineCoefficients = polyfit(Z,X,3);
    xFitCpTotal = linspace(min(Z), max(Z), 1000);
    yFitCpTotal = polyval(CpTotalBestFitLineCoefficients , xFitCpTotal);
    CpTotalAndCpStaticMatrix(CpTotalAndCpStaticMatrixCount,1) =
polyval(CpTotalBestFitLineCoefficients,Speed);
    CpStaticBestFitLineCoefficients = polyfit(Z,Y,3);
    xFitCpStatic = linspace(min(Z), max(Z), 1000);
    yFitCpStatic = polyval(CpStaticBestFitLineCoefficients , xFitCpStatic);
    CpTotalAndCpStaticMatrix(CpTotalAndCpStaticMatrixCount,2) =
polyval(CpStaticBestFitLineCoefficients,Speed);
    CpTotalAndCpStaticMatrixCount = CpTotalAndCpStaticMatrixCount + 1;
end
CpTotalAndCpStaticValuesWithAngles = [AllCalibrationAngles,
CpTotalAndCpStaticMatrix];
CpTotal = CpTotalAndCpStaticMatrix(:,1);
CpStatic = CpTotalAndCpStaticMatrix(:,2);
figure(2)
xlabel('Pitch Angle');
ylabel('Cp Total');
grid on;
grid minor;
yline(0);
xline(0);
hold on
xlim([-30 30])
ylim([-4 0.1])
CpTotalConstantYawEquationMatrix = [];
for count = 1:7:length(CpTotalAndCpStaticValuesWithAngles)
    CpTotalConstantYawBestFitLine = -60:0.1:60;
    hold on
    CpTotalConstantYawBestFitLineCoeff =
polyfit(CpTotalAndCpStaticValuesWithAngles(count:count+6,2),CpTotalAndCpStati
cValuesWithAngles(count:count+6,3),2);
    CpTotalConstantYawEquationMatrix = [CpTotalConstantYawEquationMatrix;
CpTotalConstantYawBestFitLineCoeff];
    CpTotalConstantYawBestFitLinePlot =
polyval(CpTotalConstantYawBestFitLineCoeff,CpTotalConstantYawBestFitLine);
    plot(CpTotalConstantYawBestFitLine, CpTotalConstantYawBestFitLinePlot);
    hold on
    AngleNumber = CpTotalAndCpStaticValuesWithAngles(count,1);
    AngleString = num2str(AngleNumber);
    Label = text(0,polyval(CpTotalConstantYawBestFitLineCoeff,0) -
0.02,strcat('Yaw =  ', {' '}, AngleString));
    set(Label,'Rotation',0);
    hold on
end
figure(3)
xlabel('Pitch Angle');
ylabel('Cp Static');
grid on;
grid minor;
yline(0);
```

```
xline(0);
hold on
xlim([-30 30])
ylim([-0.5 1])
CpStaticConstantYawEquationMatrix = [];
for count = 1:7:length(CpTotalAndCpStaticValuesWithAngles)
    CpStaticConstantYawBestFitLine = -60:0.1:60;
    hold on
    CpStaticConstantYawBestFitLineCoeff =
polyfit(CpTotalAndCpStaticValuesWithAngles(count:count+6,2),CpTotalAndCpStati
cValuesWithAngles(count:count+6,4),2);
    CpStaticConstantYawEquationMatrix = [CpStaticConstantYawEquationMatrix;
CpStaticConstantYawBestFitLineCoeff];
    CpStaticConstantYawBestFitLinePlot =
polyval(CpStaticConstantYawBestFitLineCoeff,CpStaticConstantYawBestFitLine);
    plot(CpStaticConstantYawBestFitLine, CpStaticConstantYawBestFitLinePlot);
    hold on
    AngleNumber = CpTotalAndCpStaticValuesWithAngles(count,1);
    AngleString = num2str(AngleNumber);
    Label = text(0,polyval(CpStaticConstantYawBestFitLineCoeff,0) -
0.02,strcat('Yaw =  ',{' '},AngleString));
    set(Label,'Rotation',0);
end
AnotherYawAngleMatrix = [0; 10; 20; 30; -10; -20;-30];
CpTotalConstantYawEquationMatrixWithAngles = [AnotherYawAngleMatrix,
CpTotalConstantYawEquationMatrix];
CpTotalBestFitLineA =
polyfit(CpTotalConstantYawEquationMatrixWithAngles(:,1),CpTotalConstantYawEqu
ationMatrixWithAngles(:,2),2);
CpTotalBestFitLineB =
polyfit(CpTotalConstantYawEquationMatrixWithAngles(:,1),CpTotalConstantYawEqu
ationMatrixWithAngles(:,3),2);
CpTotalBestFitLineC =
polyfit(CpTotalConstantYawEquationMatrixWithAngles(:,1),CpTotalConstantYawEqu
ationMatrixWithAngles(:,4),2);
CpStaticConstantYawEquationMatrixWithAngles = [AnotherYawAngleMatrix,
CpStaticConstantYawEquationMatrix];
CpStaticBestFitLineA =
polyfit(CpStaticConstantYawEquationMatrixWithAngles(:,1),CpStaticConstantYawE
quationMatrixWithAngles(:,2),2);
CpStaticBestFitLineB =
polyfit(CpStaticConstantYawEquationMatrixWithAngles(:,1),CpStaticConstantYawE
quationMatrixWithAngles(:,3),2);
CpStaticBestFitLineC =
polyfit(CpStaticConstantYawEquationMatrixWithAngles(:,1),CpStaticConstantYawE
quationMatrixWithAngles(:,4),2);
DataMatrixOne = readtable(ExcelFile,'Sheet','1st Movement');
XCoordMatrixOne = DataMatrixOne(1:105,17);
ZCoordMatrixOne = DataMatrixOne(1:105,18);
CpYawMatrixOne = DataMatrixOne(1:105,19);
CpPitchMatrixOne = DataMatrixOne(1:105,20);
TotalPressureMatrixOne = DataMatrixOne(1:105,23);
StaticPressureMatrixOne = DataMatrixOne(1:105,24);
AveragePressureMatrixOne = DataMatrixOne(1:105,25);
DataMatrixTwo = readtable(ExcelFile,'Sheet','2nd Movement');
XCoordMatrixTwo = DataMatrixTwo(1:105,17);
ZCoordMatrixTwo = DataMatrixTwo(1:105,18);
```

```
CpYawMatrixTwo = DataMatrixTwo(1:105,19);
CpPitchMatrixTwo = DataMatrixTwo(1:105,20);
TotalPressureMatrixTwo = DataMatrixTwo(1:105,23);
StaticPressureMatrixTwo = DataMatrixTwo(1:105,24);
AveragePressureMatrixTwo = DataMatrixTwo(1:105,25);
DataMatrixThree = readtable(ExcelFile,'Sheet','3rd Movement');
XCoordMatrixThree = DataMatrixThree(1:105,17);
ZCoordMatrixThree = DataMatrixThree(1:105,18);
CpYawMatrixThree = DataMatrixThree(1:105,19);
CpPitchMatrixThree = DataMatrixThree(1:105,20);
TotalPressureMatrixThree = DataMatrixThree(1:105,23);
StaticPressureMatrixThree = DataMatrixThree(1:105,24);
AveragePressureMatrixThree = DataMatrixThree(1:105,25);
DataMatrixFour = readtable(ExcelFile,'Sheet','4th Movement');
XCoordMatrixFour = DataMatrixFour(1:84,17);
ZCoordMatrixFour = DataMatrixFour(1:84,18);
CpYawMatrixFour = DataMatrixFour(1:84,19);
CpPitchMatrixFour = DataMatrixFour(1:84,20);
TotalPressureMatrixFour = DataMatrixFour(1:84,23);
StaticPressureMatrixFour = DataMatrixFour(1:84,24);
AveragePressureMatrixFour = DataMatrixFour(1:84,25);
FullMatrixOne =
[XCoordMatrixOne,ZCoordMatrixOne,CpYawMatrixOne,CpPitchMatrixOne,TotalPressur
eMatrixOne,StaticPressureMatrixOne,AveragePressureMatrixOne];
FullMatrixOne = table2array(FullMatrixOne);
FullMatrixTwo =
[XCoordMatrixTwo,ZCoordMatrixTwo,CpYawMatrixTwo,CpPitchMatrixTwo,TotalPressur
eMatrixTwo,StaticPressureMatrixTwo,AveragePressureMatrixTwo];
FullMatrixTwo = table2array(FullMatrixTwo);
FullMatrixThree =
[XCoordMatrixThree,ZCoordMatrixThree,CpYawMatrixThree,CpPitchMatrixThree,Tota
lPressureMatrixThree,StaticPressureMatrixThree,AveragePressureMatrixThree];
FullMatrixThree = table2array(FullMatrixThree);
FullMatrixFour =
[XCoordMatrixFour,ZCoordMatrixFour,CpYawMatrixFour,CpPitchMatrixFour,TotalPre
ssureMatrixFour,StaticPressureMatrixFour,AveragePressureMatrixFour];
FullMatrixFour = table2array(FullMatrixFour);
FullMatrix = [FullMatrixOne;FullMatrixTwo;FullMatrixThree;FullMatrixFour];
YawAngleValues = [];
PitchAngleValues = [];
CpPitchValueMatrixWithAngles = [];
Angles = [];
for count = 1:1:length(FullMatrix)
    InputCpYawValue = FullMatrix(count,3);
    CpPitchValueMatrix = [];
    for secondcount =1:1:length(ConstantPitchEquations)
        CorrespondingCpPitchValue =
polyval(ConstantPitchEquations(secondcount,2:4),InputCpYawValue);
        CpPitchValueMatrix = [CpPitchValueMatrix;
ConstantPitchEquations(secondcount,1), CorrespondingCpPitchValue];
    end
    hold on
    Gradient = polyfit(CpPitchValueMatrix(:,2),CpPitchValueMatrix(:,1),2);
    PitchAngleValues = [PitchAngleValues;
polyval(Gradient,FullMatrix(count,4))];
    hold on
end
```

```
PitchAnglesWithLocations = [FullMatrix(:,1), FullMatrix(:,2),
PitchAngleValues];
PitchAnglesExtrapolationMatrixNew =  [];
CorrespondingCpYawValues = [];
CpYawValueMatrix =[];
for count=1:1:length(PitchAnglesWithLocations)
    InputCpYawValue = FullMatrix(count,3);
    CpYawValueMatrix =[];
    ALineOfBestFitNew =
polyfit(ConstantPitchEquations(:,1),ConstantPitchEquations(:,2),2);
    BLineOfBestFitNew =
polyfit(ConstantPitchEquations(:,1),ConstantPitchEquations(:,3),2);
    CLineOfBestFitNew =
polyfit(ConstantPitchEquations(:,1),ConstantPitchEquations(:,4),2);
    PitchExtrapolationFitNew = -15:0.1:15;
    PitchAnglesExtractANew =
polyval(ALineOfBestFitNew,PitchAnglesWithLocations(count,3));
    PitchAnglesExtractBNew =
polyval(BLineOfBestFitNew,PitchAnglesWithLocations(count,3));
    PitchAnglesExtractCNew =
polyval(CLineOfBestFitNew,PitchAnglesWithLocations(count,3));
    PitchAnglesExtractCoeffNew = [PitchAnglesExtractANew,
PitchAnglesExtractBNew, PitchAnglesExtractCNew];
    CorrespondingCpPitchValue =
polyval(PitchAnglesExtractCoeffNew,InputCpYawValue);
    for secondcount = 1:1:length(ConstantYawEquations)
       CorrespondingCpYawValue =
polyval(ConstantYawEquations(secondcount,2:4),CorrespondingCpPitchValue);
       CpYawValueMatrix = [CpYawValueMatrix;
ConstantYawEquations(secondcount,1), CorrespondingCpYawValue];
    end
    hold on
    NewGradient = polyfit(CpYawValueMatrix(:,2),CpYawValueMatrix(:,1),2);
    YawAngleValues = [YawAngleValues;
polyval(NewGradient,FullMatrix(count,3))];
    hold on
end
YawAndPitchAnglesWithLocations = [PitchAnglesWithLocations(:,1),
PitchAnglesWithLocations(:,2), YawAngleValues,
PitchAnglesWithLocations(:,3)];
CpTotalValueMatrix= [];
CpStaticValueMatrix = [];
for count = 1:1:length(YawAndPitchAnglesWithLocations)
    YawAngleToPlot = YawAndPitchAnglesWithLocations(count,4);
    CpTotalYawExtractA = polyval(CpTotalBestFitLineA,YawAngleToPlot);
    CpTotalYawExtractB = polyval(CpTotalBestFitLineB,YawAngleToPlot);
    CpTotalYawExtractC = polyval(CpTotalBestFitLineC,YawAngleToPlot);
    ConstantYawAngleLineToPlotCpTotal = [CpTotalYawExtractA
,CpTotalYawExtractB,CpTotalYawExtractC];
    CpTotalValue =
polyval(ConstantYawAngleLineToPlotCpTotal,YawAndPitchAnglesWithLocations(coun
t,3));
    CpTotalValueMatrix = [CpTotalValueMatrix; CpTotalValue];
    CpStaticYawExtractA = polyval(CpStaticBestFitLineA,YawAngleToPlot);
    CpStaticYawExtractB = polyval(CpStaticBestFitLineB,YawAngleToPlot);
    CpStaticYawExtractC = polyval(CpStaticBestFitLineC,YawAngleToPlot);
```

```
    ConstantYawAngleLineToPlotCpStatic = [CpStaticYawExtractA
,CpStaticYawExtractB,CpStaticYawExtractC];
    CpStaticValue =
polyval(ConstantYawAngleLineToPlotCpStatic,YawAndPitchAnglesWithLocations(cou
nt,3));
    CpStaticValueMatrix = [CpStaticValueMatrix; CpStaticValue];
end
PTotalMatrix = [];
PStaticMatrix =[];
for count = 1:1:length(FullMatrix)
    PTotal = FullMatrix(count,5) -
(CpTotalValueMatrix(count,1)*(FullMatrix(count,5) - FullMatrix(count,7)));
    PStatic = FullMatrix(count,7) -
(CpStaticValueMatrix(count,1)*(FullMatrix(count,5) - FullMatrix(count,7)));
    PTotalMatrix = [PTotalMatrix; PTotal];
    PStaticMatrix = [PStaticMatrix; PStatic];
end
VelocityMatrix = [];
for count = 1:1:length(FullMatrix)
    Velocity = sqrt((PTotalMatrix(count,1)-
PStaticMatrix(count,1))*2/Density);
    VelocityMatrix = [VelocityMatrix; Velocity];
end
EverythingMatrix = [YawAndPitchAnglesWithLocations, VelocityMatrix];
ContourMatrix = [];
for count = 1:1:length(EverythingMatrix)
    YVelocity = EverythingMatrix(count,5)*sind(EverythingMatrix(count,3));
    XVelocity =
(EverythingMatrix(count,5)*sind(EverythingMatrix(count,4))*cosd(EverythingMat
rix(count,3)));
    ZVelocity =
(EverythingMatrix(count,5)*cosd(EverythingMatrix(count,3))*cosd(EverythingMat
rix(count,4)))/Speed;
    ContourMatrix = [ContourMatrix; YVelocity, ZVelocity, XVelocity];
end
EverythingMatrix = [EverythingMatrix, ContourMatrix];
for AddingOffsetCount = 1:1:length(EverythingMatrix)
    EverythingMatrix(AddingOffsetCount,2) =
EverythingMatrix(AddingOffsetCount,2) + 20;
    AddingOffsetCount = AddingOffsetCount + 1;
end
for NormalDistanceCount = 1:1:length(EverythingMatrix)
    EverythingMatrix(NormalDistanceCount,1) =
EverythingMatrix(NormalDistanceCount,1)/((994*2)/6);
    EverythingMatrix(NormalDistanceCount,2) =
EverythingMatrix(NormalDistanceCount,2)/(1133/6);
end
ExportMatrix = [EverythingMatrix(:,3), EverythingMatrix(:,4),
EverythingMatrix(:,5), EverythingMatrix(:,6), EverythingMatrix(:,7),
EverythingMatrix(:,8), PTotalMatrix, PStaticMatrix, CpTotalValueMatrix,
CpStaticValueMatrix];
ExportExcelFileName = strcat('UncertaintyValuesToCopy-',ExcelFile);
writematrix(ExportMatrix,ExportExcelFileName);
a = EverythingMatrix(:,1);
b = EverythingMatrix(:,2);
c = EverythingMatrix(:,7);
d = EverythingMatrix(:,6);
```

```
e = EverythingMatrix(:,8);
CustomColourMapRange = 0.25:0.05:1;
figure(4)
F = scatteredInterpolant(a,b,c);
[aq,bq] = meshgrid(a,b);
cq = F(aq,bq);
h = pcolor(aq,bq,cq);
shading interp
colormap(turbo(33));
view(2)
set(gca,'TickDir','out')
xticks([0 0.3 0.6 0.9]);
xticklabels([0 0.3 0.6 0.9]);
xlabel('x / w_c','fontweight','bold','fontsize',20,'fontname', 'times');
ylabel('y / h_c','fontweight','bold','fontsize',20,'fontname', 'times');
yticks([0 0.25 0.5 0.75 1.0 1.25 1.5]);
yticklabels([0 0.25 0.5 0.75 1.0 1.25 1.5]);
ax = gca;
ax.FontSize = 12;
set(gca,'box','off')
set(gca,'TickLength',[0.03, 0.005])
set(gca, 'FontName', 'times')
set(gca,'XMinorTick','on','YMinorTick','on')
ay = gca;
ay.FontSize = 14;
p = colorbar;
caxis([0.25,1.025]);
cmap(33) = 1;
colorbar('Ticks', [0.25 0.4 0.54 0.69 0.83 0.98], 'TickLabels',[0.25 0.4 0.54
0.69 0.83 0.98])
hold on
quiver(a,b,d,e,1,'black','filled');
end
```